



U.S. Department
of Transportation

Federal Railroad
Administration

Investigation of Local Commutation as Applied to Linear Synchronous Motors for Use as a Maglev Propulsion System

Office of Research
and Development
Washington, DC 20590

R. Wiesman
R. Fontana
B. Gamble
D. Cope
T. Mason
G. Bastarche

Foster-Miller, Inc.
350 Second Avenue
Waltham, MA 02154-1196

M. Coltman

U.S. Department of Transportation
Volpe National Transportation Systems Center
55 Broadway, Kendall Square
Cambridge, MA 02142-1093

DOT/FRA/ORD-95/01

May 1995
Final Report

Limited Rights Notice (Jun 1987)

NOTICE

This document is disseminated under the sponsorship of the Department of Transportation in the interest of information exchange. The United States Government assumes no liability for its contents or use thereof.

NOTICE

The United States Government does not endorse products of manufacturers. Trade or manufacturers' names appear herein solely because they are considered essential to the object of this report.

Limited Rights Notice (JUN 1987)

(a) These data are submitted with limited rights under Government contract No. [TBD] (and subcontract [TBD], if appropriate). These data may be reproduced and used by the Government with the express limitation that they will not, without written permission of the Contractor, be used for purposes of manufacture nor disclosed outside the Government; except that the Government may disclose these data outside the Government for the following purposes, if any, provided that the Government makes such disclosure subject to prohibition against further use and disclosure: [Agencies may list additional purposes as set forth in 27.404(d)(1) or if none, so state]

(i) This data shall be available, in whole or in part, for use within the Government for the purpose of analysis, and future system acquisition planning. This data may then be transformed with other data to produce form, fit and function data to form a unified system performance definition or acquisition plan, which may then be made available to other members of the Government or potential non-Government sources which possess a bona fide interest in the Maglev program. This includes the incorporation of said form, fit and function data into future acquisitions for Maglev system development or any other procurement. The data may also be made available for review and comment by private sources commissioned by the Government.

(ii) Review and comment by private sources commissioned by the Government.

(b) This Notice shall be marked on any reproduction of these data, in whole or in part.

(End of notice)

DOT/FRA/ORD-95/01

**Investigation of Local Communtation as
Applied to Linear Synchronous Motors
for Use as a Maglev Propulsion System**

R. Wiesman
R. Fontana
B. Gamble
D. Cope
T. Mason
G. Bastarche

Foster-Miller, Inc.
350 Second Avenue
Waltham, MA 02154-1196

Final Report

M. Coltman

U.S. Department of Transportation
Volpe National Transportation Systems Center
55 Broadway, Kendall Square
Cambridge, MA 02142-1093

May 1995

Technical Report Documentation Page

1. Report No. DOT/FRA/ORD - 95/01		2. Government Accession No.		3. Recipient's Catalog No.	
4. Title and Subtitle Investigation of Local Commutation as Applied to Linear Synchronous Motors for Use as a Maglev Propulsion System				5. Report Date May 1995	
				6. Performing Organization Code 30233	
7. Author(s) R. Wiesman, R. Fontana, B. Gamble, D. Cope, T. Mason, G. Bastarache				8. Performing Organization Report No. DOT-0002-FM-94062-912	
9. Performing Organization Name and Address Foster-Miller, Inc. 350 Second Avenue Waltham, MA 02154-1196				10. Work Unit No. (TRAIS)	
				11. Contract or Grant No. DTFR53-94-C-0002	
12. Sponsoring Agency Name and Address DOT/RSPA Volpe National Transportation Systems Center 55 Broadway, Kendall Square Cambridge, MA 02143-1093				13. Type of Report and Period Covered Final Report	
				14. Sponsoring Agency Code	
15. Supplementary Notes U.S. Department of Transportation Volpe National Transportation Systems Center Kendall Square, Cambridge, MA 02142-1093					
16. Abstract The Locally Commutated Linear Synchronous Motor (LCLSM) concept was analyzed and demonstrated. Design and analysis of an 8.1 Megawatt propulsion motor for a 100 Mg Maglev vehicle resulted in a LCLSM system capable of generating smooth thrust with non-overlapping individual propulsion coils. Each coil is powered by a dedicated H-bridge inverter operating from a DC bus and controlled by a dedicated microcontroller which communicates to a base station via fiber optic bus. Control systems were designed and analyzed and characteristics including bus harmonics, eddy current generation, control stability, and thrust were determined by analysis and simulation. A 1/10th scale experiment utilizing 64 coils and controllers was built which demonstrated the viability of the LCLSM concept. Results of this program indicate that the LCLSM motor design is well suited to Maglev and other transportation applications. Very high efficiency, power factor, reliability, system flexibility, ride quality, and safety can be achieved with the LCLSM. The LCLSM concept has been developed and demonstrated and it is recommended that it be evaluated for economic viability as a propulsion technology for Maglev and related applications.					
17. Key Words motor, linear motor, distributed control, power transfer, synchronous motor				18. Distribution Statement LIMITED RIGHTS NOTICE (JUN 1987)	
19. Security Classif. (of this report) UNCLASSIFIED		20. Security Classif. (of this page) UNCLASSIFIED		21. No. of Pages 91	22. Price

Form DOT F 1700.7 (8-72)

Reproduction of completed page authorized

CONTENTS

Section	Page
INTRODUCTION	INTRO-1
1. SYSTEM DESIGN AND ANALYSIS	1-1
1.1 Analytical and Simulation Model	1-1
1.1.1 LCLSM Propulsion Model (Coil Design)	1-1
1.1.2 Control Block Diagrams	1-3
1.1.3 Inverter Models	1-8
1.1.4 Ride Quality Requirements Review	1-10
1.2 Tradeoff Analysis on Inverter Topology, Configuration, Switching Device Selection, and DC Bus Voltage Level	1-10
1.2.1 Single and Multilevel Bus Configuration Analysis	1-10
1.2.2 Device Selection Trade Study	1-14
1.2.3 Trade Study Summary	1-14
1.3 Propulsion Analysis (Thrust Acceleration and Speed for 150 Passenger, 100 Mg, 40m long, 100 to 150 kN Thrust, 0.15 to 0.25g, Grades to 10 percent) ...	1-17
1.3.1 Utilize Task 1.1 Analysis to Characterize Conditions	1-17
1.3.2 Determine Features and Parameters to be Verified in Testing	1-20
1.4 Power Transfer	1-21
1.4.1 Expand Power Transfer Model	1-21
1.4.2 Parametric Studies	1-21
1.4.3 Summarize	1-22
1.5 Scaling Laws (1/10 to 1/25th Scale)	1-22
1.5.1 Document Scaling Laws	1-22
1.5.2 Model 1/10 Scale Permanent Magnet Representation of the Field Winding	1-26
1.5.3 Summarize Scaling Laws (Combine 1.5.1 and 1.5.2)	1-27
2. COMPONENT DESIGN AND ANALYSIS	2-1
2.1 Preliminary Full-scale Circuit Analysis and Preliminary Design	2-1
2.2 Detailed Scale Circuit Analysis and Preliminary Design	2-4
2.2.1 Description of Scale System Configuration Used for Controller Design	2-5
2.2.2 Results of Controller Investigation	2-6
2.3 Design 1/10 Scale Experiment	2-8
3. FABRICATE SCALE EXPERIMENT	3-1
3.1 Component Fabrication	3-1
3.1.1 Scale Model System Mechanical Fabrication	3-1
3.1.2 Inverter/Control Component Fabrication	3-3
3.1.3 Component Tests	3-5
3.2 Assembly	3-5
3.2.1 Mechanical Assembly	3-5

Section	Page
3.2.2	Balancing 3-6
3.3	Debugging 3-6
4.	TEST AND EVALUATION 4-1
4.1	Basic Electrical Tests 4-1
4.1.1	Static Tests Measuring Variation in Electrical Parameters 4-1
4.2	Dynamic Tests 4-3
4.2.1	No Load Cases 4-7
4.2.2	Partial Load Cases 4-12
4.2.3	Full Load Cases 4-18
4.3	Experimental Conclusions/Recommendations 4-20
5.	CONCLUSIONS AND RECOMMENDATIONS BASED ON THE LCLSM PROGRAM RESULTS 5-1
6.	REFERENCES 6-1
APPENDIX A - HARMONIC CURRENT EQUATIONS A-1	
APPENDIX B - IGBT DATA SHEET B-1	

ILLUSTRATIONS

Figure	Page
1-1.	Statement of work operating conditions 1-1
1-2.	Coil configuration 1-3
1-3.	Bus filtering 1-4
1-4.	AC voltage and current from one inverter 1-5
1-5.	Bus and filter losses (based on full current at full speed) 1-6
1-6.	Local control 1-6
1-7.	Local reference current waveform 1-6
1-8.	Block representation of local control 1-7
1-9.	Simulink model of PI control system 1-9
1-10.	PI control system simulation 1-10
1-11.	Harmonic content (40 kHz example at full speed) 1-11
1-12.	Switch states of full H-bridge configuration 1-11
1-13.	Permissible RMS acceleration levels (2) 1-12
1-14.	Single level H-bridge inverter topology 1-12
1-15.	Multilevel inverter topology 1-13
1-16.	Switching harmonic versus switching speed 1-16
1-17.	Track coil current and EMF versus position (four SC coils) 1-17
1-18.	Track coil current and EMF versus position (one SC coil) 1-18
1-19.	Variation in propulsion thrust versus gap 1-18
1-20.	Shield eddy currents due to bar passing 1-19
1-21.	Harmonic losses in the shield 1-20
1-22.	Power transfer configuration 1-21
1-23.	Power transfer circuit 1-22
1-24.	Power transfer mutual inductance variation with position 1-23
1-25.	Power transfer mutual inductance as a function of gap size 1-23
1-26.	Power transfer parameter variation with mutual inductance 1-23
1-27.	Scale system flux linkage 1-26
1-28.	Scale system power 1-26
2-1.	System summary block diagram 2-1
2-2.	Base station control blocks 2-1
2-3.	Position detection 2-2
2-4.	Relative impedance as a function of coil position 2-2
2-5.	Local controller software blocks 2-3
2-6.	Base station Simulink model 2-4
2-7.	Full and scale system comparison 2-5
2-8.	Summary scaled system block diagram 2-5
2-9.	Base station blocks - 1/10 scale system 2-6
2-10.	Local controller blocks - 1/10 scale system 2-7
2-11.	Current controller design 2-7
2-12.	Current controller pole zero maps 2-8
2-13.	Current control bode plots 2-9
2-14.	Thrust as a function of current control 2-10
2-15.	Scale system design 2-11

Figure	Page
2-16. Rotor detailed design	2-12
2-17. Back EMF testing	2-12
2-18. EMF test results	2-13
2-19. Calculated EMF for four permanent magnets	2-13
2-20. Controller hardware block diagram	2-14
2-21. Controller board design	2-15
3-1. LCLSM table	3-1
3-2. LCLSM "vehicle"	3-2
3-3. Counterweight and position detection coils	3-3
3-4. Load motor	3-4
3-5. Coil control board	3-4
3-6. Base station control box	3-5
3-7. Calculated impact of assembly tolerances	3-6
4-1. Variation in coil resistance	4-1
4-2. Bridge measurements	4-2
4-3. Field characteristics/back EMF	4-3
4-4. Typical test run	4-5
4-5. Coil voltage on one side only	4-6
4-6. PWM harmonics	4-6
4-7. No-load, no-acceleration, case 16 (1.28 Hz, 5.87 m/sec)	4-7
4-8. No-load, no-acceleration, case 17 (2.78 Hz, 12.72 m/sec)	4-8
4-9. No-load, no-acceleration, case 19 (1.25 Hz, 5.72 m/sec)	4-8
4-10. No-load, no-acceleration, case 20 (2.56 Hz, 11.73 m/sec)	4-9
4-11. No-load, acceleration, case 27 (0.47 Hz, 2.15 m/sec, 0.3 Hz/sec, 1.39 m/sec ²)	4-9
4-12. No-Load, acceleration, case 29 (0.82 Hz, 3.75 m/sec, 0.39 Hz/sec, 1.79 m/sec ²)	4-10
4-13. No-load, deceleration, case 32 (0.12 Hz, 0.536 m/sec, 0.39 Hz/sec, 1.79 m/sec ²)	4-11
4-14. No-load, deceleration, case 34 (0.23 Hz, 1.07 m/sec, 0.52 Hz/sec, 2.38 m/sec ²)	4-11
4-15. No-load, deceleration, case 37 (0.22 Hz, 0.98 m/sec, 0.48 Hz/sec, 2.2 m/sec ²)	4-12
4-16. Partial-load, no acceleration, case 21 (0.21 Hz, 0.95 m/sec)	4-13
4-17. Partial-load, no-acceleration, case 22 (1.22 Hz, 5.58 m/sec)	4-14
4-18. Partial-load, no acceleration, case 23 (1.59 Hz, 7.3 m/sec)	4-14
4-19. Partial-load, acceleration, case 26 (0.39 Hz, 1.78 m/sec, 0.35 Hz/sec, 1.56 m/sec ²)	4-15
4-20. Partial-load, acceleration, case 27 (0.5 Hz, 2.3 m/sec, 0.35 Hz/sec, 1.56 m/sec ²)	4-15
4-21. Partial-load, acceleration, case 29 (0.94 Hz, 4.3 m/sec, 0.26 Hz/sec, 1.2 m/sec ²)	4-16
4-22. Partial-load, deceleration, case 38 (0.94 Hz, 4.3 m/sec, 0.78 Hz/sec, 3.6 m/sec ²)	4-16
4-23. Partial-load, deceleration, case 39 (0.625 Hz, 2.86 m/sec, 0.52 Hz/sec, 2.38 m/sec ²)	4-17
4-24. Partial-load, deceleration, case 39 - single side coil voltage and bridge current (0.625 Hz, 2.86 m/sec, 0.52 Hz/sec, 2.38 m/sec ²)	4-17
4-25. Partial-load, deceleration, case 41 (0.12 Hz, 5.4 m/sec, 0.26 Hz/sec, 1.2 m/sec ²)	4-18
4-26. Full-load, no acceleration, case 24 (0.35 Hz, 1.6 m/sec)	4-19
4-27. Full-load, no acceleration, case 25 (0.25 Hz, 1.16 m/sec)	4-19

Figure	Page
4-28. Full-load acceleration, case 31 (0.16 Hz, 0.72 m/sec, 0.13 Hz/sec, 0.60 m/sec ²)	4-20
4-29. Full-load, acceleration, case 30 (0.27 Hz, 1.25 m/sec, 0.11 Hz/sec, 0.52 m/sec ²)	4-21
4-30. Impact of 20 percent coil misplacement	4-21

TABLES

Table		Page
1-1.	Baseline full-scale motor summary	1-2
1-2.	Baseline full-scale bus characteristics	1-4
1-3.	Summary of inverter topology study	1-13
1-4.	Comparison of switching devices (3-5)	1-15
1-5.	Track coil resistive losses	1-19
1-6.	Power transfer for baseline system parameters	1-22
1-7.	Scaling summary	1-24
2-1.	Scale model features	2-11
4-1.	Encoder calibration	4-2
4-2.	Load motor characteristics	4-2
4-3.	Permanent magnet model	4-3

INTRODUCTION

The Locally Commutated Linear Synchronous Motor (LCLSM) program has demonstrated the technical feasibility and practicality of the LCLSM concept for Maglev applications. The work included analysis and simulation of critical components for a full-scale system and a demonstration motor based on a 1/10th scale system. The LCLSM concept utilizes modular distributed power processing for the motor. In this case, individual nonoverlapped coils are each driven by a dedicated local inverter controlled by a dedicated local processor. For Maglev applications this has the advantage of increased reliability, performance, efficiency, and flexibility with a potential reduction in system cost compared with block switched systems.

It is useful to describe the block switched linear synchronous motor typically considered for Maglev propulsion to see the basis and motivation for the LCLSM system. Block switched systems for Maglev propulsion power a large section of guideway, typically 500m or more, over which the vehicle is traveling. The entire section (block) of propulsion coils in which the vehicle travels is energized. The inverter supplying power to each block must be sized to apply the drive power needed by the vehicle. The inverter for the block must drive the propulsion current through the voltage produced by the inductance and resistance of the entire block in addition to the net back EMF (Electro Motive Force) produced by all of the vehicle field coils. Thus the inverter must supply all of the propulsion power as well as drive large sections of coils that are not utilized and represent losses. To reduce the losses and account for the relatively long duration of the current in the block, the coils must have a sufficiently large conductor cross section to reduce heating. Vehicle configurations are also somewhat limited since the back EMF must be in a range matched to the power supply. The LCLSM concept was developed to overcome these difficulties by applying semiconductor power handling technologies which have become viable within the past few years.

The LCLSM powers the minimum number of coils required. For propulsion, only the coils near the vehicle fields are powered. Each coil is individually controlled. The back EMF experienced is only that produced locally by the vehicle fields. Thus, any length vehicle configuration can be accommodated. The back EMF does not add, and the power per local inverter does not increase as the size and weight of the vehicle changes. The LCLSM system therefore can offer greater flexibility. The track coil cross section can be reduced since the net on time is less, thus reducing conductor costs. A critical factor when considering the LCLSM is that the net power delivered to the vehicle is shared among the local individual cell inverters so the power handling requirements of the local inverters is considerably less than that required for the block switched system. This allows lower power, higher performance electronics to be utilized. Based on preliminary cost estimates, combining the reduced conductor cost with the lower power, high volume semiconductor cost may make LCLSM cost effective for Maglev applications.

Other inherent features of LCLSM can provide further improvements in performance and reduction in system cost. Smooth thrust can be provided, even on a per magnet basis, with a nonoverlapping track coil configuration. This can provide simpler installation and reduced component cost relative to overlapping coil configurations. The local controllers can also accommodate errors in gap and positioning of the coils or failure of nearby coils by modifying the drive current to accommodate these errors and maintain smooth thrust. The net system

reliability is high because many distributed inverter modules can fail without halting operation of the system. Repair is potentially simplified by the nonoverlapped track coil configuration with dedicated electronics. Cost and reliability advantages due to the ability of the LCLSM system to accommodate manufacturing variations may provide substantial savings in net system cost in a real world environment and long term usage.

The application of LCLSM for Maglev systems spans a wide range of system design and utilization issues. The LCLSM concept is a new approach to motor design and control made practical by developments in power electronics and microcontrollers. The regimes of operation are substantially different from the block switched system in actual implementation. In particular, the distributed control and communications requirements are critical to the system design. The objective of this program was investigation and demonstration of the basic LCLSM concept.

Intro.1 Final Report Format

This report utilizes a format in which there is a brief synopsis in *italics* at the beginning of each subsection. More detailed description of the work performed in response to the statement of work follows in that subsection. Because a wide range of issues relating to LCLSM could have been studied, this format is used to make the motivation and extent of the work performed clear.

Intro.2 Summary of the LCLSM Program

System design and analysis were performed for a LCLSM for Maglev application. A one-tenth scale model was analyzed, designed, and constructed to validate the LCLSM concept. The analysis and model tests demonstrated the technical viability of the LCLSM concept.

The overall design philosophy which guided the development of the LCLSM system was high efficiency, high reliability, graceful degradation, and low electromagnetic interference. LCLSM is a single-layer propulsion and power transfer system in which independent controllers control dedicated coils to supply a desired waveform with the proper frequency, phase and amplitude. In one embodiment, the coils are commutated locally by pulse-width-modulation (PWM) of semiconductor switches in an H-bridge configuration controlled by signals transmitted over fiber optic communications lines from a central control. Local communication allows energized coils to be limited to those required to achieve a specific purpose (propulsion or power transfer). For example, only those coils in the immediate vicinity of the superconducting magnets need to be energized for propulsion.

The LCLSM design utilizes the same guideway coils for the propulsion and power transfer functions. The PWM scheme is modified from that appropriate for propulsion to a higher frequency, lower current waveform appropriate for power transfer. Power is inductively coupled to onboard coils for power factor correction. In addition, for true Maglev systems, the LCLSM coils can also be used to supply a magnetic guidance function (port-to-starboard forces).

A complete LCLSM system will have a great many identical single units, especially semiconductor devices. Repeated experience with semiconductor devices has shown that the cost of a system must account for the dramatic unit price drop as a result of the increase in volume of units. It is recommended that LCLSM be evaluated for economic viability as a propulsion technology for Maglev and related applications.

1. SYSTEM DESIGN AND ANALYSIS

1.1 Analytical and Simulation Model

1.1.1 LCLSM Propulsion Model (Coil Design)

The LCLSM propulsion models consist of mutual inductance models between the track propulsion coils, the field winding, and equivalent windings representing eddy current paths in the magnet shields. These models have been constructed in Mathcad. The models are used to optimize coil geometries producing smooth thrust and to estimate the losses in the shields due to switching harmonics and the passing of the vertical portions of the track coils. This latter loss appears to dominate for the cases studied to date. These tools are used to characterize both the constant thrust and transient acceleration cases following a change in commanded thrust or bus voltage.

The technical requirements from the statement of work can be summarized as follows:

- 150 passengers.
- 100 Mg.
- 40m long vehicle.
- 100 to 150 kN thrust.
- 135 m/sec cruise.
- 30 to 60 kN thrust at cruise.
- Acceleration 0.15 to 0.25g.
- Full performance for 3.5 percent gradients.
- Reduced performance for 10 percent gradients.

For propulsion motor design, these requirements can be summarized as power and current limits as shown in Figure 1-1. There are two types of limits presented in this figure. The

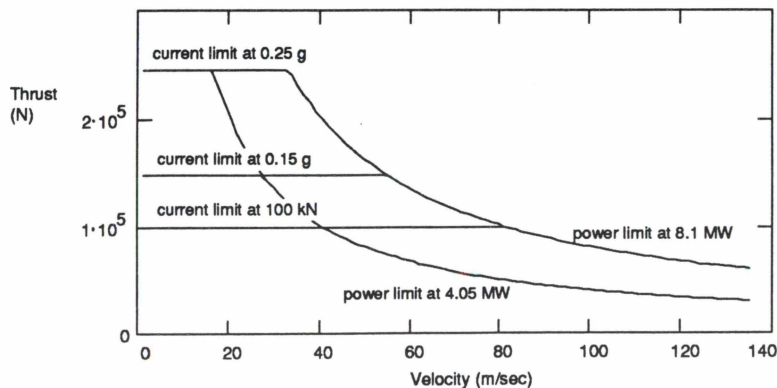


Figure 1-1. Statement of work operating conditions

thrust (or acceleration) requirement translates into a current requirement for the track coils. The power limit corresponds to a peak bus current (for a given bus voltage).

The baseline design selected to address these requirements is summarized in Table 1-1 and is discussed in detail in the following sections. The design consists of racetrack shaped field windings (Figure 1-2) on the vehicle and rectangular shaped track coils (nonoverlapped). The baseline consist includes two vehicles and three "bogies" containing eight magnets each (four per side) for a total of 24 superconducting magnets.

Figure 1-2 schematically depicts a set of four SCM (Super Conducting Magnet) field magnets passing a series of track propulsion coils (track coils are labeled A-M). The moving field magnets produce an EMF wave in the track coils. This induced voltage is termed the back EMF since the applied voltage must be higher than the back EMF to provide a forward propulsive force. Shorting the coils would produce a braking force due to the induced back EMF voltage. The back EMF wave moves down the track at the velocity of the vehicle. The coils are powered to produce a current wave (track current) which is controlled to move in synchronism with the EMF.

In the full-scale baseline design each coil is powered from a DC bus through a dedicated inverter. The dedicated or "local" inverter produces a sinusoidal current in the track coil which is in synchronism with the field coils as they pass. The principal difference between the LCLSM and the block switched linear synchronous motor is the ability of the local inverter to tailor the current profile. The resulting benefit is a reduction in track coil loss (operating cost savings) or a reduction in copper content for constant losses (capital cost savings). If the pitch of the track coils is selected to be two-thirds of the pitch of the superconducting coils, the current distribution in the track is indistinguishable from a very short three-phase block switched system for the sinusoidal excitation utilized. The local commutation permits track pitches which are not simple fractions of the superconducting coil pitch. This provides an

Table 1-1. Baseline full-scale motor summary

Field winding	
Pitch (spacing of coil centers)	1.3 m
Racetrack:	
Diameter of the mid wire in the end turns	0.5 m
Straight length of mid wire	0.5 m
Coil section:	
Radial thickness	8 cm
Width	16 cm
Ampere-turns	1.8×10^6
Track coil	
Pitch (center to center)	0.668m
Coil height (center to center)	0.7m
Coil length	0.6m
Resistance	0.015Ω
Inductance	0.275 mHenry
Gap (track coil mid-plane to SCM mid-plane)	0.3 m
Mutual inductance	2.2×10^{-7} Henry/(turn) ²
Full speed	135 m/sec
Full speed fundamental frequency	51.9 Hz
Thrust (2 SCM pole pair)	3.75 Newton/A-turn (track coil-peak)

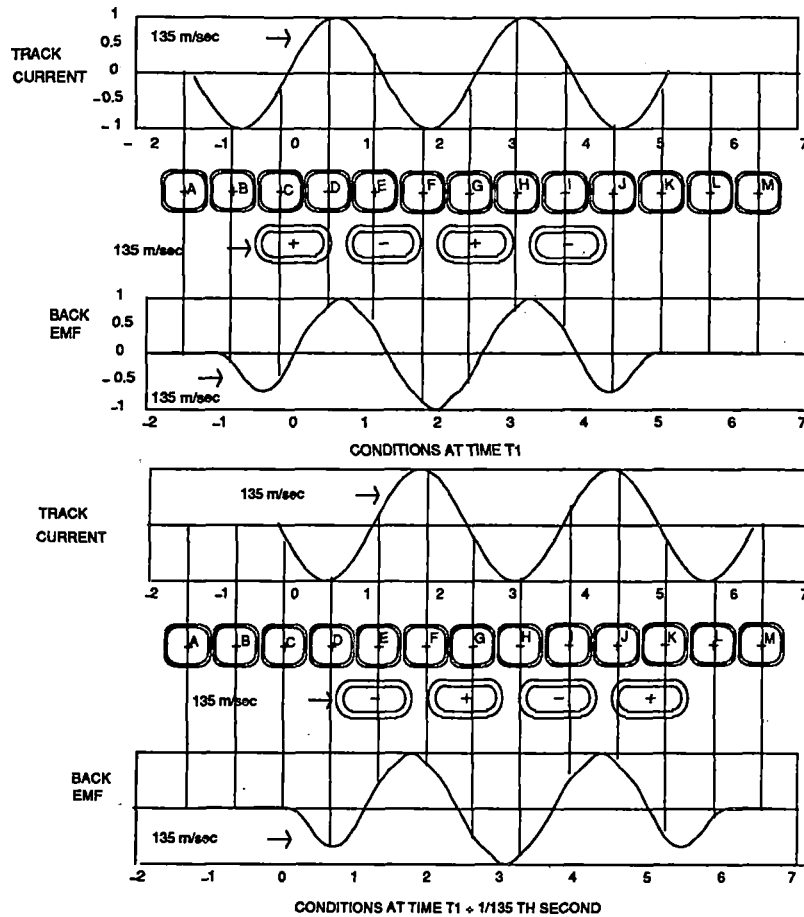


Figure 1-2. Coil configuration

additional degree of freedom for the machine designer which can be used to minimize thrust variations on individual coils. This strategy led to the selection of the above design.

Figure 1-3 presents the baseline inverter and bus configuration.

The baseline bus and filter design (Table 1-2) was modeled for a range of PWM frequencies to determine the magnitude of the AC current and frequency at the PWM frequency as a function of the distance along the bus from the active area (vehicle location). The results are summarized in Figure 1-4 for pulse width modulation frequencies from 10 to 40 kHz. Note that the bus filtering improves as PWM frequency increases.

The resulting losses in the bus and filters are summarized in Figure 1-5. The bus losses at full power represent approximately 3 percent of the full power rating of the system. If a 40 kHz system is selected, Figure 1-4 indicates that reduced resistance in series with the local capacitance in the local filter could be considered to further reduce this loss.

* **1.1.2 Control Block Diagrams**

- * • *Microprocessor PWM voltage control.*
- * • *Adaptive (hysteretic) PWM.*
- * • *Vector control of synchronous motors.*

"Information on this page identified by asterisk (*) in the margin is proprietary to Foster-Miller, Inc.

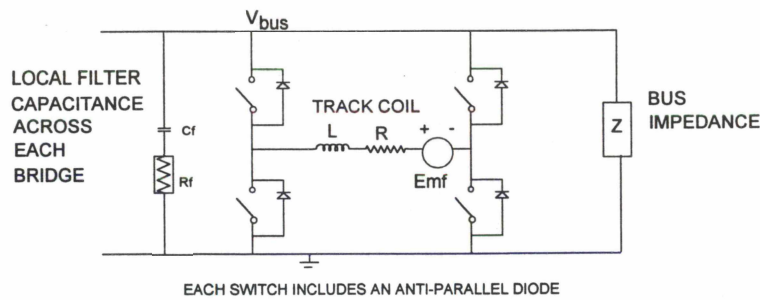


Figure 1-3. Bus filtering

Table 1-2. Baseline full-scale bus characteristics

Copper area	25.8 cm ²
Spacing	0.152m (6 in.)
Bus inductance	6.5E-4 Henry/km
Bus capacitance	1.7E-8 Farad/km
Local capacitance across each bridge	40 μFarad
Resistance in series with the local capacitance	0.1 ohm
Typical bus supply voltage	2 kV

* The control block diagrams are developed to present the variables to be controlled and the control strategy to produce the desired response in all operating modes. The diagrams include the quantities to be measured and sources of noise in these measurements. The control methods have been selected as appropriate for synchronous machines with high power factor and high efficiency. Control issues include transient response given the conductive magnet shields which act as damper windings (time constant on the order of 1/6 sec). In addition, it is anticipated that filtering will cause the bus voltage to sag following a request for an increase in thrust. If necessary vector control can be used to improve the transient response. Additional control issues include noise on the control signals including air gap flux, back EMF, and propulsion coil current.

* Early in the program the control of the current in each local bridge was reviewed. The work reviewed in this section addresses PID control of these currents. In subsequent sections alternate control strategies are considered. Figure 1-6 shows the local control of the track coil current based on the commanded current amplitude and the measured train velocity and position. The local controller and bridge provide the appropriate voltage waveform which results in a suitable current waveform. In this system the back EMF due to the SCM is represented as a disturbance which is not directly measured. Modeling of the back EMF is described in more detail in the simulation description.

* The local processor generates a reference current waveform based on the received information from the bus (Figure 1-7). This reference waveform will be used as the input command to a control loop with current feedback shown in Figure 1-8.

* The control loop shown in Figure 1-8 is used to investigate appropriate control functions (G) which will provide good tracking of the reference current waveform for the expected EMF.

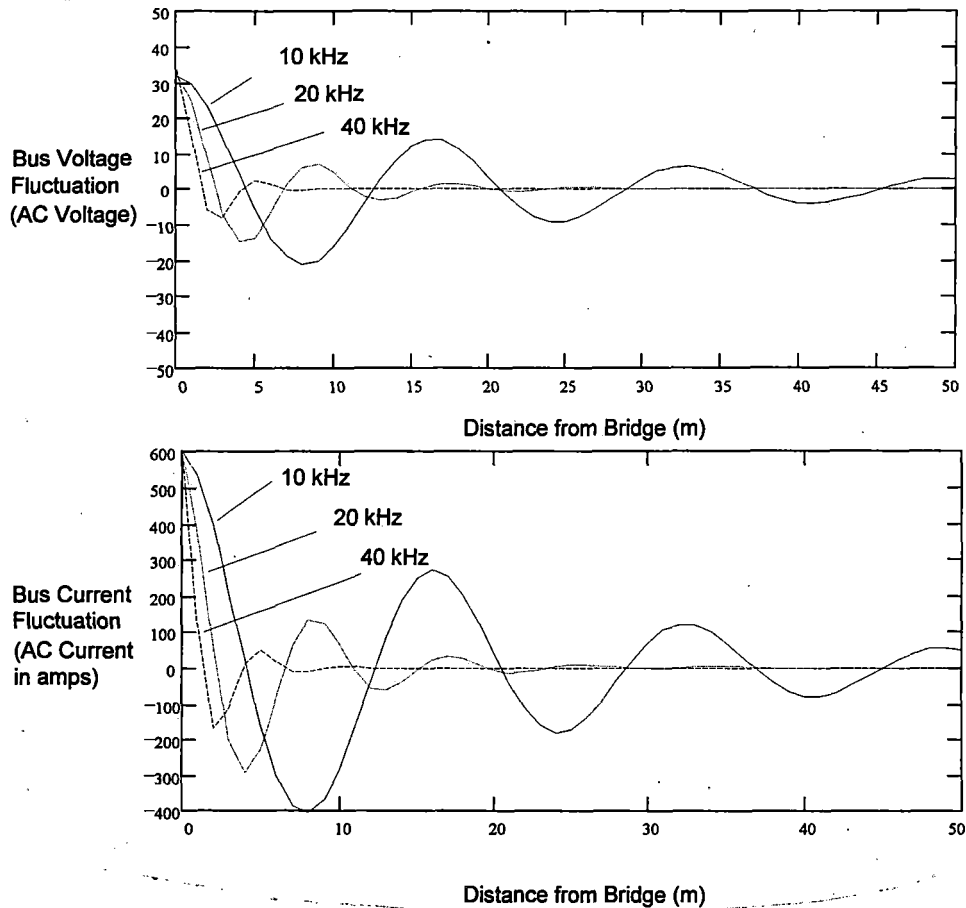


Figure 1-4. AC voltage and current from one inverter

* This system was investigated assuming PI control with the objective of using only current
 * as feedback (no EMF feedback) as follows.

* The system transfer function is:

$$\frac{i_{\text{coll}}}{i_{\text{ref}}} = \frac{G \cdot K_A}{L \cdot s + R + G \cdot K_A}$$

* For PI control gain is given by:

$$G = K \cdot \left[\frac{s + a}{s} \right]$$

* By inspection this is a second order system where the damping ratio, ξ , and undamped
 * natural frequency, ω_n , are given by:

$$\frac{i_{\text{coll}}}{i_{\text{ref}}} = \frac{\frac{K \cdot K_A}{L} \cdot (s + a)}{s^2 + \left[\frac{R}{L} + \frac{K \cdot K_A}{L} \right] \cdot s + a \cdot \frac{K \cdot K_A}{L}}$$

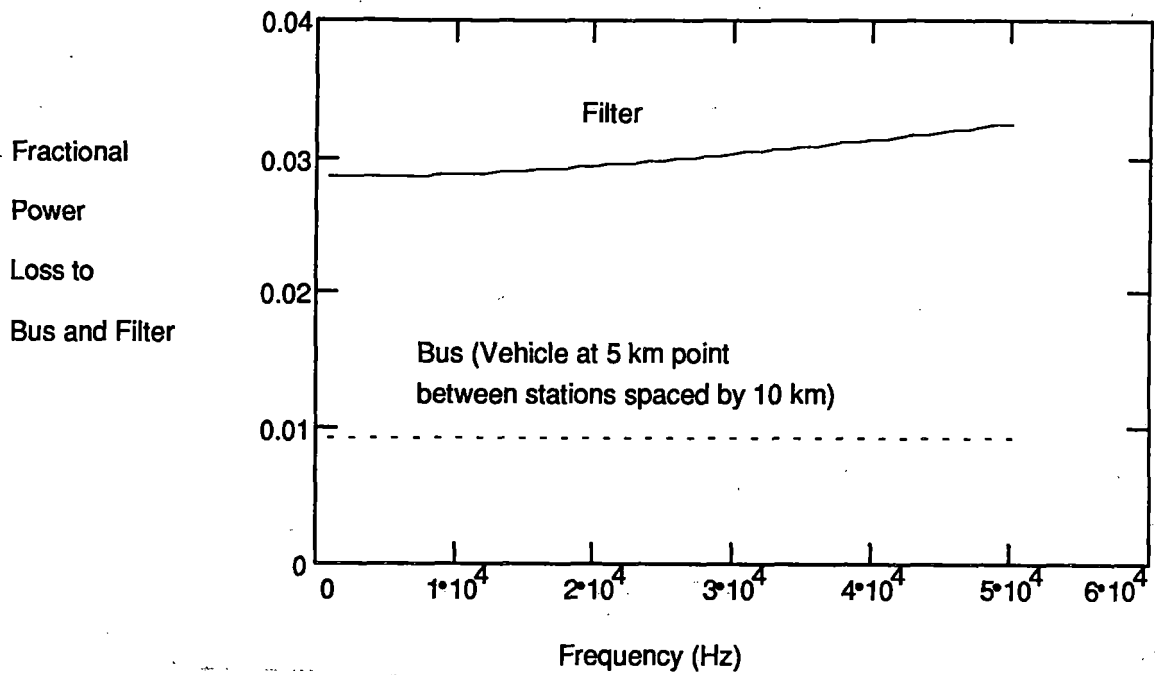


Figure 1-5. Bus and filter losses (based on full current at full speed)

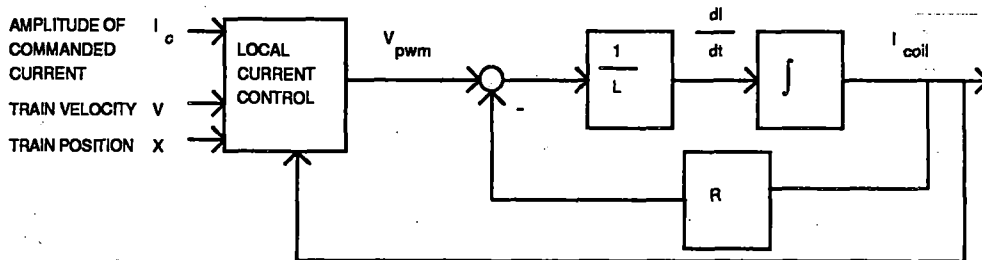


Figure 1-6. Local control

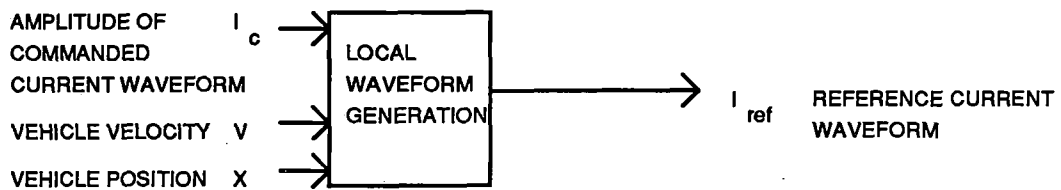


Figure 1-7. Local reference current waveform

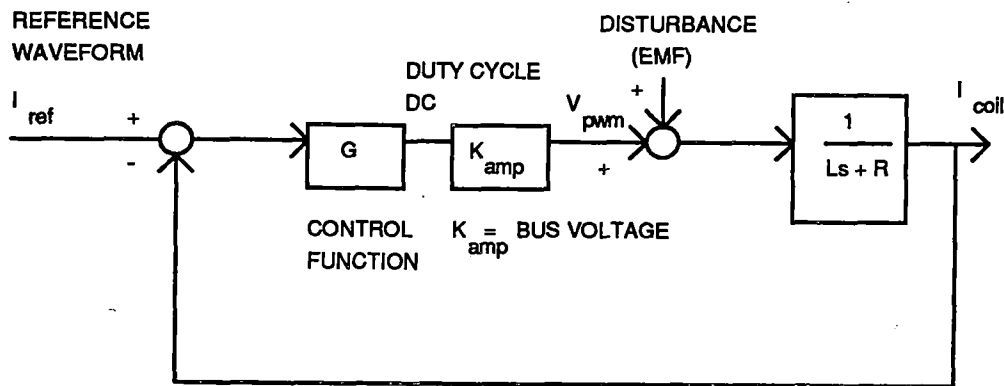


Figure 1-8. Block representation of local control

$$2 \cdot \xi \omega_n = \frac{R}{L} + \frac{K \cdot K_A}{L}$$

$$\omega_n^2 = a \cdot \frac{K \cdot K_A}{L}$$

By appropriate selection of these parameters the control can be made fast and stable (1). ξ is generally selected at a value of 0.707 (critically damped) and ω_n is selected well away from the frequency of disturbances (i.e., well away from the fundamental of 50 Hz, the PWM frequency of 40 kHz, and well below the corner frequency of the selected low pass filter ~6,000 Hz). A frequency of 1,900 Hz was found to yield good response.

Stable and fast response is achieved with critical damping if:

$$\xi = 0.707 \text{ (2)}$$

ω_n selected away from disturbances

$$\text{IE } \omega_n = 1,900 \cdot 2 \cdot \pi \cdot \frac{\text{rad}}{\text{sec}}$$

Then

$$K = \frac{2 \cdot \xi \cdot \omega_n \cdot L - R}{K_A}$$

$$a = (\omega_n)^2 \cdot \frac{L}{K \cdot K_A}$$

For the full-scale coil

$$R = 0.01792 \cdot \text{ohm}$$

$$L = 0.000264 \cdot \text{Henry}$$

$$K_A = 2,000 \cdot V$$

$$G = 0.00222 \cdot \frac{1}{A} \cdot \left[\frac{s + 8.47684 \cdot 10^3 \cdot \frac{1}{\text{sec}}}{s} \right]$$

Since control was implemented using a digital microcontroller, a discrete transformation was applied to the above continuum analysis. This was accomplished as follows:

$$s = \frac{2}{T} \cdot \left(\frac{z-1}{z+1} \right) \text{ bilinear transformation (3)}$$

$$G = \frac{(z - 0.71008)}{(z - 1)} \cdot \left(0.00324 \cdot \frac{1}{A} \right)$$

This control function was simulated using Simulink to verify stability and response (Figure 1-9). Simulink is software for numerical analysis of control system response. Simulink is manufactured by Mathworks, Inc., Natick, MA. This model was used to investigate the response for a broad range of EMF disturbances. The results are presented in Figure 1-10 based on a 40 μ sec computer cycle time ($T = 40 \mu\text{sec}$).

The output was investigated for harmonic content of the ripple current produced by the system. The results are presented in Figure 1-11. As can be seen, there are harmonics at 40 kHz and multiples of 40 kHz. The amplitude of the switching harmonic at 40 kHz is approximately 14A. Appendix A presents a method for estimating the magnitude of the switching harmonic (ripple current).

It has been recommended that alternate control strategies be considered including observers which could be used in place of the low pass filter and would potentially provide significantly more information. For example, it is possible that the observer could provide coil position information permitting "on the fly" correction for coil position. These strategies were not implemented because they were not necessary.

1.1.3 Inverter Models

- *Switching harmonics as a function of bus characteristics (filtering, line inductance and capacitance, voltage level, and substation spacing).*
- *Harmonics for each control option.*
- *Acceleration, coasting, regenerative braking.*

The control models described in subsection 1.1.2 were used to study approaches to controlling the standard configuration H-bridge inverter. The harmonics for the baseline control alternative were presented in subsection 1.1.2 and the bus losses were presented in subsection 1.1.1.

Figure 1-12 shows the inverter switch states for the baseline PWM inverter option (positive current states). The on-state (positive case) represents the application of the bus voltage to the coil. Off-state A and off-state B present cases where the coils are shorted and are acted upon only by the back EMF, the resistive drop of the coil and the power semiconductor drops. The

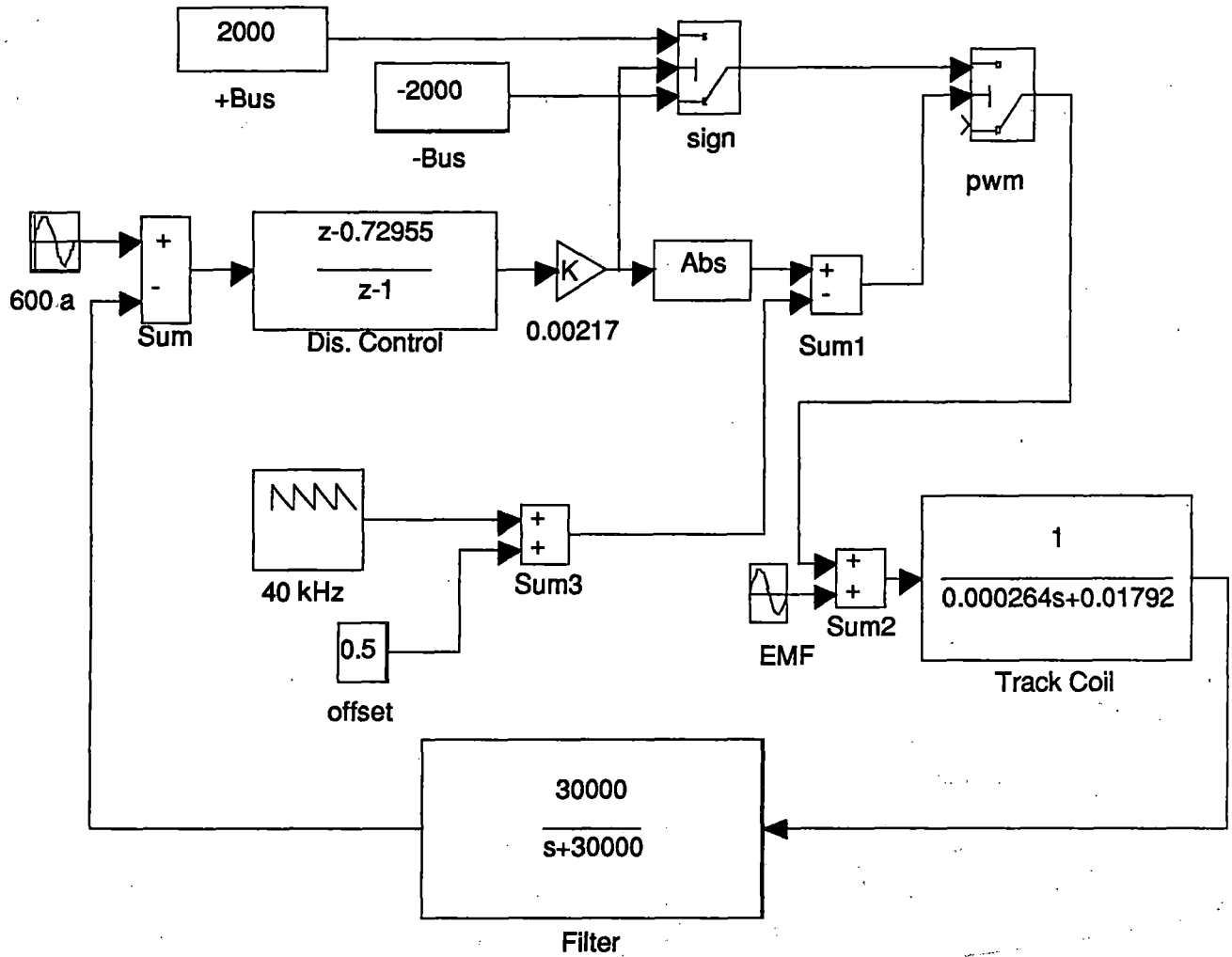


Figure 1-9. Simulink model of PI control system

last state, on-state (negative) is the case of the bus voltage being applied in opposition to the current flow. The latter case occurs only near a current zero crossing or during regenerative braking. For most of the normal drive cycle, switching occurs between the on-state positive and the off-state a or b conditions. Using both off state a and off-state b alternately reduces the duty on switches permitting a 40 kHz modulation using staggered switching elements individually operating at 20 kHz. For regenerative braking, switching occurs between the on-state and the "negative on state" in an alternating manner similar to the drive cycle except that instead of using the bus voltage to ramp the coil current against the back EMF, the back EMF is allowed to drive the coil current which is then switched into the bus to inject current against the bus voltage. The ability to utilize a 40 kHz switching frequency by alternating switching on 20 kHz switches reduces harmonic content at the expense of a very slight increase in control complexity.

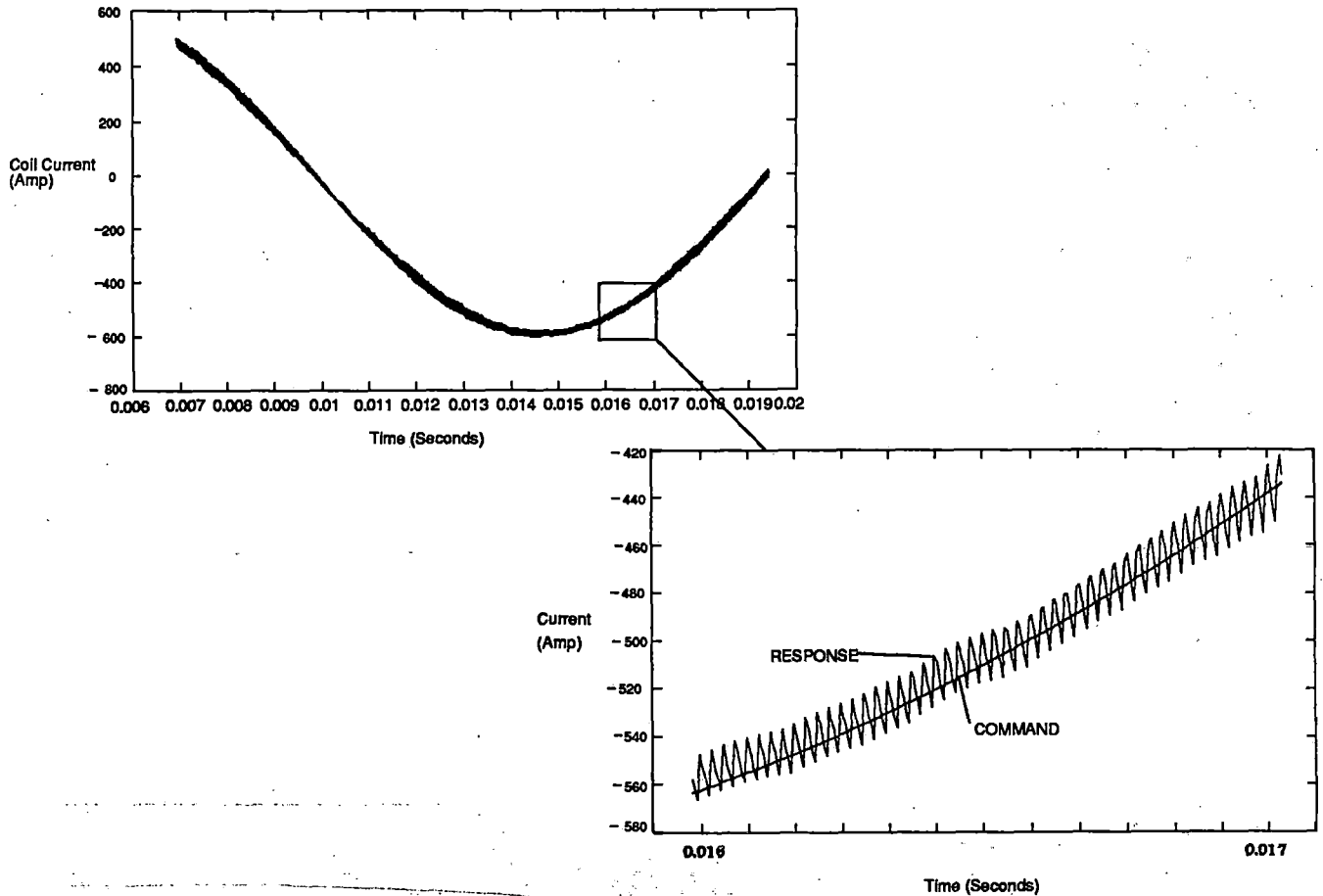


Figure 1-10. PI control system simulation

1.1.4 Ride Quality Requirements Review

The design study of coil geometry and control strategy requires a review of the ride quality requirements. The allowable thrust variation as a function of frequency will permit coil design and control alternatives to be compared. This study consists primarily of a review of prior work in this area.

Acceleration harmonic magnitudes of 0.06 g's appear to be acceptable at even the most sensitive frequencies. Figure 1-13 presents the rms acceleration levels from (2) which are permissible. In subsequent sections the thrust harmonics for the selected coil design will be calculated.

1.2 Tradeoff Analysis on Inverter Topology, Configuration, Switching Device Selection, and DC Bus Voltage Level

1.2.1 Single and Multilevel Bus Configuration Analysis

The multilevel bus configuration offers advantages in harmonics at the expense of additional switching elements, and additional bus and control complexity.

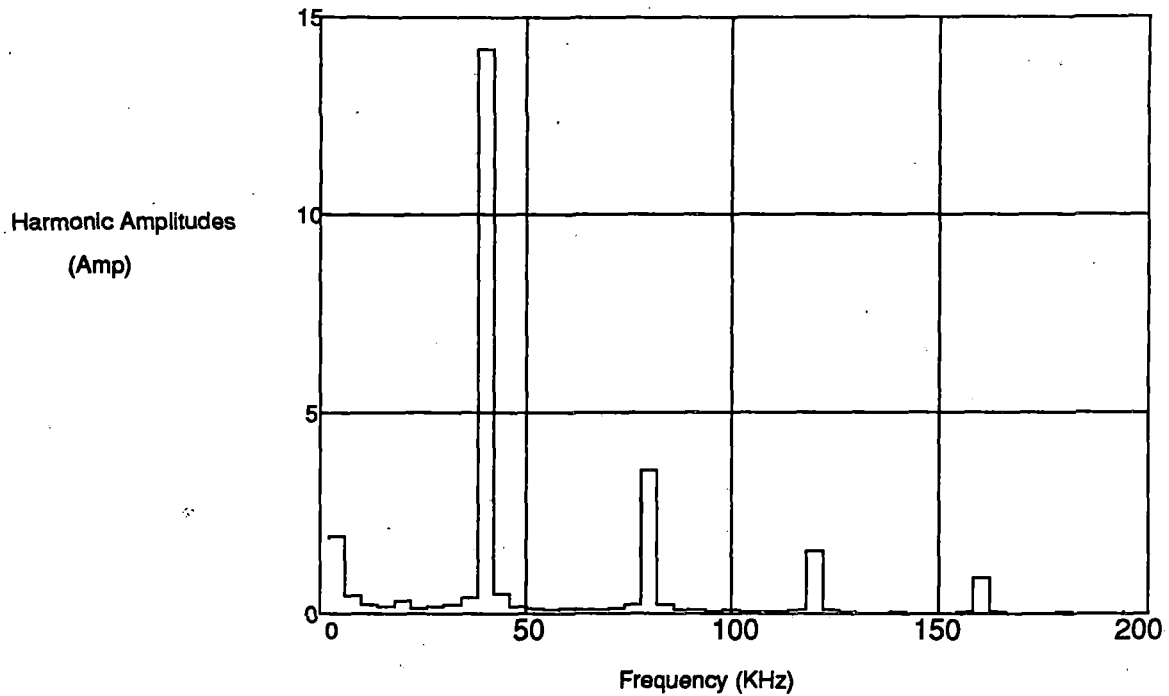


Figure 1-11. Harmonic content (40 kHz example at full speed)

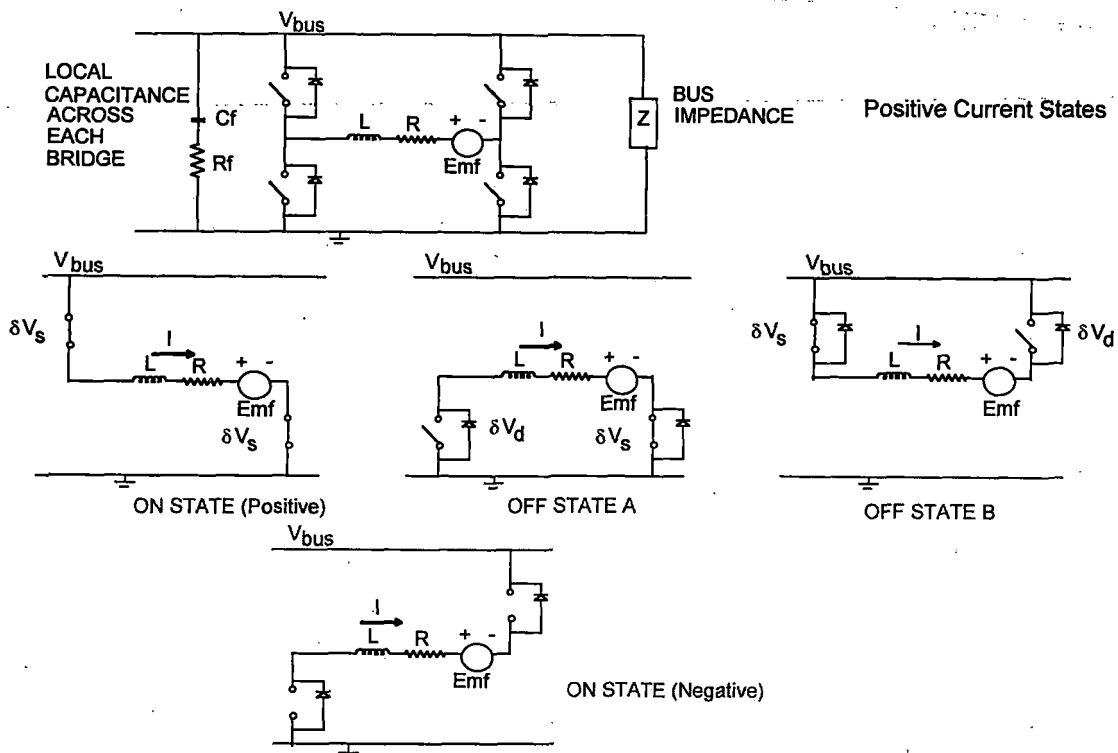


Figure 1-12. Switch states of full H-bridge configuration

"Information on this page identified by asterisk (*) in the margin is proprietary to Foster-Miller, Inc.

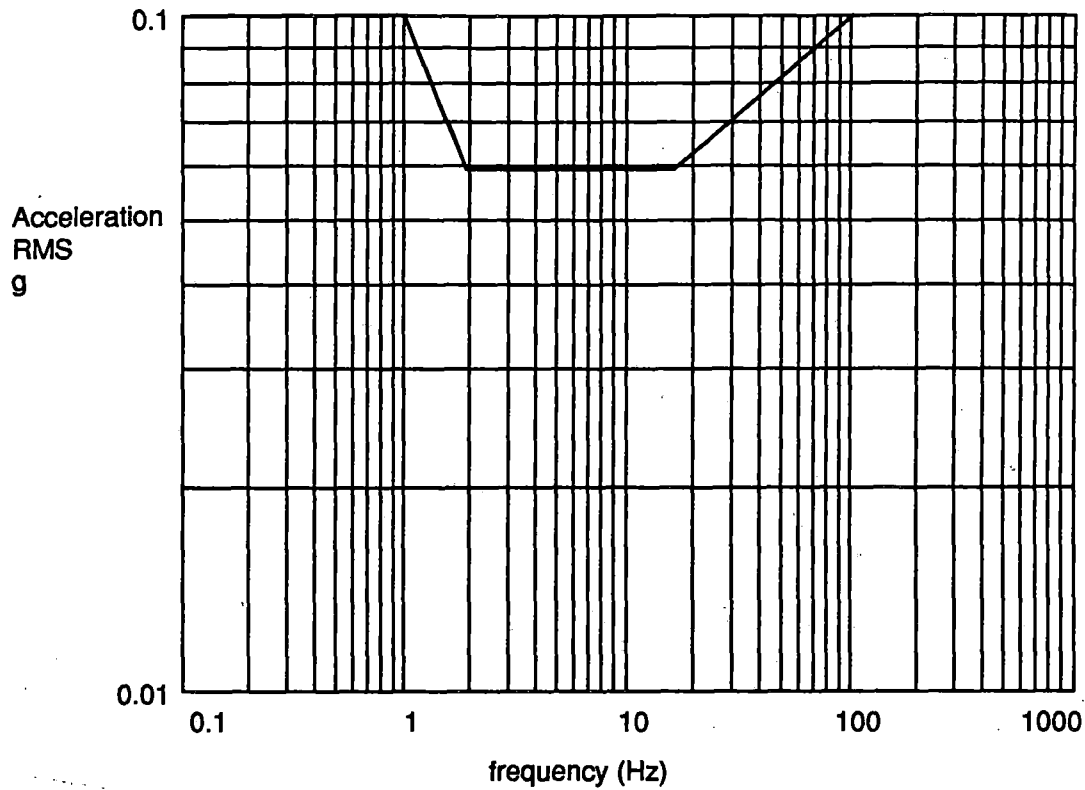


Figure 1-13. Permissible RMS acceleration levels (2)

A computer simulation study of the trackside inverter modules was performed. This study included the consideration of two specific bridge configurations, a single level inverter and a multilevel inverter (specifically a three level inverter). These are presented in Figures 1-14 and 1-15.

These configurations were analyzed in detail. The analysis included Pspice modeling of the elements in the inverter and determined device and bridge efficiency as well as the level of switching ripple. These factors are summarized in Table 1-3.

By alternating which device is switched the bridge can be operated at twice the frequency of the device. In the Pspice simulation, the ripple current harmonics were determined for each case. Pspice is an electrical circuit modeling computer program.

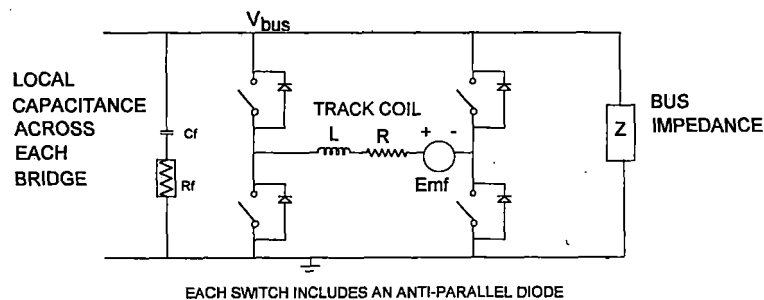


Figure 1-14. Single level H-bridge inverter topology

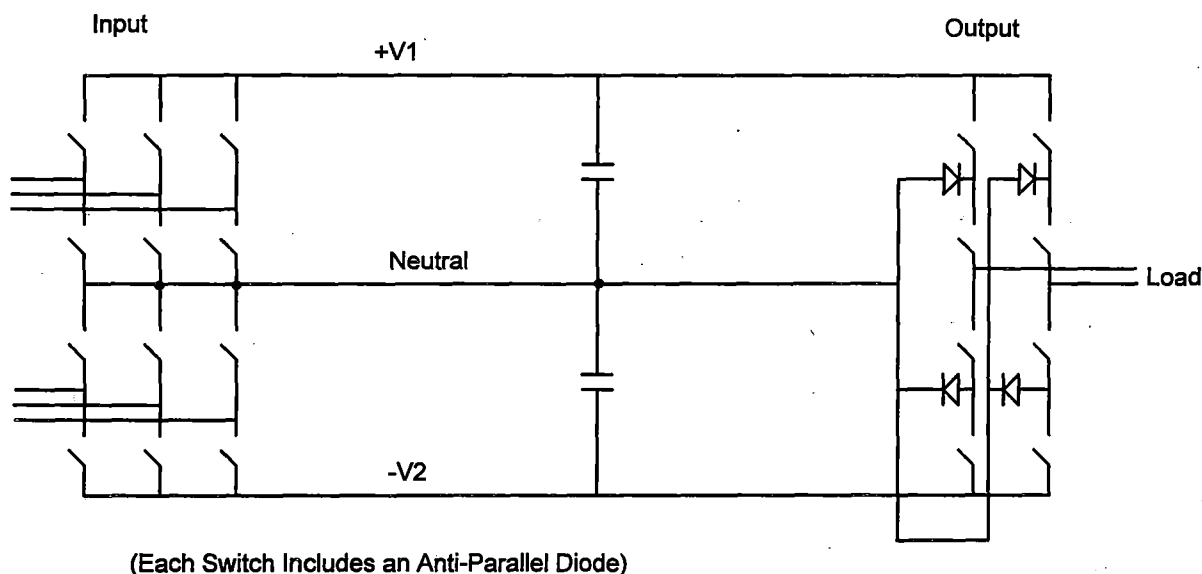


Figure 1-15. Multilevel inverter topology

Table 1-3. Summary of inverter topology study

Inverter Topology	Device Frequency (kHz)	Bridge Frequency (kHz)	Inverter Efficiency (percent)	Switching Harmonic (\pm percent)
Single level GTO	2.5	5	63	25
Single level IGBT	20	40	97	4.5
Single level MCT	10	20	90	5
Multilevel IGBT	10	20	98	7

The GTO (Gate-Turn-Off Thyristor) frequency was increased to reduce switching harmonics. It was set at a level that yielded the lowest harmonic which potentially could be accepted. At the selected frequency (2.5 kHz) the efficiency of the inverter is only 63 percent. A significant conclusion of the report is that the GTO cannot support the high switching speeds needed for this application.

The MCT (MOS-Controlled Thyristor) does poorly in applications where hard switching is required. This is reflected in the low efficiencies.

The IGBT (Insulated Gate Bipolar Thyristor) cases studied by GA clearly show the lowest switching harmonics and the highest efficiencies. The multilevel inverter system requires devices with half the voltage capability of the single level system but requires twice as many legs. The multilevel IGBT was operated at a bridge frequency of 20 kHz which was expected to yield the inverter harmonics for the 40 kHz single level inverter. The simulation yielded harmonic content considerably higher than anticipated. The disadvantage of the multilevel bus is that it requires three buses rather than the two required for a single level inverter. This represents a 50 percent increase in copper for a given bus voltage.

1.2.2 Device Selection Trade Study

GTOs, MCTs and IGBTs were compared for this application. Their relative advantages are summarized. The major issues include switching frequency and projected availability.

Subsection 1.2.1 includes summaries of both device and configuration selection. We have attached the specification sheet for Fuji 1MBI 400L-200 (Appendix B) which has a continuous current rating of 400A and a voltage rating of 2,000V. If the bus was reduced from 2,000 to 1,600V by decreasing the number of turns or by decreasing the coil area, the peak coil current for 0.25g thrust would be 1,136A necessitating three devices in parallel for each leg of the bridge per coil. A peak thrust requirement of 0.17 g's could be supported by two devices (800A) per leg per coil. Power limits set in the system design specifications limit acceleration to below 0.17 g's for speeds over 50 m/sec. It is therefore apparent that IGBTs available today can be used to meet the system requirements. Near term improvements will permit the use of a 2,000V bus.

1.2.3 Trade Study Summary

In summary it appears that the GTO has inadequate switching speed for this application. IGBTs are closer than MCTs to achieving the desired currents and voltages. The switching harmonic generated with IGBTs appears to be acceptable. Based on our analysis and the results of the GA study, the IGBT is our selection for inverter switching components in the full-scale system design. Further detail on the component selection process follows.

Table 1-4 presents a general comparison of the components under consideration for this application (expanded to include the MOSFET for the scale model). The GTO has the required voltage and current ratings required for this application but the switching losses were high. This high switching loss limits the allowable switching frequency. The higher switching frequency of the IGBT reduces the switching harmonic currents (ripple current) for a given bus voltage. The resulting switching harmonics for each device have been included in Table 1-4 and, as can be seen, the GTO would yield very high switching harmonics as a fraction of the fundamental current.

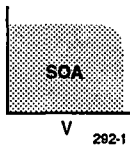
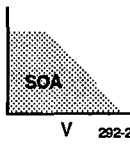
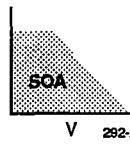
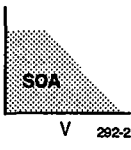
The impact of bus voltage and switching frequency on the harmonic content is summarized in Figure 1-16. It can be seen that there is a strong dependence on switching frequency over the range of interest. This analysis led to the selection of the higher frequency IGBT over the higher voltage GTO for this application.

The conclusions for each switching device can be summarized as follows:

IGBTs

IGBTs are the preferred switching device, at this time, for this application. Fuji has recently announced a 2,000V, 400A IGBT (1 MB1400L-200 IGBT 20 kHz, $V_{CE} = 2.7V$, $R_{thj} = 0.08 C/W$). IGBT components are approaching the requirements for full-scale implementation of LCLSM. Switching this device at 20 kHz would result in harmonics which are approximately 5 percent of the full thrust fundamental current for the case considered. Switching alternate devices at 20 kHz is equivalent to switching the inverter at 40 kHz. In this case the harmonics are approximately 2.5 percent of the fundamental current. The safe operating area (SOA) of this device is nearly square making these devices ideal for hard switching applications.

Table 1-4. Comparison of switching devices (3-5)

Characteristic	Parameter	IGBT	MCT	GTO	MOSFET		
Safe operating area	Forward current and blocking voltage						
		Thermal management	Conduction drop	1.7 to 3.2V	1.1V	1.1V	(Resistive)
		Switching loss	10 mJ/pulse	20 mJ/pulse	350 mJ/pulse	Very low	
		Junction temperature	150	150	125	150	
Circuit complexity	Gating method	Voltage	Voltage	Current	Voltage		
	Snubber	Optional	Required	Required	Optional		
	Series/ paralleling requirements	Proven	Difficult	Difficult	Proven		
Harmonic current generation	Device switching frequency	20 to 40 kHz	10 to 20 kHz	1 to 2 kHz	50 to 100 kHz		
	Bus voltage	2,000V	1,000V	4,000V	1,000V		
	Harmonic current	1.25 to 2.5 percent	2.5 to 5 percent	25 to 50 percent	0.5 to 1 percent		

MCTs

MCTs of only small power (1,000V, 75A) are available today but MCTs are rapidly undergoing development. The schedule for availability of high power devices with the required characteristics is being reviewed. MCTs are not favored in hard switching applications due to the degraded SOA of the device. This application does not utilize the low conduction losses, high surge current capacity and high di/dt capability so often cited as the MCT raison d'etre. The MCTs anticipated to be available in the near term are unsuitable for the configurations studied to date.

GTOs

GTOs have a large forward current and blocking voltage capability (3kA, 6 kV). Unfortunately they have a high energy loss per pulse and a complex gate drive. In addition to a large energy loss per pulse, the relatively slow turn-off process restricts GTOs to lower frequency switching applications. The air-core LCLSM motor has a relatively low inductance requiring fast switching for low harmonic currents. At a bridge frequency of 4 kHz the magnitude of the harmonic current relative to the fundamental current is 25 percent requiring a device frequency of 2 kHz. The GTO allows the bus voltage to be raised (desirable to reduce resistive power losses). To the extent that high harmonic currents are undesirable, based upon degraded ride quality, bogie fatigue and vibration and eddy current losses, GTOs do not seem well suited to this application.

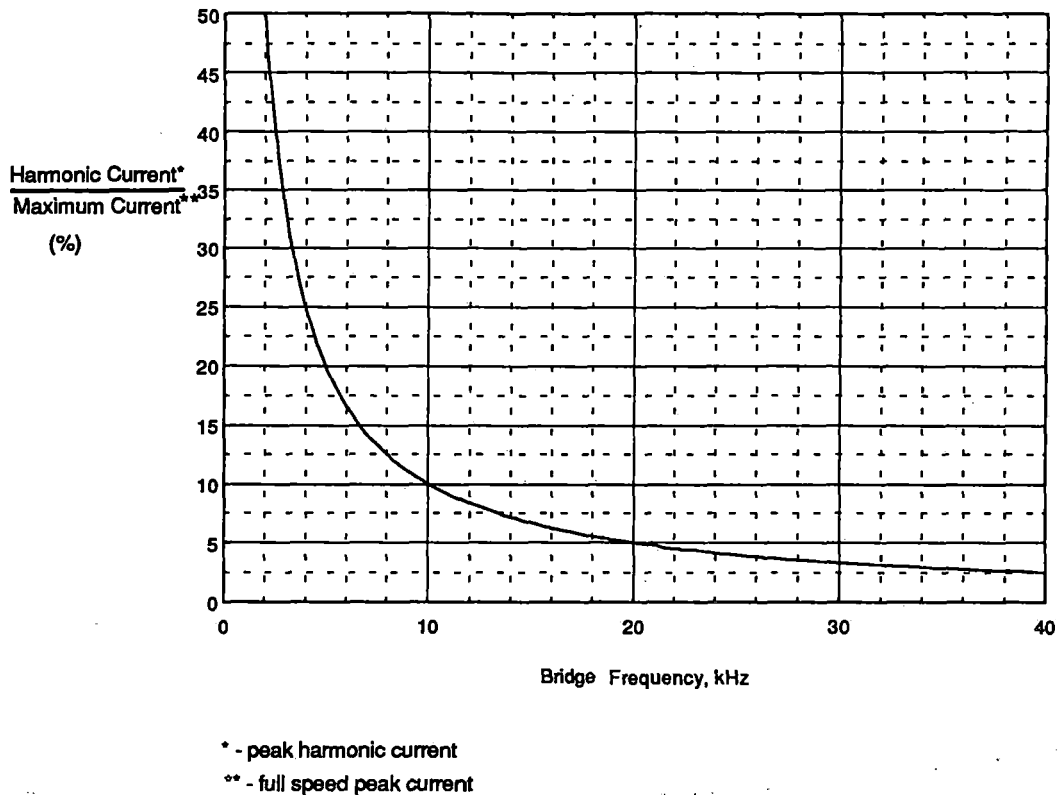


Figure 1-16. Switching harmonic versus switching speed

✓ **MOSFETs**

MOSFETs, as for MCTs, are available only in small power devices. In this case it is because the resistive characteristic of the device increases exponentially with increasing blocking voltage. Therefore, high voltage devices are usable only for low power. MOSFETs have been included in our comparisons for completeness and do not represent a realistic option for delivering the required propulsion power to the Maglev vehicle.

Conclusion

The IGBT is the preferred switching device due to its square SOA; low loss, high frequency capability; reasonable conduction loss; and convenient voltage gate control. Devices are available today with a rating of 2,000V, 400A and are expected in the near term to approach 2,300V, 600A levels. A bus voltage of between 1,700 to 2,000V results if the devices are used at 85 percent of their static blocking capability (common usage is >80 percent). If bus voltage fluctuations are severe the devices will need to be reduced in rating compared to their static blocking capability.

DC Bus Voltage Level

The DC bus voltage level has been determined based upon an analysis of the inverter performance (including power electronic switching device, bus voltage, and harmonic current levels). The result is a 2,000 VDC bus is preferred with IGBT switching devices operating alternately at 20 kHz providing ~2.5 percent harmonic currents.

1.3 Propulsion Analysis (Thrust Acceleration and Speed for 150 Passenger, 100 Mg, 40m long, 100 to 150 kN Thrust, 0.15 to 0.25g, Grades to 10 percent)

1.3.1 Utilize Task 1.1 Analysis to Characterize Conditions

- Thrust harmonics.
- I^2R .
- Eddy currents.
- Other losses.

The inverter and thrust models were used to characterize the parameters of the selected design point.

The thrust harmonics, resistive losses, and eddy currents were characterized for the full-scale design. The design of the propulsion system was based on the following areas which are covered in this subsection:

- Uniformity of thrust and field as seen by one SCM - as required to minimize the loads on the magnet support structure and to minimize the eddy currents seen by the low temperature members.
- Uniformity of thrust for the complete bogie - as required from ride quality considerations.
- Minimize losses including:
 - I^2R .
 - Eddy Current (vertical bar passing).
 - Eddy Current (switching harmonics).

* Thrust Harmonics

* Figure 1-17 presents the current and back EMF seen by a track coil as a function of the
* position for a set of four superconducting coils. The frequency of the current wave in the track
* is matched to be in synchronism with the passing superconducting coils. Figure 1-18 presents
* the back EMF from one SCM passing a track coil. The back EMF for this latter case has a
* much shorter apparent length than that for the full set of magnets. Smooth thrust is in

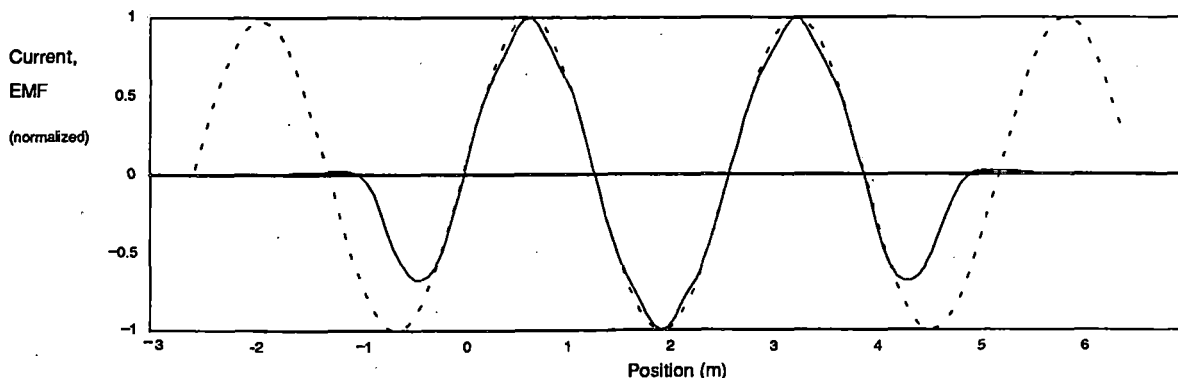


Figure 1-17. Track coil current and EMF versus position (four SC coils)

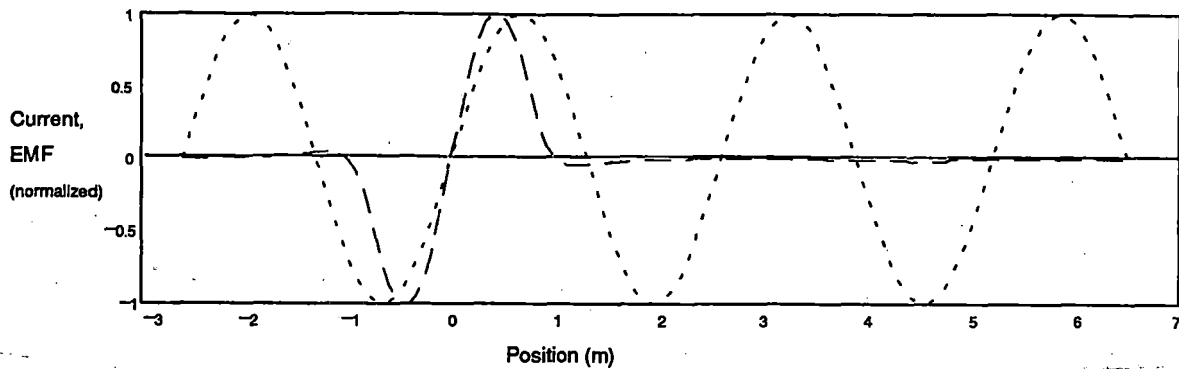


Figure 1-18. Track coil current and EMF versus position (one SC coil)

general achieved by spacing the track coils at 120 deg increments with respect to the back EMF wave. It is clear from Figure 1-18 that the requirement to provide smooth thrust for the individual coil requires a shorter pitch than could be used to provide smooth thrust for a larger set of magnets.

The baseline full-scale design was selected from these considerations based on a mean effective gap of 0.3m (coil center-line to coil center-line). The gap is not fixed and will vary with wind, cornering, and track tolerances. The thrust variation as a function of gap size for the selected design is presented in Figure 1-19. These thrust variations are well below those required from ride quality considerations.

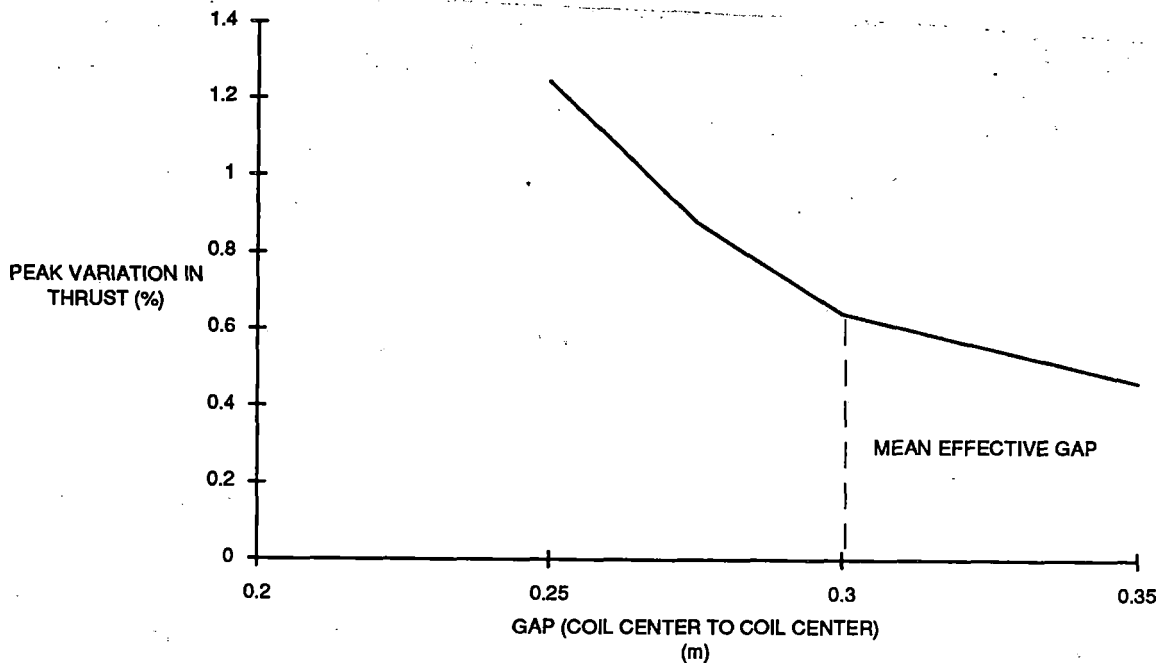


Figure 1-19. Variation in propulsion thrust versus gap

Table 1-5 presents the resistive coil losses for the cases of interest for the baseline full-scale design. The efficiency of the track coil exceeds 94 percent even at the peak thrust condition which is an infrequent event. Analysis of a particular route will determine if larger cross section coils are warranted in areas where peak thrust is frequently encountered.

Other electrical losses include eddy currents in the shield of the superconducting magnet. An ideal machine would have no losses in the shield because the flux wave produced by the track coils would be in synchronism with the SCM. In practice losses in the shield result from harmonics in the track coil currents (asynchronous currents) and from nonidealities in the track coil construction. When the vertical bar portions of the track coils pass the magnet shield, image currents are produced in the shield. These image or eddy currents result in losses.

Figure 1-20 presents the variation in fields seen by a point on the SCM as a function of the position of the SCM.

The following analysis is based on reference (6). The currents penetrate the shield based on the conductivity of the shield and the incident frequency. The bars pass at a frequency approaching 200 Hz and the shield is constructed from aluminum alloy with a thickness of approximately 1.5 cm. For the frequency of interest, the currents in the shield are inductively limited to a low value. For all 24 SCM shields, the losses are estimated to be less than 4 kW.

Table 1-5. Track coil resistive losses

Accel (g)	Thrust (kN)	Coil Current (A) (peak)	Speed at 8.1 MW (m/sec)	12R Coil (kW)	12R/Power (percent)
0.25	245	909.00	33.06	431	5.32
0.15	147	545.40	55.10	155	1.92
	60	327.24	135.00	56	0.69

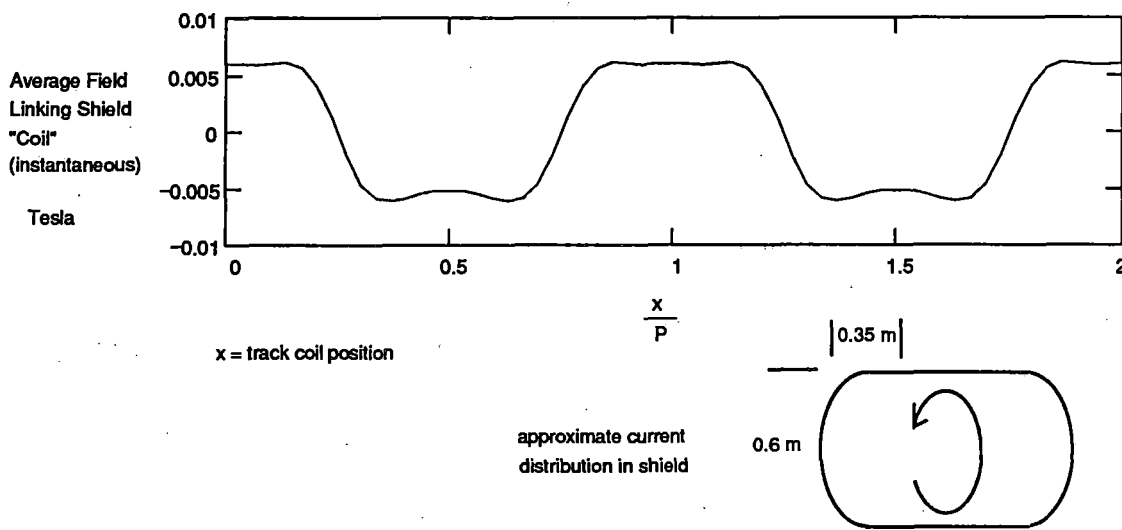


Figure 1-20. Shield eddy currents due to bar passing

$$\sigma := \sqrt{\frac{2}{\mu \cdot \frac{1}{res} \cdot \omega s}}$$

$\sigma = 0.55826 \cdot \text{cm}$ skin depth

$$\tau := \frac{\mu \cdot \text{rad} \cdot \sigma}{4 \cdot res}$$

$\tau = 0.01911 \cdot \text{sec}$ shield time constant

$$B_{\text{ratio}} := \frac{1}{[1 + (2 \cdot \pi \cdot v \cdot \tau)^2]^{0.5}}$$

$B_{\text{ratio}} = 0.04$ outer shield effectiveness

$$P := \frac{\pi \cdot \text{thick} \cdot \text{rad}^2 \cdot (2 \cdot \pi \cdot v \cdot \text{rad} \cdot Bp)^2}{8 \cdot res \cdot [1 + (2 \cdot \pi \cdot v \cdot \tau)^2]}$$

$P = 52.46 \cdot \text{W}$ eddy current loss per current loop in shield
3.8 kW in 24 magnet shields

The PWM harmonics in the track coil currents will also produce AC fields with respect to the SCM shield. The above equations can also be used to calculate the losses due to switching harmonics. This has been summarized in Figure 1-21 for a 40 kHz PWM frequency. If the harmonic current is maintained below 10 percent of the full thrust current, the harmonic losses will be negligible compared to other losses.

1.3.2 Determine Features and Parameters to be Verified in Testing

A sensitivity analysis will be used to determine the parameters which must be verified in testing. Transient conditions around the design point will also be investigated.

The analysis conducted to date indicates the following are the key parameters for modeling:

- Microcontroller timing cycle (control).
- Inverter switching speed/coil inductance (switching harmonics).
- Bus characteristics (bus voltage variation and efficiency).
- Thrust variation (ride quality).
- Geometric variations (coil placement and impact on thrust).

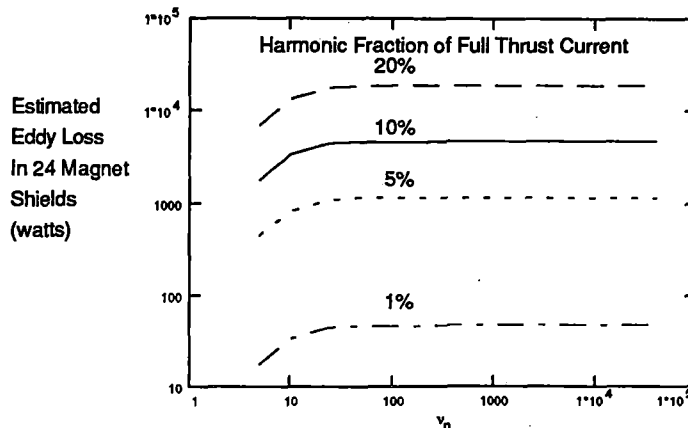


Figure 1-21. Harmonic losses in the shield

The timing cycle is determined by the speed of the microcontroller selected for the full-scale system and for the experiment. Based on the simulations, this parameter has a strong impact on the performance of the control circuit. The switching harmonics impact bus losses and eddy currents in the shield. The bus characteristics, including filtering, impact efficiency. Thrust uniformity will be impacted by the overall performance of the current control and by track tolerances.

* **1.4 Power Transfer**

* **1.4.1 Expand Power Transfer Model**

* *A simple model of the power transfer system will be developed for parametric studies. This model will utilize either MATLAB or MCAP.*

* The power transfer model consists of a coupling model between the track coils and a pickup coil on the vehicle. The length of the pickup coil is being selected to lap several track coils. The length is selected to minimize the change in total coupling to the excited track coils with time. Figure 1-22 presents the baseline configuration for the power transfer coil on the vehicle. The track coils are powered in parallel (in phase) by the local inverters to produce a 1 kHz AC field coupled to the power transfer coil. As the vehicle moves down the track new coils are excited as passed coils are turned off.

* The power transfer coil on the vehicle is connected to a rectifier on the vehicle as shown in Figure 1-23. Rectified current is supplied to the load. Multi-phase alternatives are also feasible but a single phase system will be sufficient to determine the requirements placed on the track coil inverter.

* The characteristics of the baseline power transfer circuit are summarized in Table 1-6. The transferred power level was selected to be within the range specified in the statement of work.

* **1.4.2 Parametric Studies**

* *The model was used to perform a study of the performance as a function of frequency and geometry.*

* There are only six track coils powered at any one time. As coils are turned off, new coils are added at the beginning. The mutual inductance between the powered track coils and the power transfer coil varies as a function of position. This variation has been minimized as shown in Figure 1-24, shown in exaggerated scale.

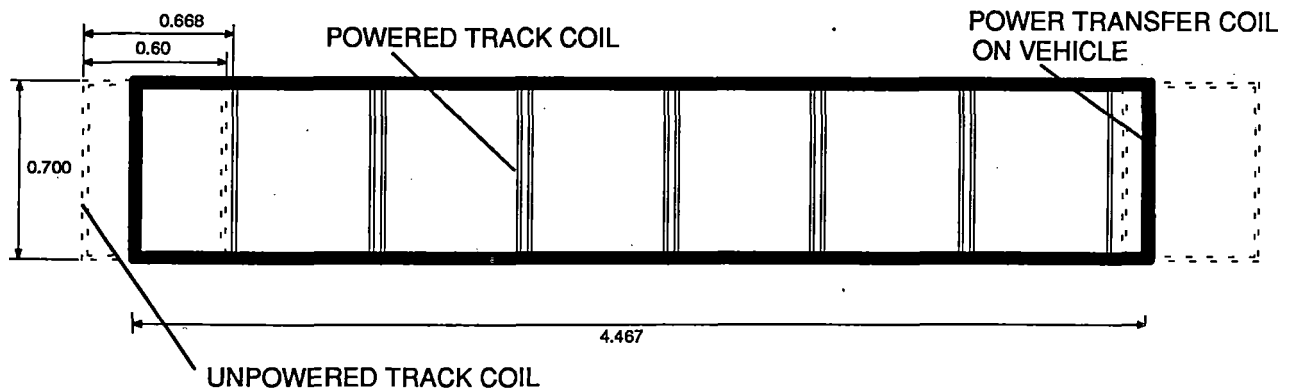


Figure 1-22. Power transfer configuration

"Information on this page identified by asterisk (*) in the margin is proprietary to Foster-Miller, Inc."

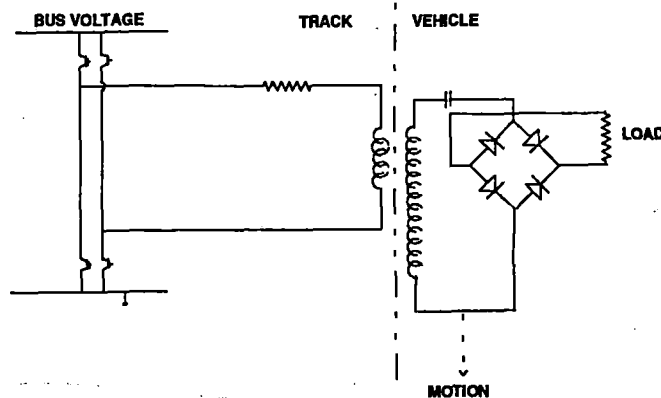


Figure 1-23. Power transfer circuit

The mutual inductance also varies as a function of the gap size. This is shown in Figure 1-25.

The change in mutual inductance changes the frequency for resonance in the power transfer circuit. Figure 1-26 presents the variation in parameters with the variation in mutual inductance. The voltage which is provided by the PWM function at the track is shown to increase with the mutual coupling. The required coil current to provide the nominal power transfer is shown to decrease with the mutual inductance. Both voltage and current are within an acceptable range for estimated variations in the mutual inductance.

1.4.3 Summarize

Foster-Miller will summarize the results of this study.

It can be concluded that the selected propulsion coils can be coupled effectively to provide resonant power transfer. In addition it appears that with proper design expected variations in mutual inductances with gap and coil position are acceptably small.

1.5 Scaling Laws (1/10 to 1/25th Scale)

1.5.1 Document Scaling Laws

The scaling laws for designing a 1/10 scale model based on a full-scale circuit design will be documented.

Table 1-6. Power transfer for baseline system parameters

Number of track coils coupled	6
Secondary coil	
Length	7 x track pitch
Height	0.7m
Number of turns	22
Section	4 cm x 4 cm
Inductance	0.00427 Henry
Resistance	0.055 Ohm
Avg. mutual inductance	7.74 10 ⁻⁴ Henry
Load characteristic	26.7 ohm
Load resistance	2.67 ohm
Load voltage	700.6V rms
Resonant capacitor	6 x 10 ⁻⁶ Farad
Peak voltage	9.9 kV peak
Resonant frequency	996.28 Hz
Track coil voltage	1,800V peak
Track coil current	147.7A rmsec
Power transfer	184.1 kW avg.
Efficiency	0.979

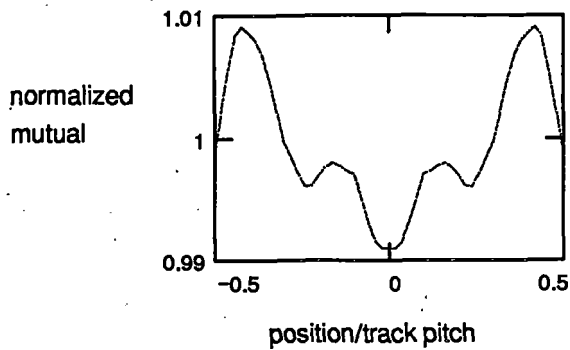


Figure 1-24. Power transfer mutual inductance variation with position

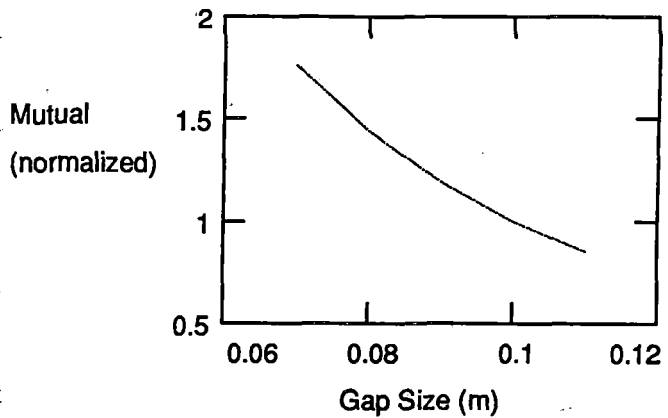


Figure 1-25. Power transfer mutual inductance as a function of gap size

The full and scale systems have been studied by directly calculating the key parameters including thrust and switching harmonics. Table 1-7 summarizes the scaling. The scaling can be estimated (with a fair degree of accuracy) by using the equation below from Nasar and Boldea (7) developed for three-phase block switched LSM. The LCLSM design has separate inverters powering each coil. These inverters are used to synthesize a synchronous flux wave in the track which is similar to that for a three phase block switched system. The scaling of the mutual inductances can be done by inspecting the Newman equation (8).

$$P \sim \frac{3}{2} \cdot M \cdot I_{sc} \cdot \omega_f \cdot I_{pc} \cdot nt$$

M is the peak mutual (one turn)
 I_{sc} is the ampere-turns of the SCM
 ω_f is the fundamental frequency
 I_{pc} is the peak track current (one turn)
 nt is the number of turns in the track coil
 P is the average power per SCM pole pair

$$M = \frac{\mu_0}{4\pi} \int \int \frac{1}{r} dl_{pc} \cdot dl_{scm}$$

M is the mutual between the field and track coils
 r is the spacing between elements
 dl_{pc} is a incremental length of propulsion coil
 dl_{scm} is an incremental length of scm

These equations were used to provide general scaling guidance in selecting a 1/10 scale design. The resulting 1/10 scale design was then analyzed using the same tools used to develop the full-scale system. The resulting scale system parameters appear to be within measurable ranges.

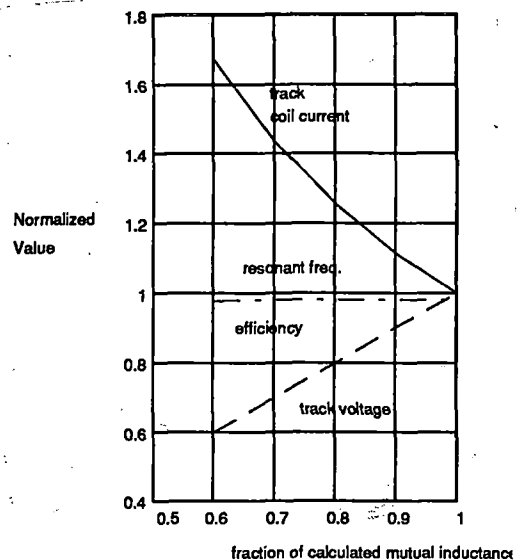


Figure 1-26. Power transfer parameter variation with mutual inductance

Table 1-7. Scaling summary

Variable	Approx. Scale	Actual Scale		Full-Scale Value	Scale Value
s	1/10	1/10	Geometry scaling	1	1/10
ω_f	1	1	Fundamental frequency	51.9 · Hz	51.9 · Hz
$V_{el} = \frac{2 \cdot p_{sc} \cdot \omega_f}{2 \cdot \pi}$	s = 0.1	0.1	Peak velocity	135 · m/sec	135 · m/sec
p_{pc}	s = 0.1	0.112	Propulsion coil pitch (modified by characteristics of pm versus scm)	0.6675m	0.0745 · m
p_{sc}	s = 0.1	0.1	scm/pm pitch	1.3 · m	0.13 · m
$M = \frac{\mu_0}{4 \pi} \iint \frac{1}{r} dl_{pc} dl_{scm}$	s = 0.1	0.18	Mutual inductance (four scm coils on one track coil)	$2.2 \cdot 10^{-7} \cdot \text{Henry/turn}^2$	$2.3 \cdot 10^{-8} \cdot \text{Henry/turn}^2$
l_{pc}	s = 0.1	0.1	Propulsion coil length	0.6 · m	0.06 · m
h_{pc}	s = 0.1	0.1	Propulsion coil height	0.7 · m	0.07 · m
A_{pc}	s ² = 0.01	0.25	Propulsion coil area, increased over scaling to permit increased duty cycle in the scale system	$4 \cdot \text{cm}^2 \cdot 0.9 = 3.6 \cdot \text{cm}^2$	$1 \cdot \text{cm}^2 \cdot 0.9 = 0.9 \cdot \text{cm}^2$
$V_{EMF} = M \cdot \omega_{ab} \cdot I_{sc}$	s ³ = 0.001	0.0012	Approximate EMF (where M is the peak amplitude of the mutual inductance)	133.79 · V/turn	0.161 · V/turn
nt	1	10	Number of turns	12 · turns	120 · turn
V_{EMF}			Peak EMF	$1.605 \cdot 10^3 \cdot \text{V}$	19.29V
J_{pc}	1	0.22	Current density in propulsion coil reduced to permit high test duty cycle	$3.03 \cdot 10^4 \cdot \text{A/cm}^2$	$666.67 \cdot \text{A/cm}^2$
$i_{pc} = \frac{J \cdot A_{pc}}{nt}$	s ² /nt = 0.001	0.006	Propulsion coil current (peak)	909 · A	5 · A

Table 1-7. Scaling summary (continued)

Variable	Approx. Scale	Actual Scale		Full-Scale Value	Scale Value
$\frac{L_{pc}}{nt^2}$	s = 0.1	0.052	Inductance is roughly proportional to the scale. In practice the coil cross section has a significant impact on the inductance	$1.91 \cdot 10^{-6} \cdot \text{Henry/turn}^2$	$1.03 \cdot 10^{-7} \cdot \text{Henry/turn}^2$
L_{pc}			Propulsion coil inductance	$2.75 \cdot 10^{-4} \cdot \text{Henry}$	$0.00148 \cdot \text{Henry}$
$\frac{R_{pc}}{nt^2}$	1/s = 10	0.388	Propulsion coil resistance	$1.04 \cdot 10^{-4} \cdot \text{ohm/turn}^2$	$1.03 \cdot 10^{-4} \cdot \text{ohm/turn}^2$
R_{pc}				0.015 ohm	1.48 ohm
$\tau = \frac{L}{R}$	s ² = 0.01	0.056	Propulsion coil time constant. Coil area was increased over simple geometric scaling to increase coil time constant	0.018 · sec	0.001 · sec
i_{sc}	s ² = 0.01	0.0096	Determined by properties of selected permanent magnet (1/10 physical scale)	$1.8 \cdot 10^{-6} \cdot \text{A/turns}$	17,300 · A/turns
$\frac{P}{I_{pc} \cdot nt} = 2 \cdot \left[\frac{3}{2} \cdot (M \cdot I_{sc} \cdot \omega_f) \right]$	s ³ = 1 · 10 ⁻³	$9.11 \cdot 10^{-4}$	Power per bogie side (2 scm pole pair) approximate expression (±10 percent)	$505.54 \cdot \text{W/A} \cdot \text{turn}$	$0.461 \cdot \text{W/A} \cdot \text{turn}$
P			Power limit on bus	$8.1 \cdot 10^6 \cdot \text{W}$	276.23 · W
$\frac{F}{I_{pc} \cdot nt} = 3 \cdot M \cdot I_{sc} \cdot \frac{\pi}{P_{sc}}$	s ² = 0.01	0.0091	Force per bogie (2 scm pole pair) (derived as power/velocity)	$3.745 \cdot \text{Newton/A} \cdot \text{turn}$	$0.0341 \cdot \text{Newton/A} \cdot \text{turn}$
F			Thrust limit per two pole pair	4.1 kN	20.46 · Newton
$i_{sw} = \frac{2 \cdot \pi}{8} \cdot \frac{M_{ab} \cdot \omega_f}{L \cdot \omega_{sw}} \cdot I_{sc}$	s ² /nt = 0.001	0.002	Switching harmonic estimate (peak based on zero bus voltage margin, 40 kHz example)	18A	0.037 · A

The general approach was to geometrically scale all dimensions. The superconducting field winding in the scaled system was replaced with a scaled block of permanent magnet material (with squared ends). The pitch of the track coils in the scaled system was adjusted to provide smooth thrust when operated with the permanent magnets. The number of turns in the scaled system was increased by a factor of 10 from the full-scale system to increase the back EMF to a level consistent with a 24V bus. Taps are included in the track coil to permit operation with a reduced number of turns.

1.5.2 Model 1/10 Scale Permanent Magnet Representation of the Field Winding

The permanent magnets were used to represent the field winding in the 1/10 scale model (both analytically using Amperes and physically by iteratively modifying magnets) to determine the pole shaping required to produce a back EMF wave similar to a scaled coil.

A 1/10 scale system was modeled assuming the SCM is replaced with a permanent magnet scaled to 1/10 the physical size of the superconducting coil (with squared ends). Figure 1-27 shows the single turn flux linkage to a 1/10 scale track coil. This was calculated using the Amperes code.

This flux linkage distribution was used to calculate the thrust as a function of position per ampere-turn in the propulsion coil. Multiple track coils were added to determine the total thrust and power as a function of track current. The pitch of the track coils was varied until the thrust and power were smooth. A pitch of 7.44 cm was found to yield smooth thrust and power. Figure 1-28 presents the power as one bogie with four permanent magnets moves one

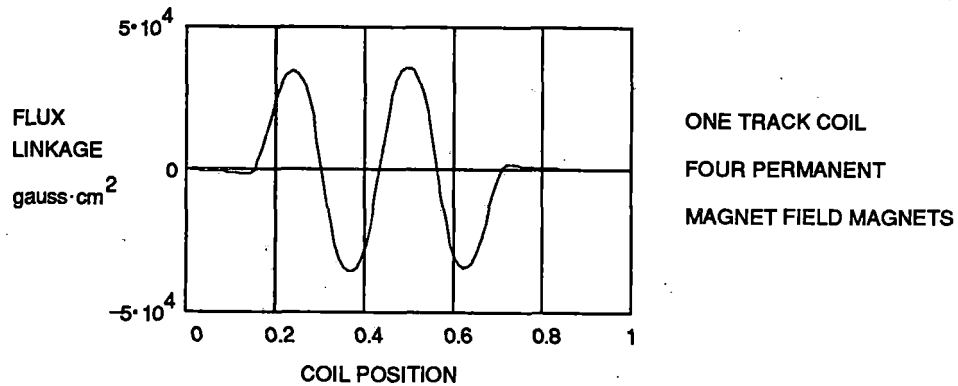


Figure 1-27. Scale system flux linkage

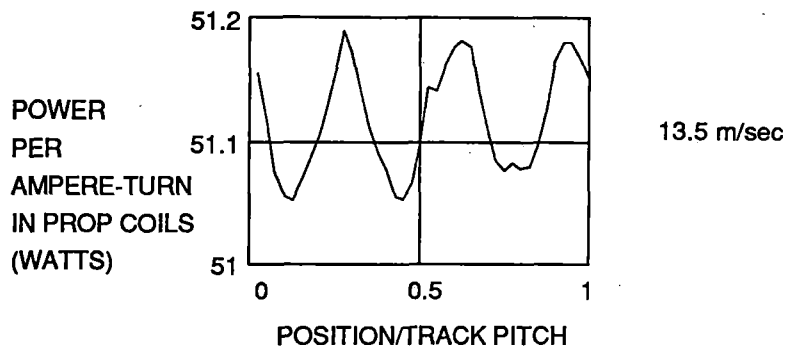


Figure 1-28. Scale system power

track pitch. Note that the calculated variation in power is less than 0.2 percent with the configuration selected.

1.5.3 Summarize Scaling Laws (Combine 1.5.1 and 1.5.2)

The results of the scaling law analysis and the permanent magnet models were combined to optimize the scaling approach.

The scaling was summarized in Table 1-7 and includes the analysis of the permanent magnets representing the superconducting magnets.

2. COMPONENT DESIGN AND ANALYSIS

2.1 Preliminary Full-scale Circuit Analysis and Preliminary Design

In the following subtasks, the full-scale design parameters were selected. This was the baseline which the 1/10 scale model simulated.

A simulation of the full-scale system including both local and central control was completed as a baseline for comparison to the scale system. Figure 2-1 presents the division of controls. A command for a specific velocity is received at the base processor which communicates to the local processors over a fiber optic link. The local processors control the current in the track coils to provide propulsion and power transfer.

Figure 2-2 presents the control blocks for the base station. The commanded velocity is compared to the estimated velocity to generate an error signal. A simple gain is used to

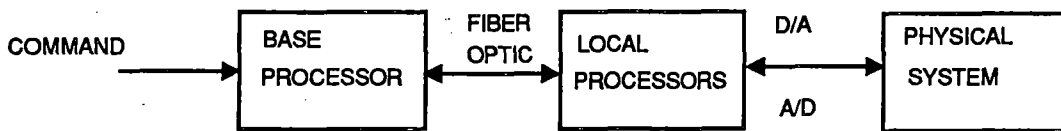


Figure 2-1. System summary block diagram

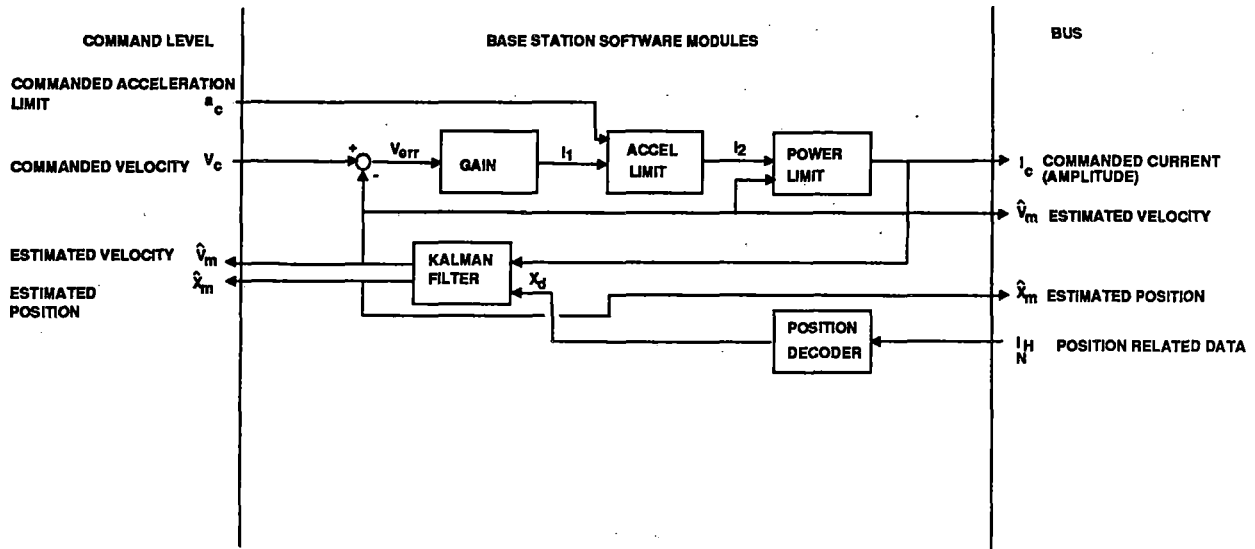


Figure 2-2. Base station control blocks

* develop a current amplitude command. This amplitude is compared to current amplitude limits for acceleration and power (bus current) limits. If required, the commanded current amplitude is reduced to be consistent with these limits. This amplitude and the estimated position and velocity are communicated to the local controller. The estimated position and velocity are generated by a Kalman filter which has measured position as an input. This position measurement is generated at the track coils and communicated over the fiber optic bus to the central controller.

* Figure 2-3 presents the general approach recommended for position detection. A shorted coil on the vehicle with the same dimensions as the track coil is shown moving past a track coil in this figure. The effective impedance of the coil pair is a function of the mutual inductance between the coils and therefore a function of position.

* The impedance looking into the track coil as a function of the position relative to the track coil was investigated to determine the sensitivity of this approach to position sensing. Figure 2-4 presents the results of this analysis for a 1 kHz source. If a 20 kHz, 1,800V square

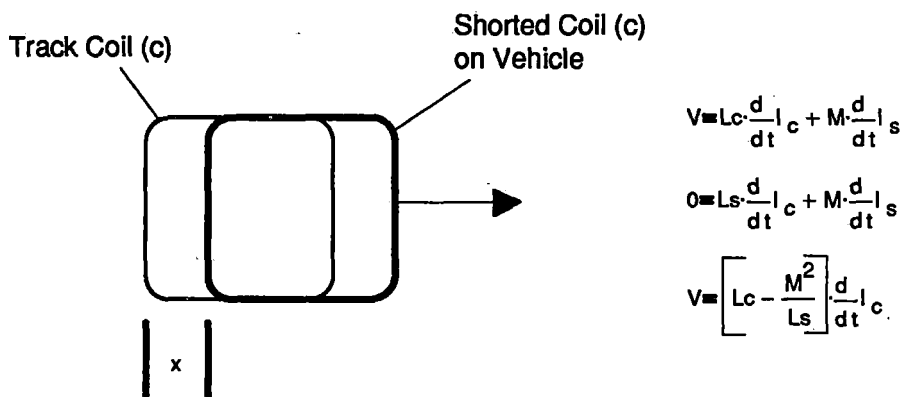


Figure 2-3. Position detection

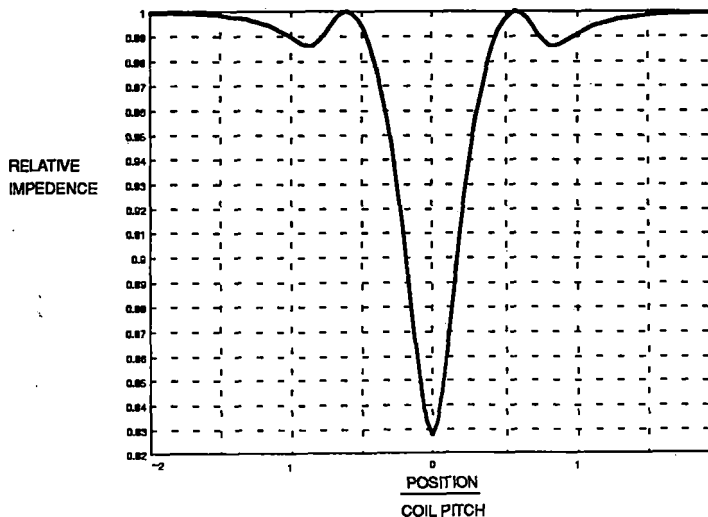


Figure 2-4. Relative impedance as a function of coil position

* wave is input to the coil, a current of approximately 50A would result. When aligned with the
 * shorted coil on the vehicle, the resulting current would be increased by 20 percent.

* The local controller functions are summarized in Figure 2-5. The commanded current
 * amplitude combined with the estimated velocity and position are the inputs to the local
 * controller. The position is used to determine the relative position to the center of the first
 * magnet in the first bogie. If the relative distance is small enough, a reference sine wave is
 * generated based on the position and commanded amplitude. The error between the command
 * and measured current is used as an input to the control block. In previous sections, a PI
 * control was described. In following sections alternate control strategies will be discussed, but,
 * for the purpose of comparing the performance of the full and scale systems, a PI control was
 * assumed. The amplitude of the output of the controller is used as the duty cycle input to the
 * PWM chip. The sign is used as a "direction" command.

* In Figure 2-5 the relative distance to shorted position coils on the vehicle is used to
 * determine whether a 20 kHz square wave should be generated to permit position sensing. The
 * harmonic current in the coil is measured and this measurement is sent over the bus to the
 * basestation processor where position is calculated.

* Figure 2-6 presents a portion of the Simulink model used to compare performance of the
 * full-scale and 1/10 scale systems. The position sensor was not modeled in detail and instead
 * was represented as a position signal with superimposed noise. The block labeled as "motor"
 * was modeled as 12 track coils which were used repeatedly to simulate a long section of track
 * with many track coils. When the vehicle moves far enough past a track coil that the coil does
 * not need to be excited anymore, the coil is numerically moved to the next available position in
 * front of the vehicle.

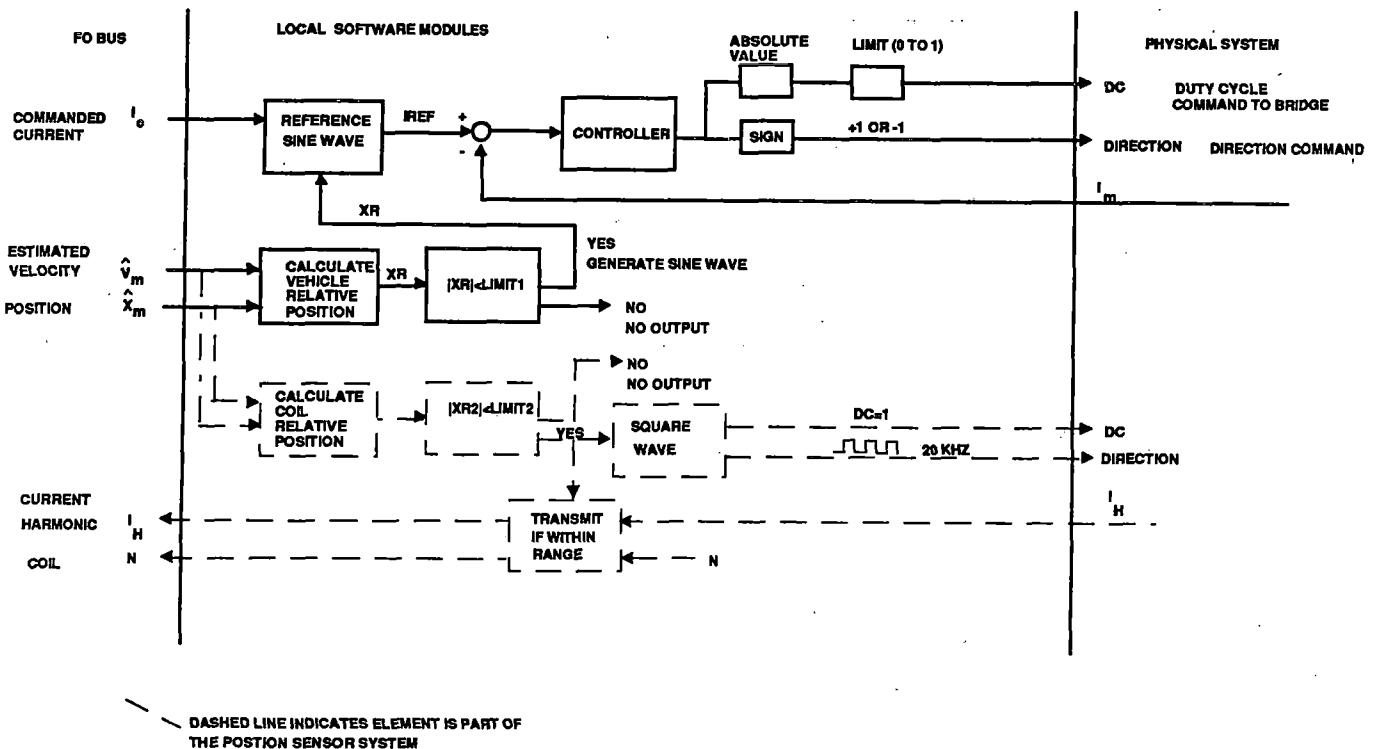


Figure 2-5. Local controller software blocks

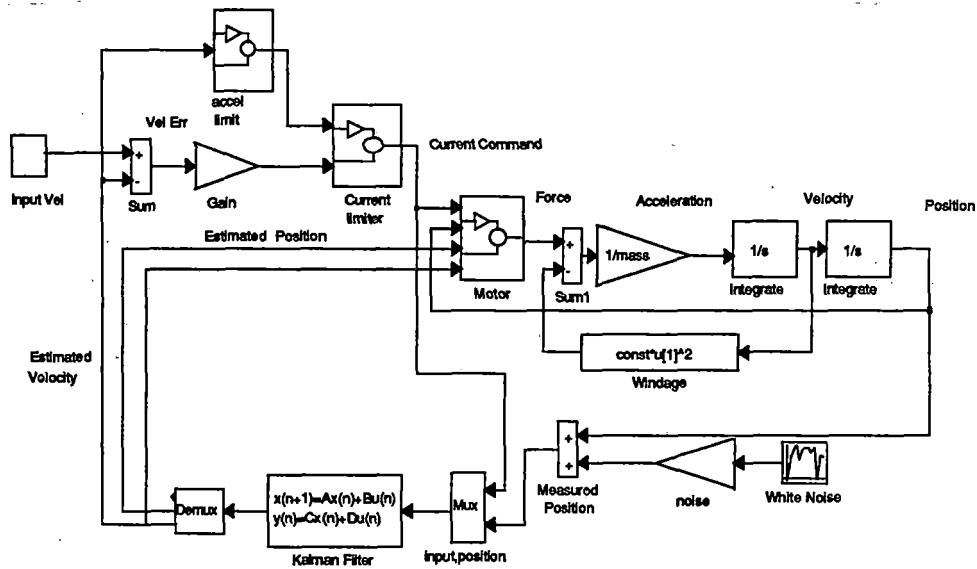


Figure 2-6. Base station Simulink model

Figure 2-7 compares the predicted performance of the full and 1/10 scale systems. All of the data presented in the figure has been normalized by the factors indicated underneath each variable. The case investigated consisted of acceleration from a standing start to full speed. The bus power limit requires a reduction in coil current as the speed is increased in the full-scale system. The scale system has sufficient bus and power supply capacity to not necessarily require this reduction in coil current with speed. The weight of the scaled system was selected to be low to permit rapid acceleration. These factors combine to result in a time to full speed in the scaled system which is a factor of 10 quicker than the full-scale system. This rapid time to full speed will be useful in demonstrating the stability of the control system. Since the operating range of the scale system encompasses the range of operation of the full-scale system, we can artificially impose bus current limits in software to simulate the requirements of the full-scale system bus.

2.2 Detailed Scale Circuit Analysis and Preliminary Design

The scaling laws and analytical tools will be used to determine the scale system circuit characteristics: inductances, resistances, mutual inductances and frequencies.

The analysis of the scale system included electromagnetic and controls modeling. We have used Simulink to investigate alternate control strategies for the current in the track coils. In the previous section the full and scale system overall performance were compared. In this section the basic configuration of the scale system model used to analyze the performance capabilities of alternate control strategies are described and the performances of the alternate control strategies are compared.

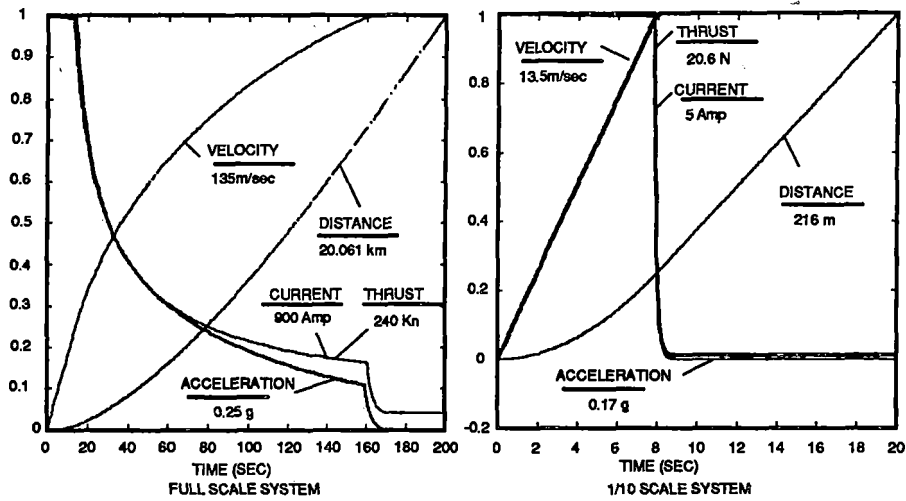


Figure 2-7. Full and scale system comparison

2.2.1 Description of Scale System Configuration Used for Controller Design

Figure 2-8 is a block diagram for the simulated control logic. The base processor coordinates the control of the local processors. It receives input through a serial port from a PC and can return test data over the same link. The PC is used in the system as a test interface only. The base processor also receives input from the system instrumentation including an encoder (position) and a load cell on the vehicle measuring acceleration. The base station sends commands to the local processors (only one shown) over the fiber optic links.

Figure 2-9 presents the software blocks for the base station in the 1/10 scale system. In this figure a PC is used to input commanded velocity goals and peak allowed acceleration in achieving the commanded velocity. The base station uses a Kalman filter to estimate position and velocity based on position inputs from the position encoder on the test motor. The estimated velocity is used to create a velocity error signal which is used to generate a commanded current subject to acceleration and power limits. A shaft encoder on the rotor will be used for most position measurements. A load cell on the rotor will measure thrust on the rotor and the data will be sent through the base station to the PC for display.

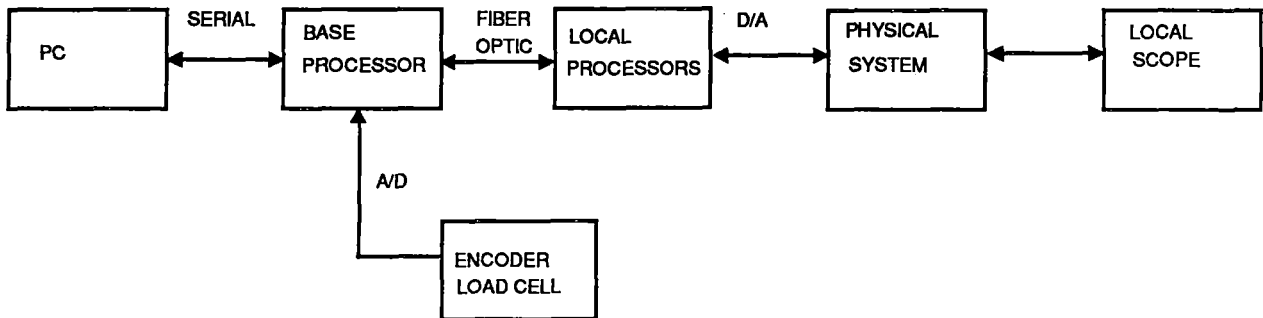


Figure 2-8. Summary scaled system block diagram

"Information on this page identified by asterisk (*) in the margin is proprietary to Foster-Miller, Inc."

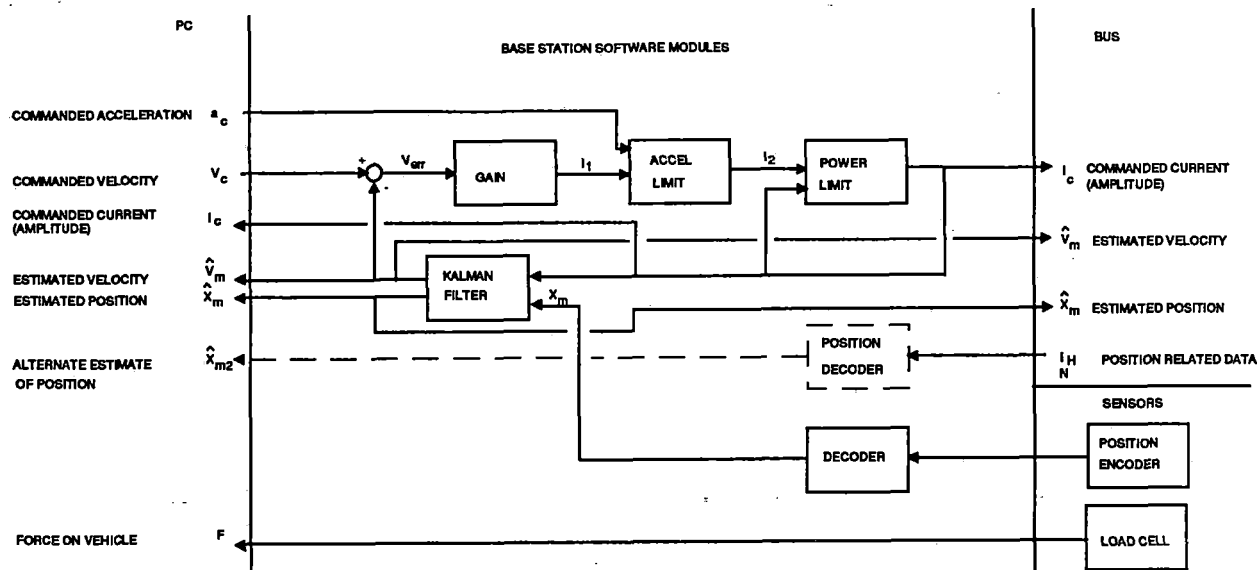


Figure 2-9. Base station blocks - 1/10 scale system

Figure 2-10 presents the local controller software blocks. The commanded current, estimated velocity and estimated position are used as inputs. The vehicle relative position (relative to the local coil) is used to determine when the coil should be powered. If the relative position is within the desired limits, a reference sine wave is generated based on the commanded amplitude and the relative position. The measured coil current is compared to the reference current wave and an error signal is generated for use in the controller. A duty cycle and direction signal are then generated for the inverter controller.

These models of the scale system were used to consider strategies for controlling the current in the track coils. The design problem is to develop a current controller which is responsive to the current command and is insensitive to disturbances including the back EMF (Figure 2-11).

2.2.2 Results of Controller Investigation

Three controllers were investigated. The first was the PI discussed in previous subsections (PI 1). A variation on this controller was investigated with increased damping (PI 2). An LQG controller was also investigated. This was designed using the controls package with MATLAB. The poles and zeros for these systems are presented in Figure 2-12.

Figure 2-13 presents the bode plots for the current and EMF response for the three controllers investigated. It is clear that the PI 1 has the fastest current response and best rejection of the back EMF. PI 2 with increased damping has slightly reduced response. The LQG was formulated without adding any integrators to the overall system. The result is a system which is type 0 and has finite error for a steady input. The LQG controller is not as responsive as either the PI 1 or PI 2 controllers. Not shown in these plots is the sensitivity to

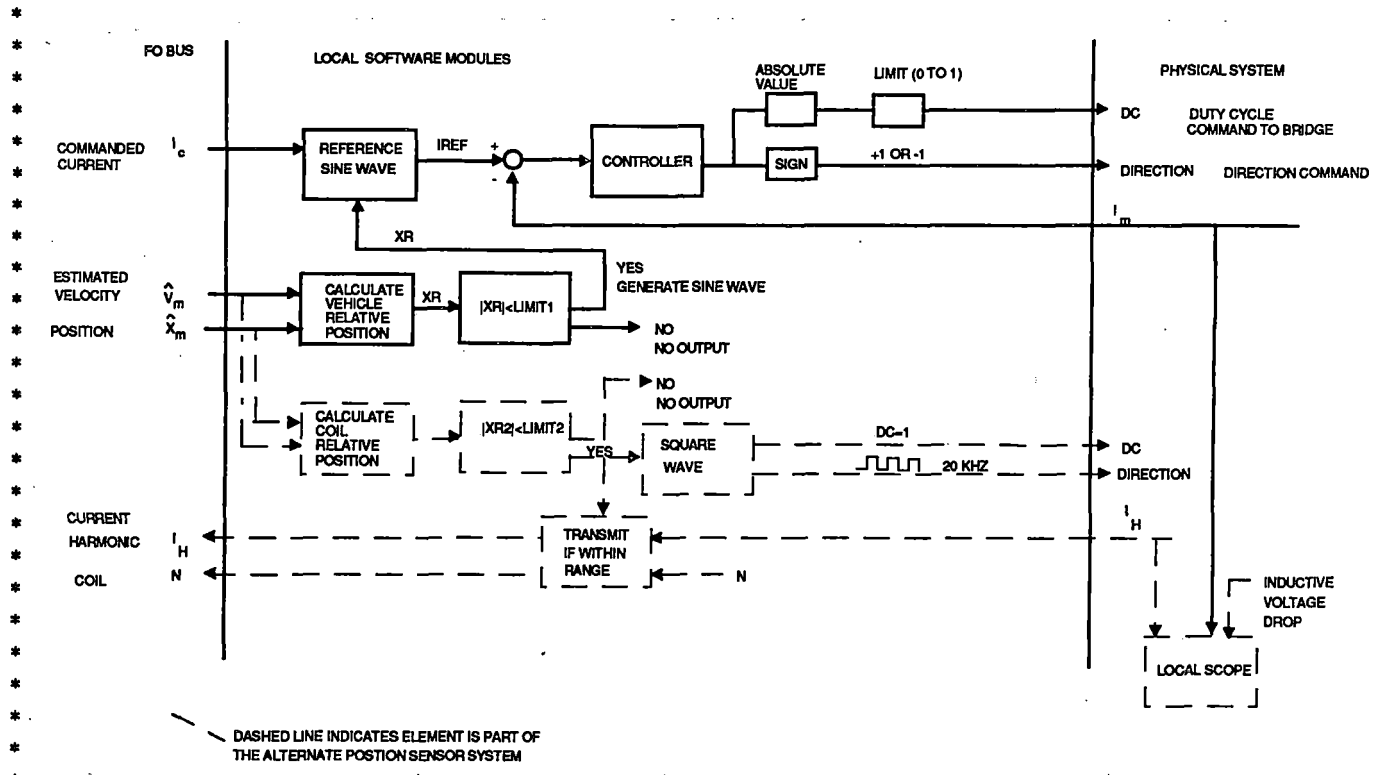


Figure 2-10. Local controller blocks - 1/10 scale system

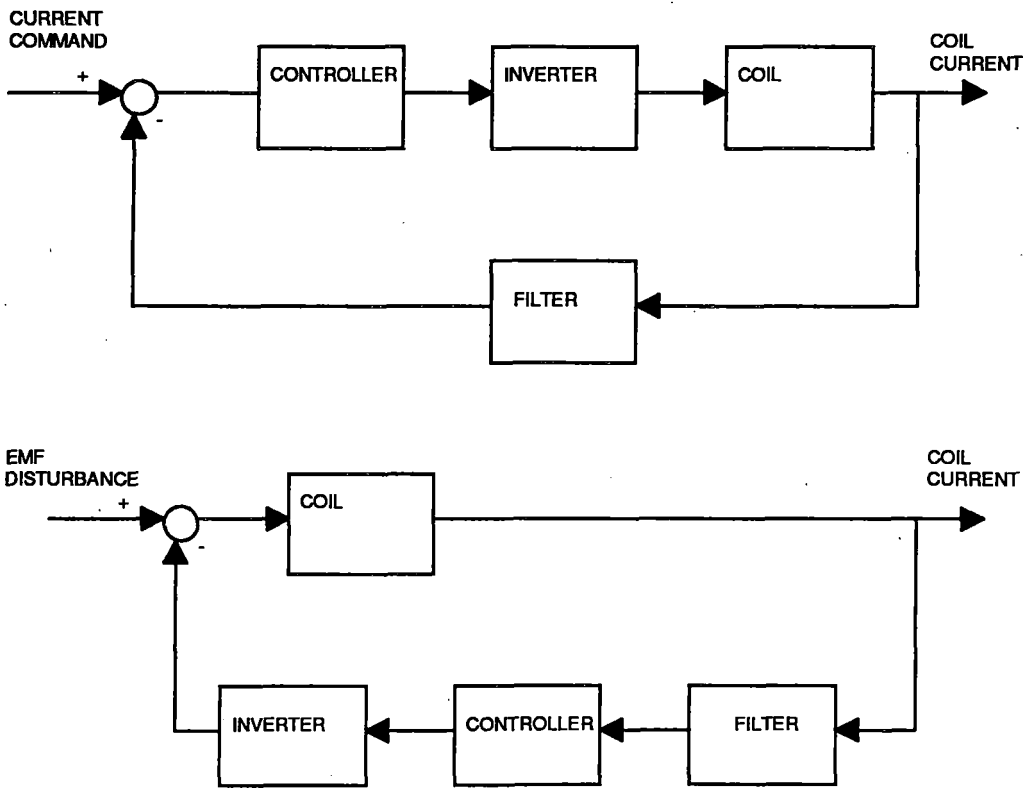


Figure 2-11. Current controller design

"Information on this page identified by asterisk (*) in the margin is proprietary to Foster-Miller, Inc."

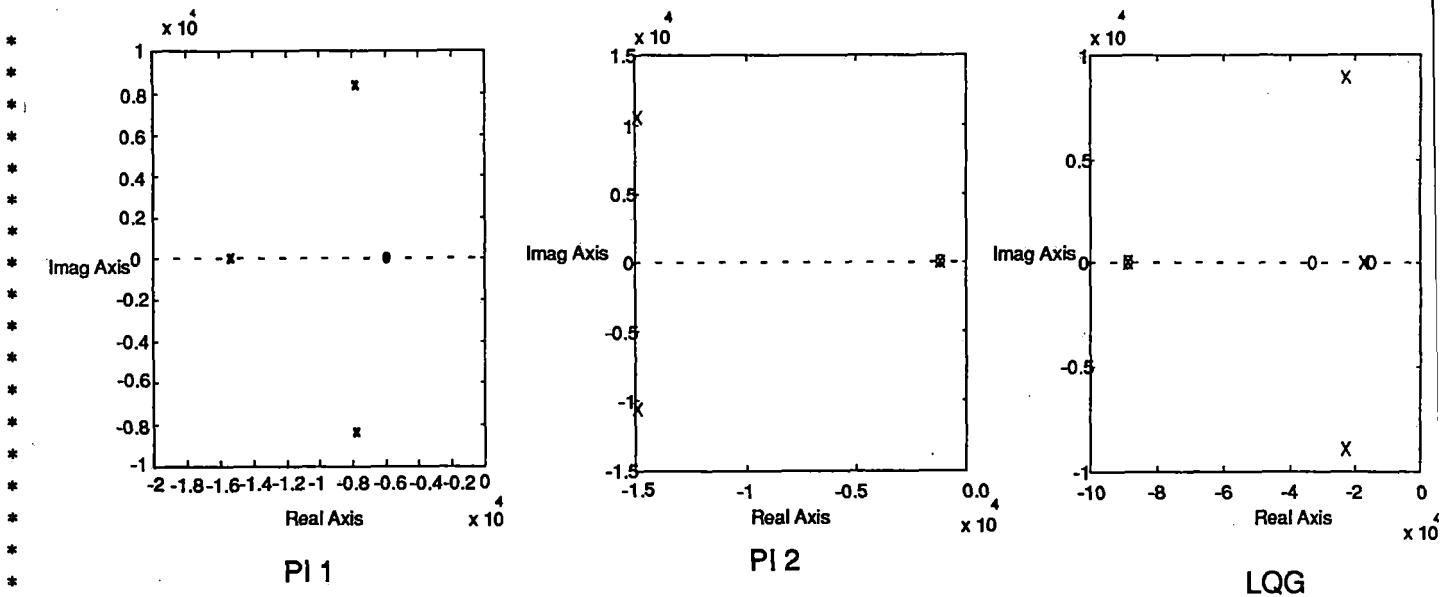


Figure 2-12. Current controller pole zero maps

* perturbations not included in the model. In running Simulink models using all three
 * controllers it was clear that the LQG is the most stable of the three controllers investigated.
 * Large perturbations in the commanded current resulted in a smooth approach to the correct
 * answer without oscillation.

* Figure 2-14 presents the calculated overall thrust for the 1/10 scale vehicle as a function of
 * the current control. The harmonic content appears acceptably low for all of the cases
 * considered. The LQG has lower thrust harmonic than the PI 2. The phase lag for the LQG
 * results in a 10 percent loss in output power (reduced power factor).

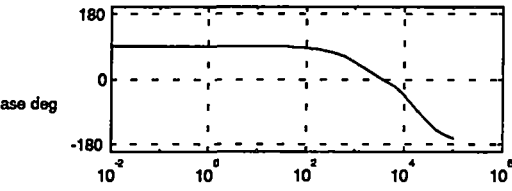
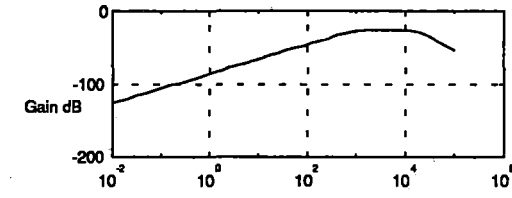
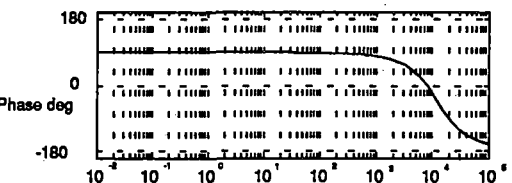
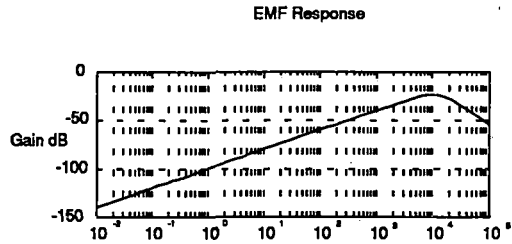
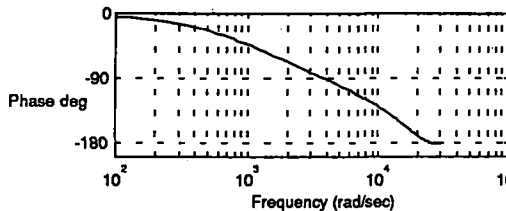
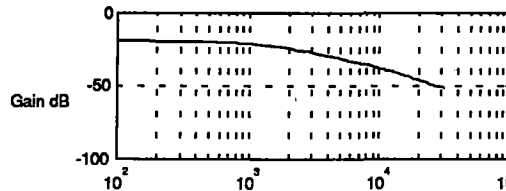
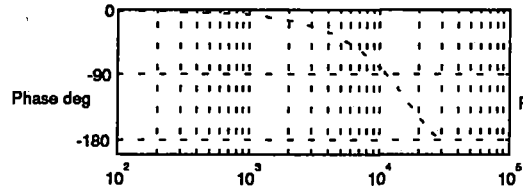
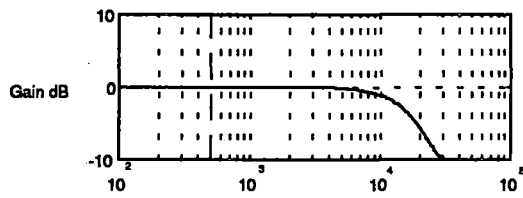
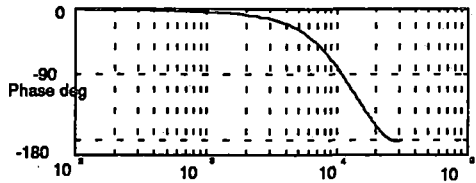
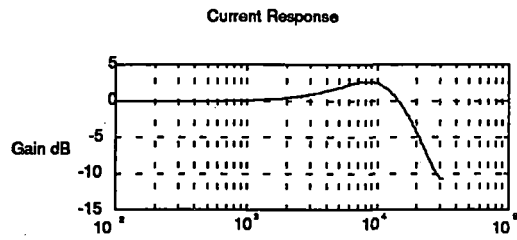
2.3 Design 1/10 Scale Experiment

The 1/10 scale system will be designed. This will include the mechanical design of the wheel and vehicle, coil design, and control system design. Verification of the inverter performance is a key experimental requirement which will be accounted for in the experiment design.

The design parameters of the 1/10 scale system are summarized in Table 2-1. Figure 2-15 is a photograph of the scale system. The track coils are mounted on blocks forming a 1.5m diam circular track. The vehicle includes four permanent magnets which simulate the superconducting field magnets in the full-scale system. The vehicle is mounted on a composite rotor which is mounted on its hub to a vertical shaft. The vertical shaft is the drive shaft of a permanent magnet motor which can be used as a load for the experiment. The inductances have been verified in component testing.

The rotor detailed design is summarized in Figure 2-16. The rotor structure is fabricated from high strength carbon fiber reinforced composite tubing. This structure was selected for light weight and high resonant frequencies. The vehicle is shown on the left in this figure. It consists of a housing clamping four magnets. It is supported from four pivot arms which are constrained by the load cell. Adjustable counterweights are shown on the right in this figure. The shorted coils used for position sensing are shown between the counterweights.

"Information on this page identified by asterisk (*) in the margin is proprietary to Foster-Miller, Inc."



PI 1

PI 2

LQG

Figure 2-13. Current control bode plots

"Information on this page identified by asterisk (*) in the margin is proprietary to Foster-Miller, Inc."

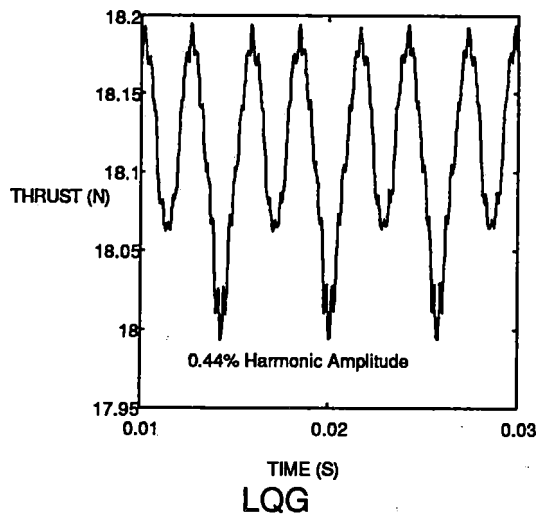
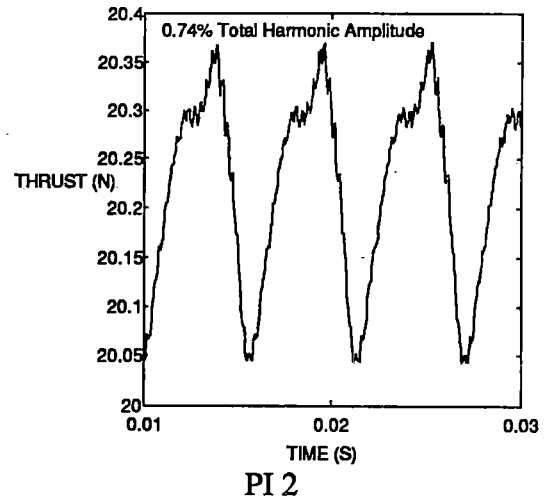
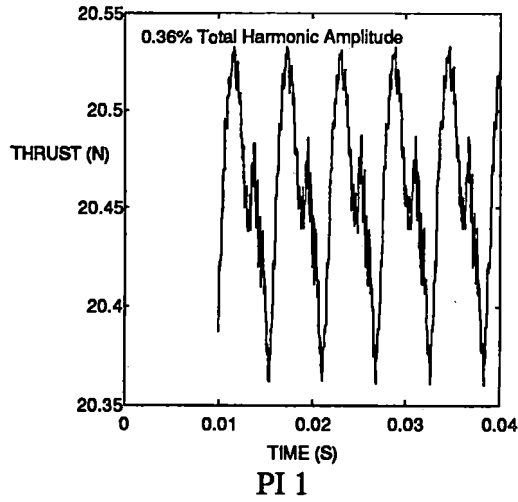


Figure 2-14. Thrust as a function of current control

The permanent magnets were modeled with Amperes to determine the field distribution and back EMF. The Amperes model yields the current distribution on the surface of the magnet which yields a field distribution which is equivalent to the magnet. For the assumed permanent magnet properties this corresponds to a surface current of 10,820 A/cm of magnet thickness. This results in a surface current of 17,300A for the 1.6 cm thickness used in the model. This magnet model was used to develop the scaling of the system model. To verify the performance of the actual magnet system we have tested the back EMF produced by one of the permanent magnets when swung from a pendulum (Figure 2-17) with an effective radius of 0.73m (similar to the experimental gap diameter). During this test the magnet achieved a velocity of 3.78 m/sec based on height of the drop.

Table 2-1. Scale model features

Permanent magnets	Quantity	4
	Pitch	13 cm
	Height	5 cm
	Length	1 cm
	Thickness	1.8 cm
Track coils	Quantity	64
	Turns	120
	Width	6 cm
	Height	7 cm
	Pitch	7.45 cm
Overall	Gap	3 cm
	Gap diameter	1.5 m

The permanent magnet was also modeled as a rectangular coil on the perimeter of the magnet using the Newman equation model used to design the full-scale system. The analytical and experimental results are compared in Figure 2-18. The agreement is good.

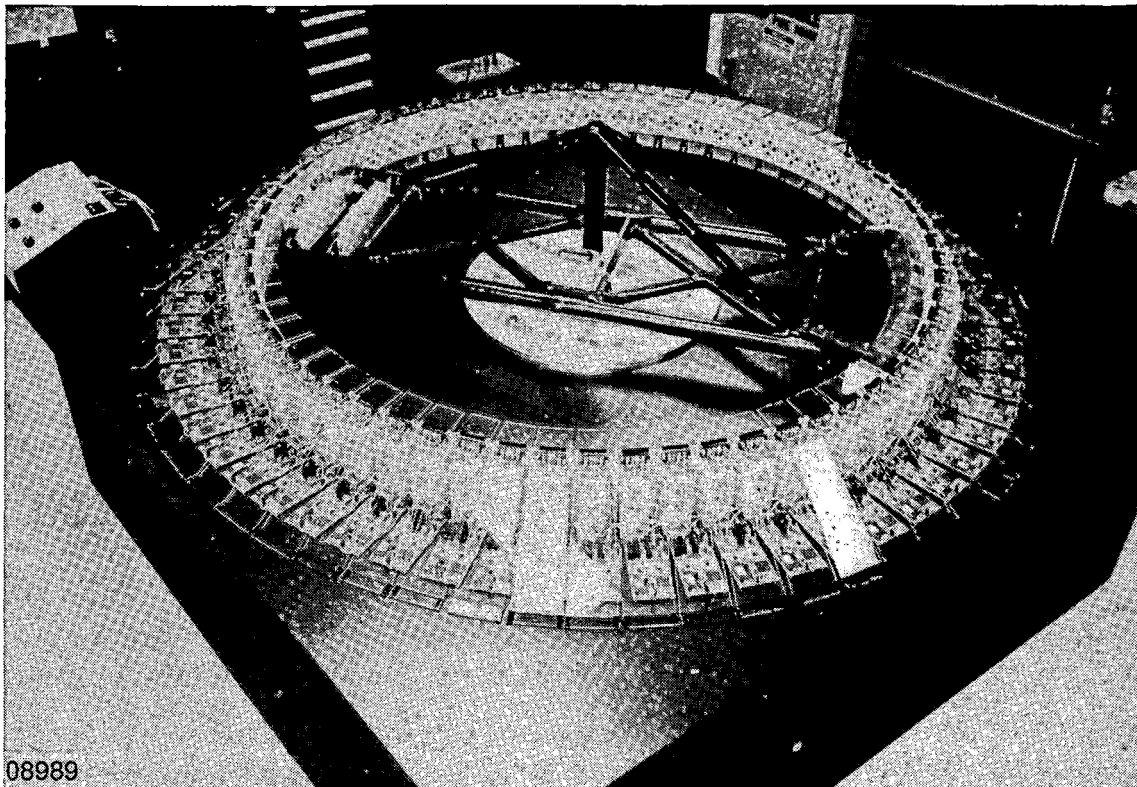


Figure 2-15. Scale system design

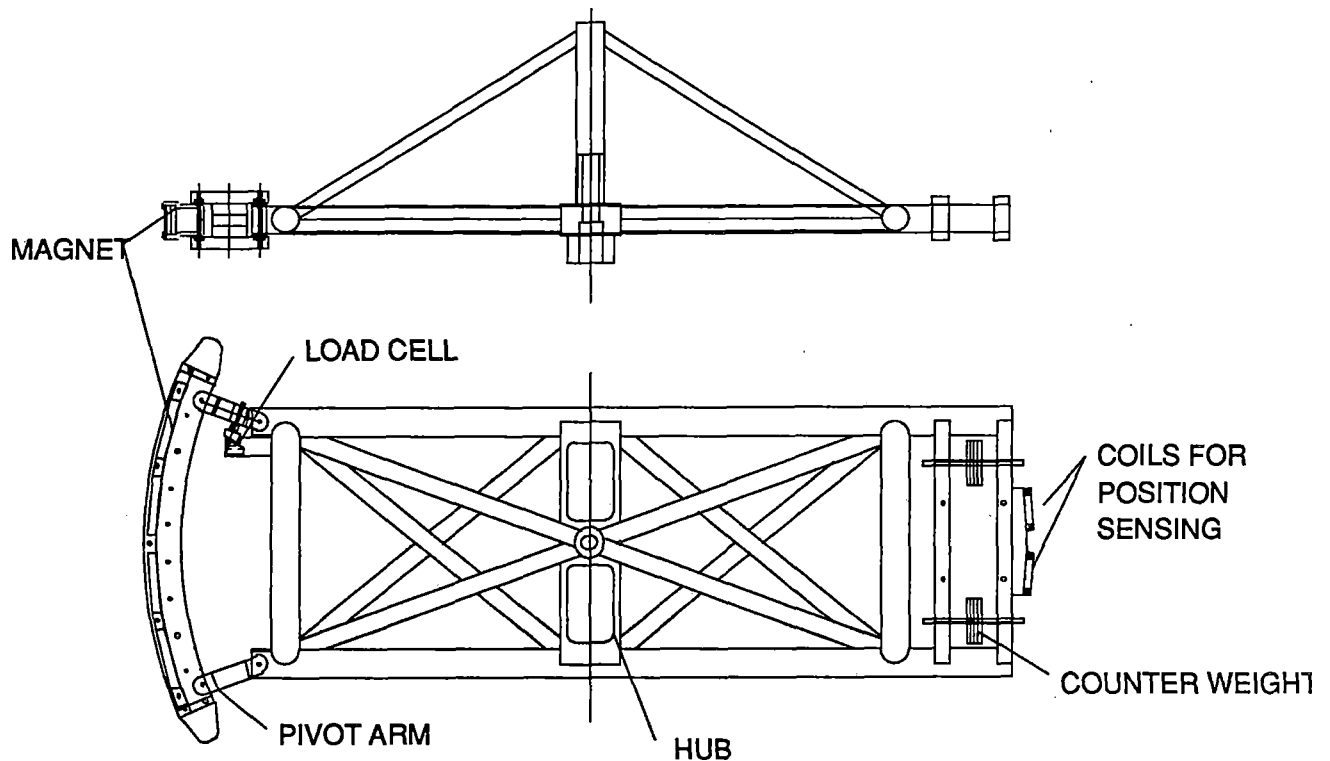


Figure 2-16. Rotor detailed design

The results for one magnet were summed to predict the performance for a set of four field magnets. This was done for the experimental results, the analytical results based on the Newman equation, and the numerical results based on the Amperes code. The results are presented in Figure 2-19 for the test speed of 3.78 m/sec. The results are in good agreement giving confidence to analytical and numerical calculations for the scale and full-scale systems.

The controller hardware block diagram is shown in Figure 2-20. This chart is consistent with the software module block diagram shown previously with the addition of analog inputs to the base station.

Figure 2-21 presents the controller board design. This board is used for the individual coils and in slightly modified form for the base station. It includes four amplifier circuits on the left which are used for current and voltage measurements. The controller is in the center of the board and the fiber optic interface is shown on the lower right of the board.



Figure 2-17. Back EMF testing

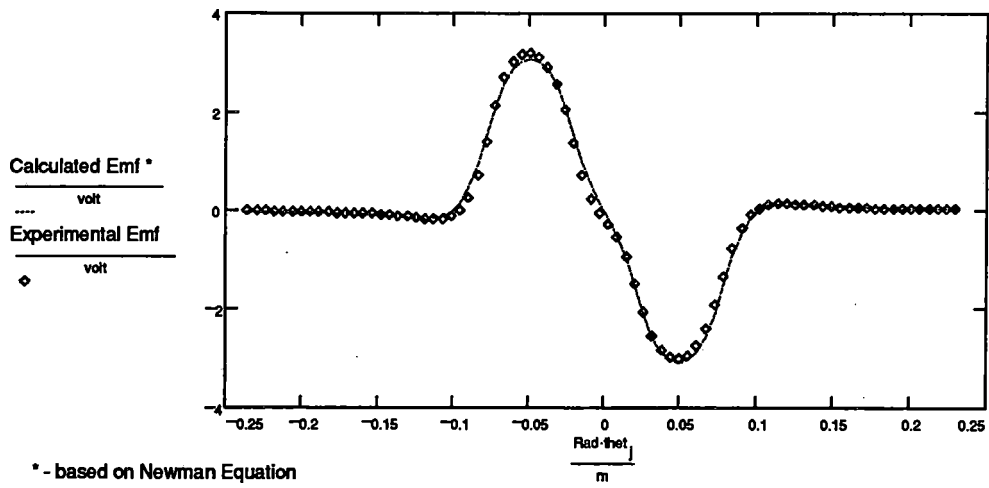


Figure 2-18. EMF test results

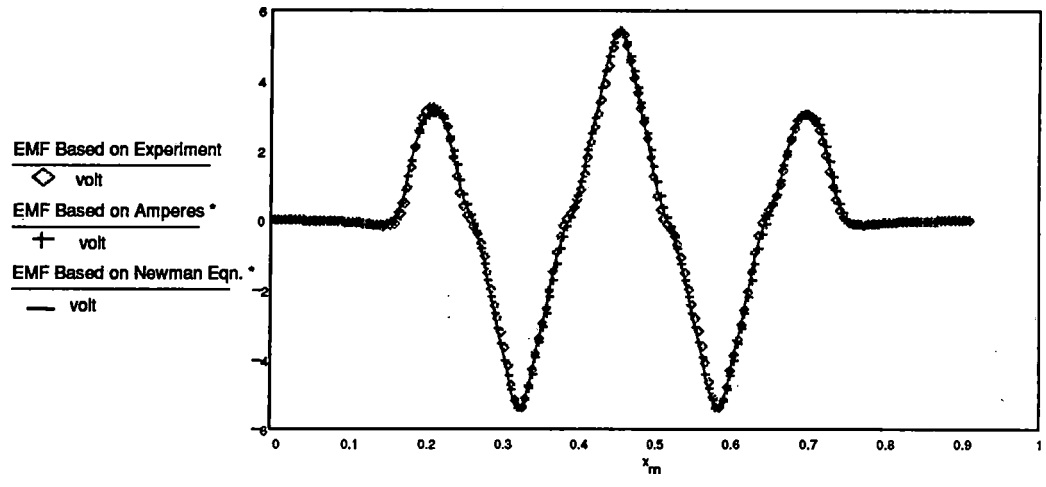
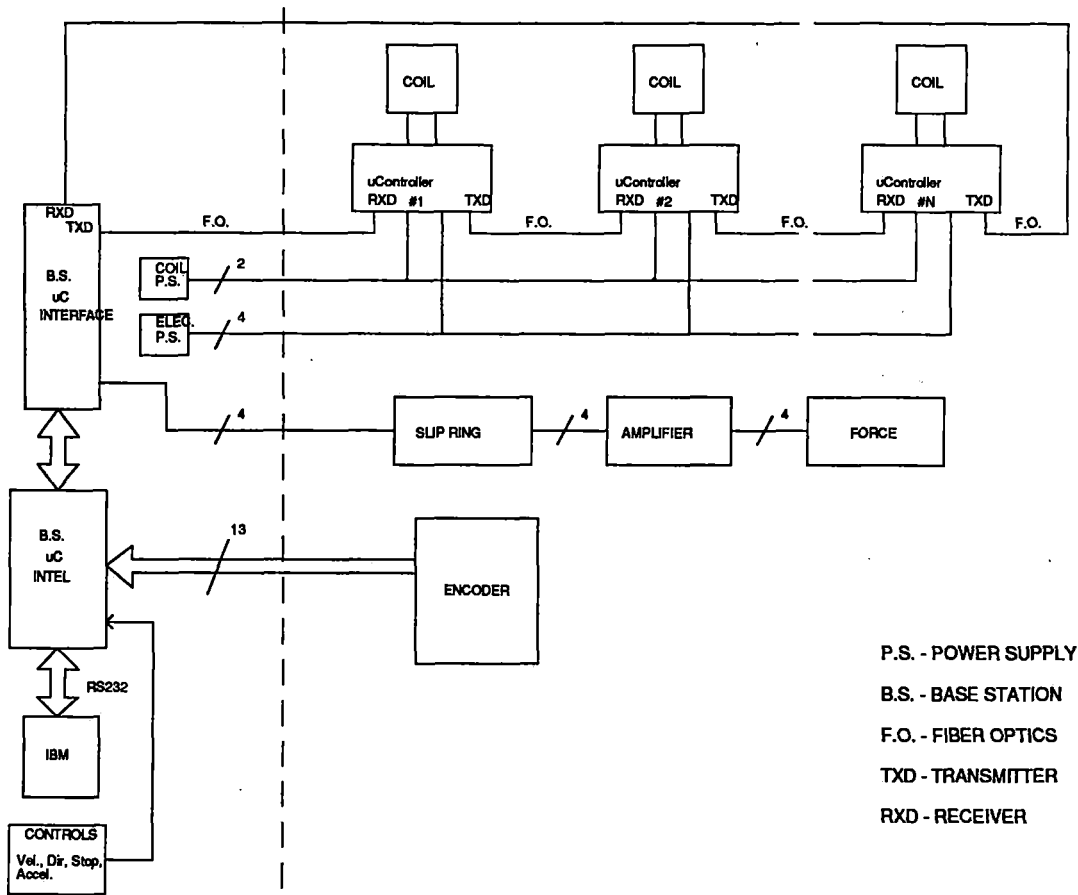


Figure 2-19. Calculated EMF for four permanent magnets



P.S. - POWER SUPPLY
 B.S. - BASE STATION
 F.O. - FIBER OPTICS
 TXD - TRANSMITTER
 RXD - RECEIVER

Figure 2-20. Controller hardware block diagram

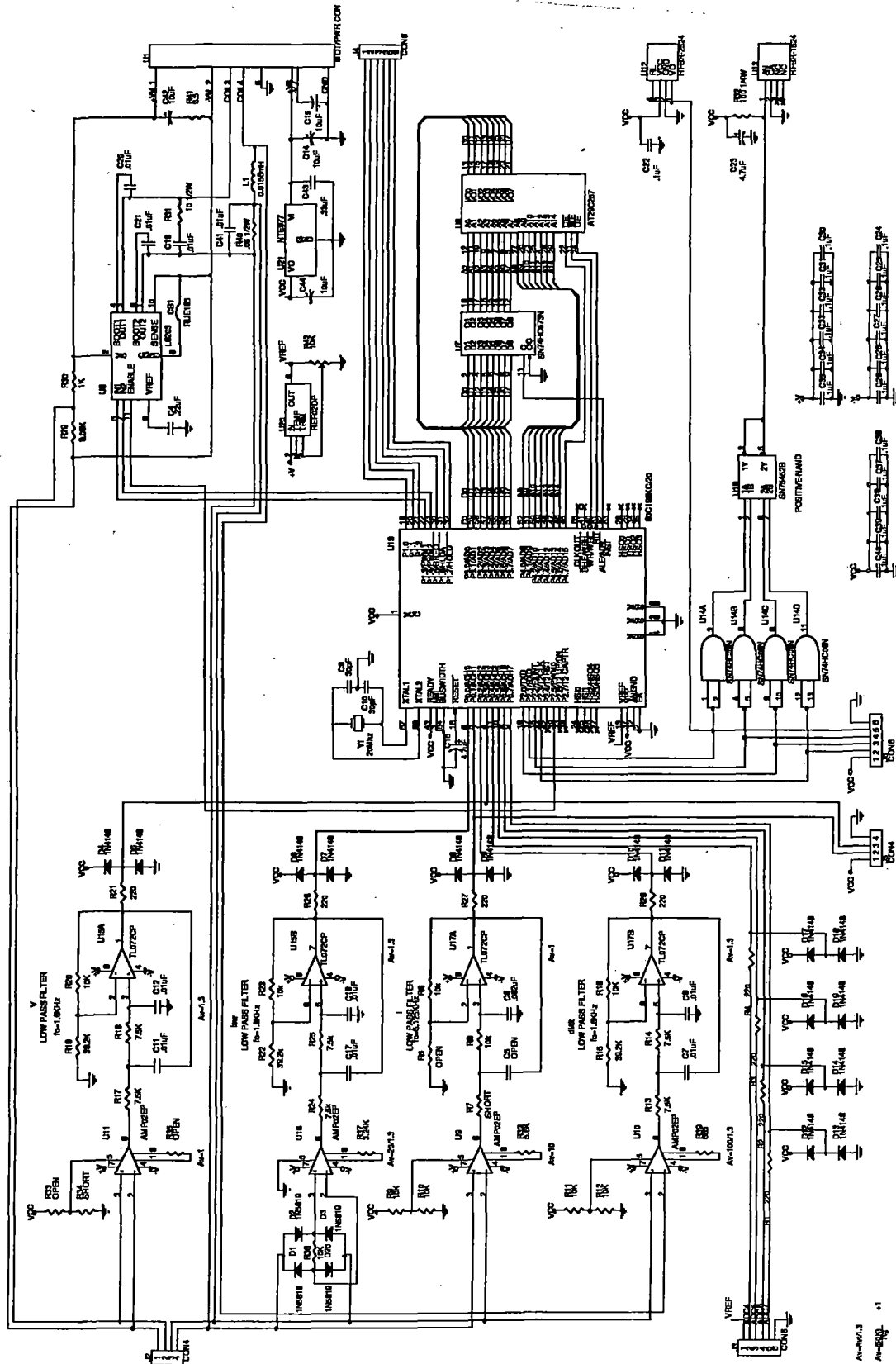


Figure 2-21. Controller board design

"Information on this page identified by asterisk (*) in the margin is proprietary to Foster-Miller, Inc."

3. FABRICATE SCALE EXPERIMENT

3.1 Component Fabrication

The fabrication of the scale experiment was begun with component fabrication including the scale model system mechanical components, coils and control components. Where possible, the performance of the subsystems was verified before assembly of the full experiment. The software for control was developed during this subtask.

3.1.1 Scale Model System Mechanical Fabrication

A rotor system with stationary coils was determined to be a more suitable approach for this demonstration model. The complete experiment assembly used is shown in Figure 3-1. The hardware was mounted on a Formica covered table with a 6 in. thick top. This table formed a rigid mount designed to be free of vibration and distortion.

The rotor was mounted on a shaft in the center of the table. The shaft was part of a DC motor located below the table which served as a load for the experiment. The motor was mounted to an aluminum plate bolted to the table top. The rotor was a composite material

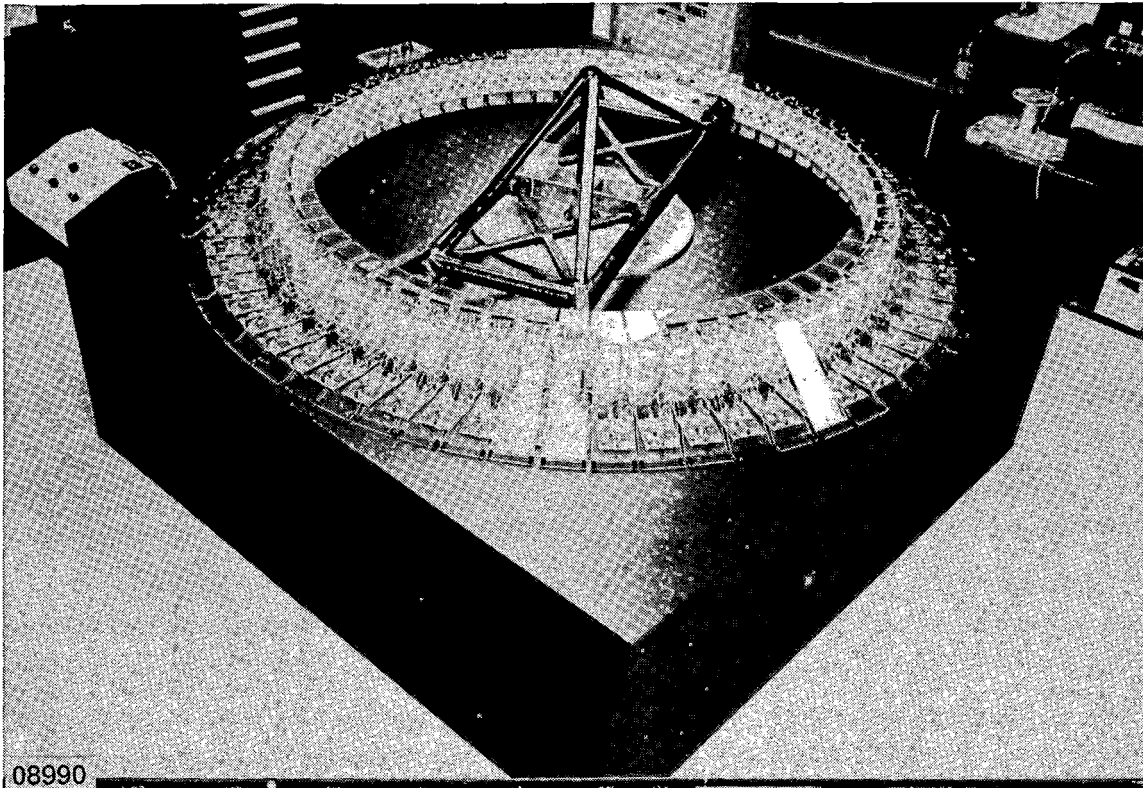


Figure 3-1. LCLSM table

(carbon/fiberglass/epoxy) structure which supported and guided the magnets on one side and the counterweight and position detection system on the other.

The coils were mounted on coil support blocks bolted to the table. There were 64 coils and support blocks. The table top was shimmed to be flat with respect to the rotor shaft to within 0.015 in. The coil supports were then positioned at a constant radius with respect to the shaft (to within 0.005 in.). The coils were then mounted to the blocks and positioned circumferentially by using shims between the edges of the coils. With this method the coils were uniformly positioned around the periphery to better than 0.010 in.

The magnet assembly (referred to as the vehicle) mounted on the rotor is shown in Figure 3-2. It consisted of composite side plates covering four of the vehicle permanent magnets (5 x 10 x 1.6 cm). Plastic nose and tail pieces have been included to reduce windage effects on the measured propulsion forces. The magnets were spaced on a 13 cm pitch. The centers of the magnets were located at a radius of 72.85 cm. The pitch of the permanent magnets at this radius was 13 cm.

The vehicle was mounted to the rotor on two arms. The arms were mounted to the vehicle and the rotor in bearings to form a four bar linkage. The arms and vehicle were restrained from swinging by a load cell on the rotor (attached to the top arm in Figure 3-2). The load cell measured the thrust on the magnets which was transmitted to the rotor. The load cell signal was amplified on the rotor in the amplifier shown in Figure 3-1 (the box near the center of the rotor assembly). Data from the load cell was transmitted through a slipring located at the top of the rotor hub.

The side of the rotor opposite of the magnets is shown in Figure 3-3. The metal disks mounted on the composite plates on the rotor were counterweights used to balance the rotor.

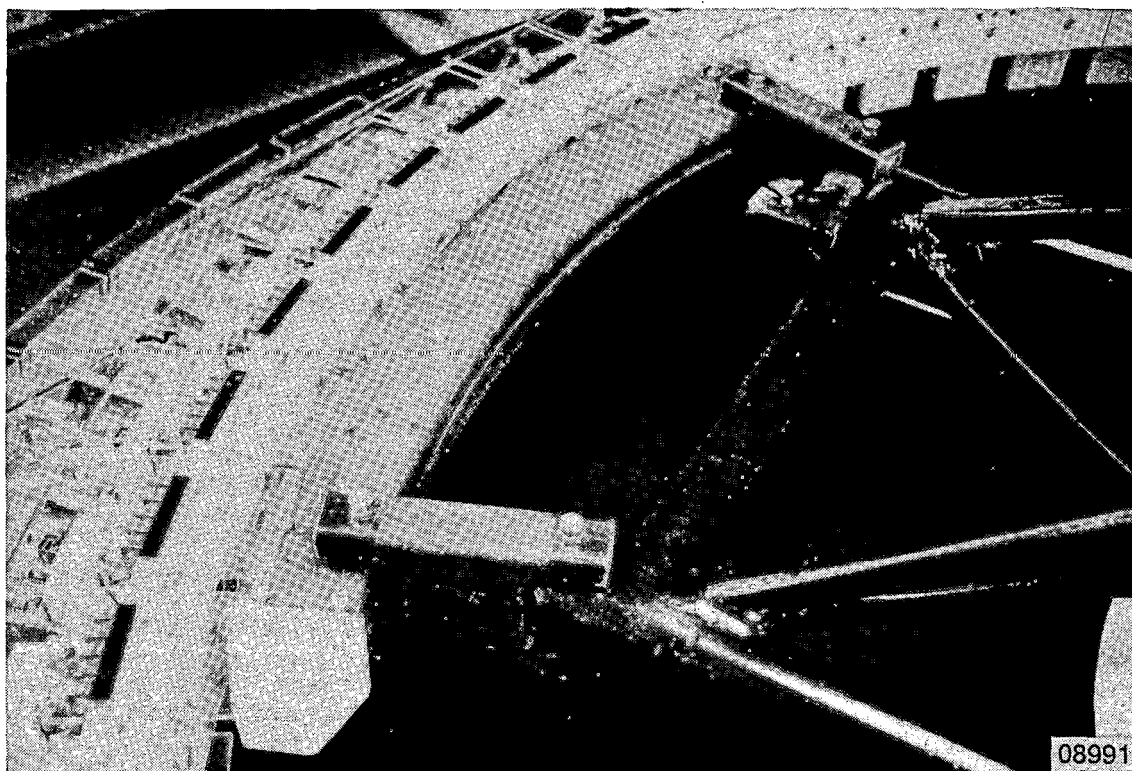


Figure 3-2. LCLSM "vehicle"

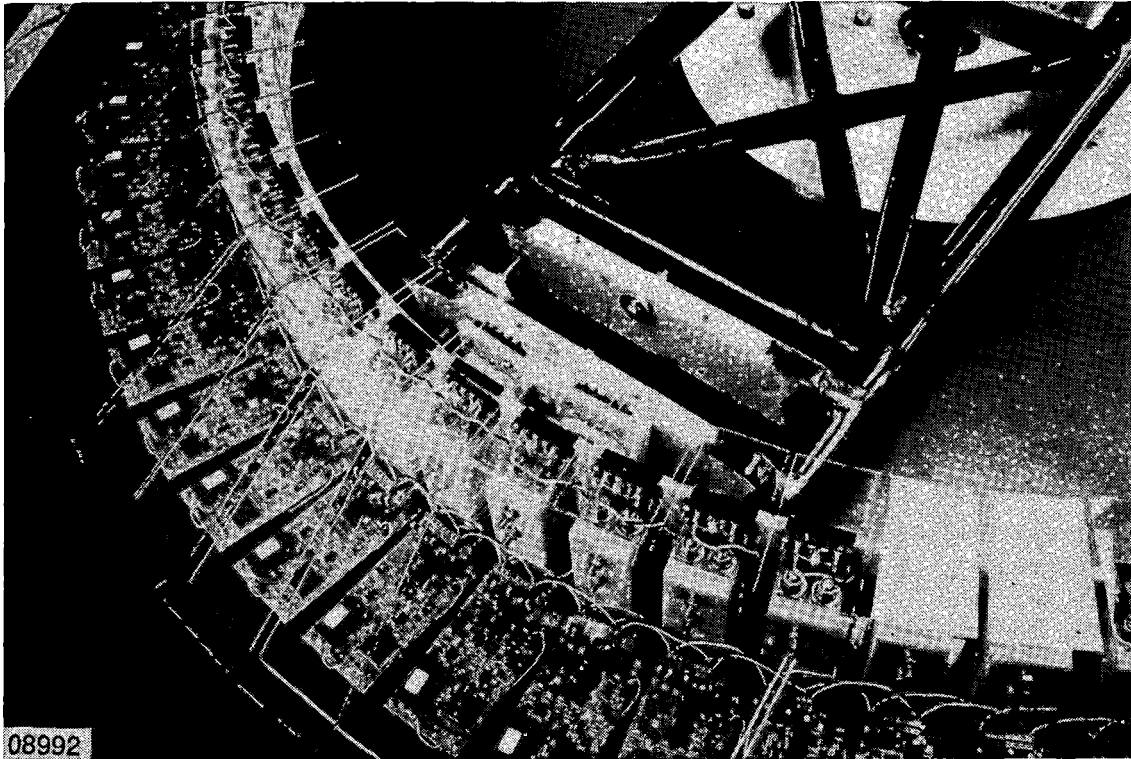


Figure 3-3. Counterweight and position detection coils

Positioning coils were mounted on the outer face of the outer light colored plates on the rotor. These two coils were shorted and tended to reduce the transient impedance of a coil positioned across the relative motion gap. Figure 3-3 also provides a good view of the coil current control boards mounted to the table.

Figure 3-4 is a view under the table showing the permanent magnet motor which was used as a controllable load. By varying the resistance across the armature, the load on the LCLSM motor was varied. For emergency stopping a direct short can be applied across the load motor. Vertical support braces (4) surrounding the load motor are also shown in Figure 3-4. These were included to stiffen the table top against vertical modes of vibration.

3.1.2 Inverter/Control Component Fabrication

Control Board/Inverter

The microcontroller, memory and inverter were mounted on a common board with the fiber optic transceivers. One of the 64 boards is shown in Figure 3-5 displayed on the corner of the LCLSM table. A fiber optic cable was connected in this figure to display the communications hardware.

Base Station

The base station control box is shown in Figure 3-6. This included manual input controls (knobs) for position, speed, and velocity limits. An emergency stop was included (switch on the upper right) which shut off power to the inverter bus and applied braking torque to the rotor.

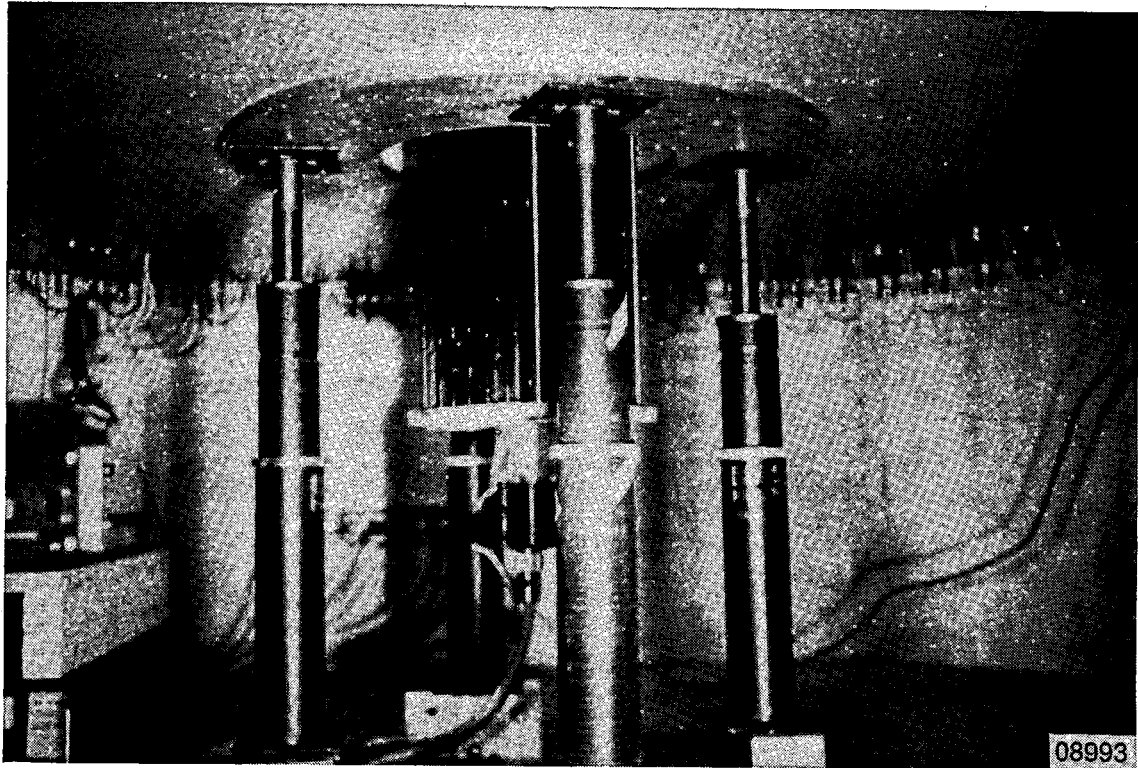


Figure 3-4. Load motor

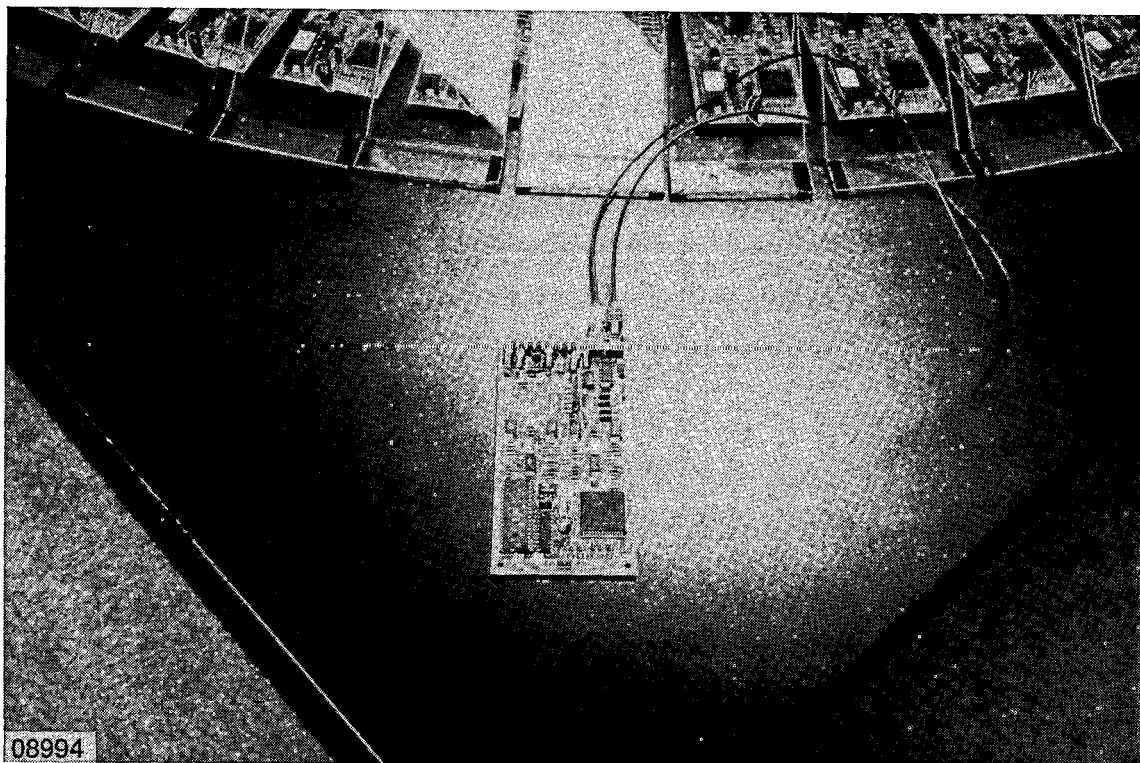


Figure 3-5. Coil control board

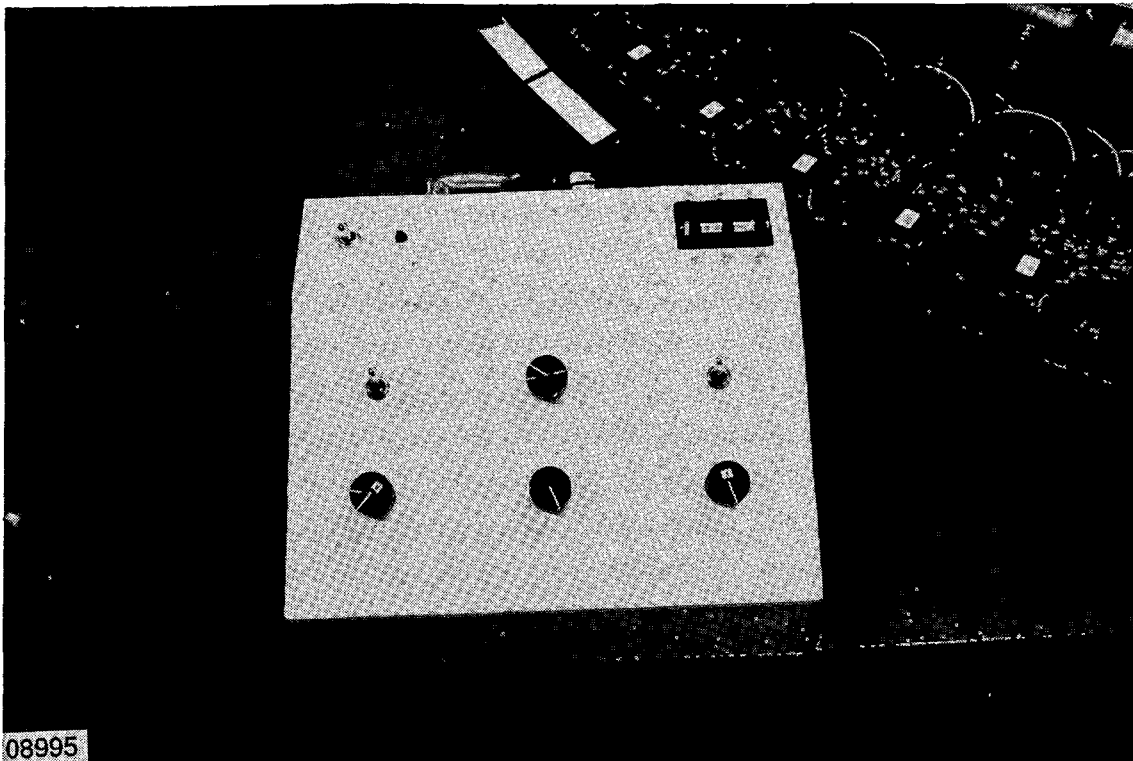


Figure 3-6. Base station control box

3.1.3 Component Tests

The back EMF wave for one of the test permanent magnets (5 by 10 by 1.6 cm) was tested on a prototype track coil. The fiber optic communications components linking the individual processors was also tested. The electrical characteristics of the coils were measured (1.43 mH and 1.23 ohms with better than 4 percent accuracy). The effect of small variations in the inductance and resistance between coils can be accommodated by the local current control. A potentially more important parameter was variation in the mutual inductance between the rotor magnets and the stator coils. The variation in mutual inductance was tested as part of the rotor tests and was found to be accommodated by local current control.

Each inverter/controller board was individually inspected and tested for proper assembly and functionality.

3.2 Assembly

Assembly of the experiment was begun with the mechanical assembly of the wheel components. After complete assembly the system was balanced. Electrical subassemblies and the final assembly were tested as each was completed.

3.2.1 Mechanical Assembly

The assembly of the table and coils was described in subsection 3.1. In summary the coils are positioned to within 0.015 in. (0.38 mm) vertically, less than 0.005 in. radially (0.13 mm) and less than 0.010 in. (0.25 mm) in the circumferential direction. These tolerances were based on the calculated variation in thrust for a given position error as presented in Figure 3-7.

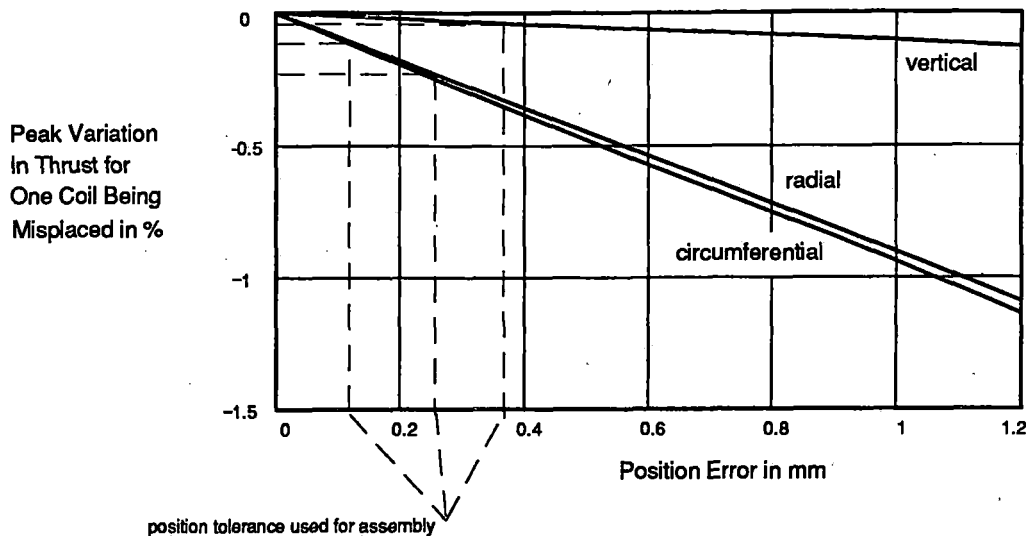


Figure 3-7. Calculated impact of assembly tolerances

This calculation was made using the Neuman equation computer routines verified in pendulum testing of a permanent magnet with one coil.

3.2.2 Balancing

The assembly was statically balanced by hanging the rotor from its center and adding weights shown in Figure 3-3.

3.3 Debugging

After assembly of the full experiment, the complete system was debugged to ensure the communications and control functions were operating.

The individual coil current control boards were used to produce up to 100 Hz sine waves in the track coils. The overall function of the system was demonstrated with some remaining anomalous behavior which developed over time in a few of the boards. These boards were replaced with spares.

Delays were experienced in communications between the base station and the local current control boards. Communication at reduced rates was used to reduce the cycle time on the local processor. The ability of the local controller to control smooth current sine waves in the track coils (a function previously demonstrated for a local control board not communicating to the base station) required a significantly faster cycle time than previously achieved. The present cycle time for the LCLSM processors was reduced by an order of magnitude from that used for control and performance design and analysis. This order of magnitude reduction had substantial adverse impact on performance of the system under certain operating conditions.

4. TEST AND EVALUATION

Section 4 describes the tests and evaluations performed with the experimental apparatus. First, basic electrical tests which verified design parameters, scaling laws, and calculated electrical characteristics of the apparatus are described. Then, static and dynamic tests of the motor system are described, followed by conclusions and recommendations relating to the system tests.

4.1 Basic Electrical Tests

4.1.1 Static Tests Measuring Variation in Electrical Parameters

The electrical characteristics of the track coils were measured. The coil inductances were 1.43 mH and the resistances averaged 1.15 ohm at 23°C. The resistance measurement was used to compare coil characteristics as shown in Figure 4-1. The coils were specified as having 120 turns. With the possible exception of coil 55, the resistances of the coils indicated consistency in the number of turns.

The coils were positioned with respect to the center of rotation and the table was shimmed to be generally flat. Table 4-1 presents the location of the 64 track coils and the four magnet set on the vehicle. The vertical locations were accurate to approximately 0.5 mm and the radial locations were accurate to approximately 0.2 mm. During testing the coils were located with respect to the 13 bit (8192 count) encoder used to measure the vehicle location.

Table 4-2 presents the electrical characteristics of the load motor used with the experiment.

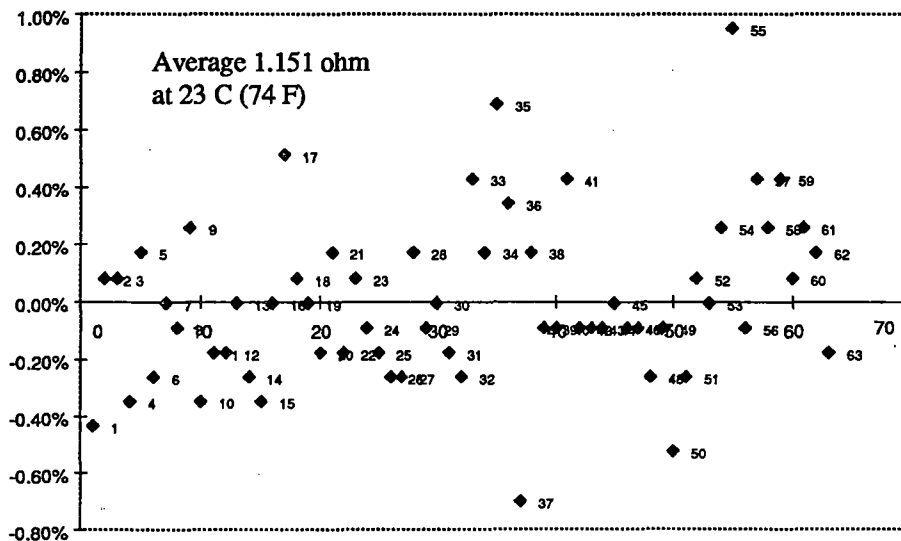


Figure 4-1. Variation in coil resistance

Table 4-1. Encoder calibration

	Rad Centers (cm)	Pitch (cm)	Count/Rev	Count/Pitch	Count per Four Magnets
Coils	75.85	7.45	8,192	128.00	
Perm. magnets	72.85	13.00	8,192	232.65	930.61

Figure 4-2 presents the measurements made on the bridge. Voltage measurements were made relative to point 5 at points 1-4. The current reading was made by measuring the voltage drop across a 0.05 ohm resistor between the bottom of the bridge and the low side of the power bus. This reading was filtered (1.6 kHz second order low pass filter) and amplified by a factor of 10 before going to the data acquisition system. This resulted in a 0.5 V/A output for the bridge current.

Table 4-2. Load motor characteristics

	Armature	Armature + Load Resistor
Load (ohm)	0.1	0.474
EMF/Hz (approximate single phase RMS value)	2.8	

Because the current into the bottom of the bridge is always positive (except during regenerative braking) this measurement reads the rectified current which goes through the track coil.

Permanent magnets were used in this experiment as a simpler alternative to excited magnets on the rotor. These magnets were a model of the superconducting coils in the full-scale system. The neodymium-iron-boron magnets used in the experiment were particularly strong and provided a large number of equivalent ampere turns of excitation. The four permanent magnets were characterized as equivalent coils with an effective number of ampere-turns which were inductively coupled to each of the track coils with the coupling being a function of position. These electrical characteristics of the permanent magnets are summarized in Table 4-3. Figure 4-3 shows the measured and calculated back EMF in one of the track coils (number 32, unexcited) with two sets of timing pulses from the encoder. One of the pulses occurred twice per rotor rotation and the other occurred 128 times per rotation.

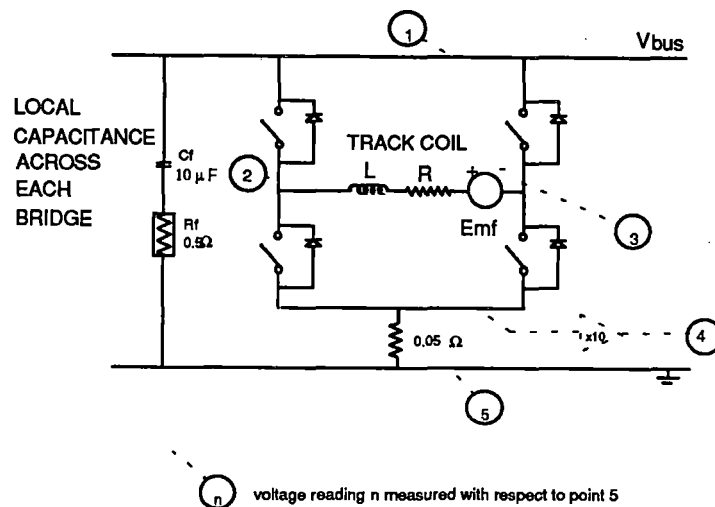


Figure 4-2. Bridge measurements

Table 4-3. Permanent magnet model

	Length (cm)	Height (cm)	Thickness (cm)	Pitch at Mid-Plane (cm)	Effective Ampere-Turns
Permanent magnet	10	5	1.6	13	16,800

The rotor frequency can be calculated as the frequency of the rapid timing pulse divided by 128. For the case shown in Figure 4-3 the rotor frequency is 2.62 Hz. The peak back EMF on the coil was 16.8V for this velocity. On the basis of the magnet speed at the outer radius of the rotor the back EMF characteristic of the linear motor is 14.01 V/(m/sec).

4.2 Dynamic Tests

The important features of the LCLSM concept were demonstrated by the model system. Measurements match predicted results and the distributed control and power processing were demonstrated in theory and practice. Although the demonstration was successful and the LCLSM concept was proven feasible, there were some performance limitations in this particular experimental implementation that prevented the most useful results from being obtained in all test scenarios. The primary limitation was that caused by the effective update time for the inverter controllers. The duty cycle for the PWM was updated on the order of every 1 msec. As was discussed in earlier sections of the report, all modeling and simulation were performed based on an update rate of 100 μ sec, on the order of ten times faster than the update rate actually achieved. This had several adverse effects on the system performance. The primary adverse effects were: the PWM duty cycle setting update rate was inadequate to produce as smooth a waveform as desired, and the control system suffered some instability due to the

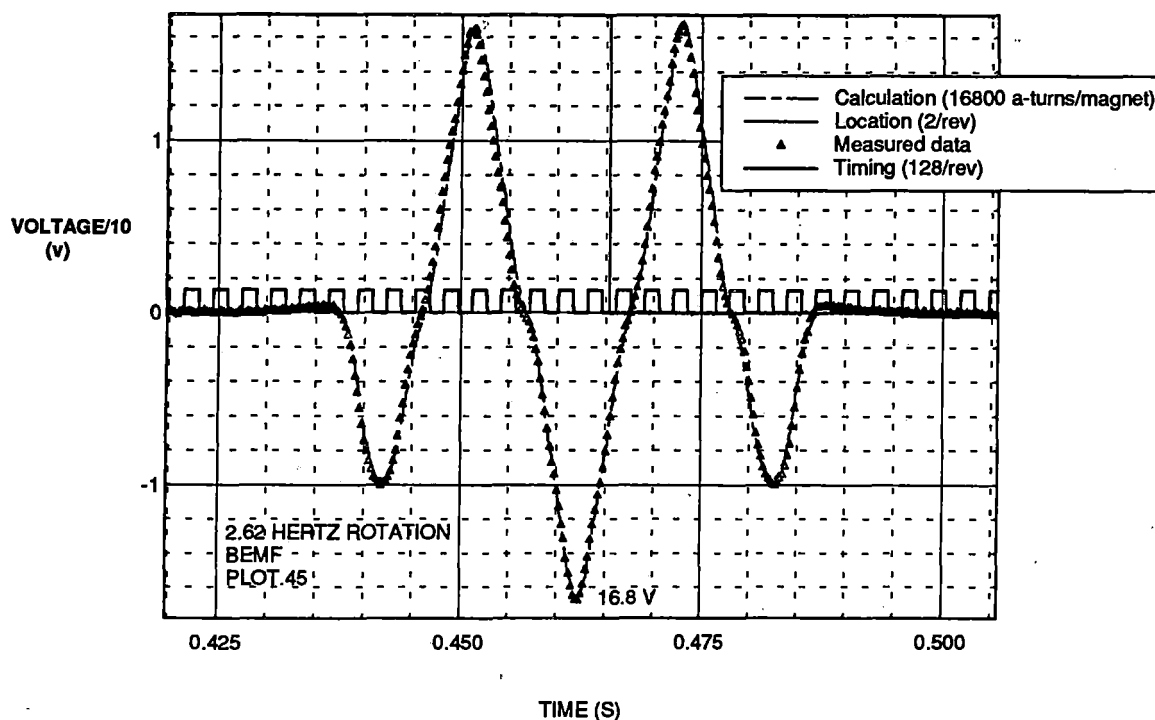


Figure 4-3. Field characteristics/back EMF

delay both in the PWM update time and feedback delay due to communications protocol implementation which increased the loop time. A (manually adjustable) phase shifting system between the encoder position reading and the control system was implemented to partially account for the delays, but this was not an ideal solution since it resulted in inaccuracies in the current phasing and produced thrust oscillations and potential resonances in the system. Under high power factor operation the rotor essentially operated at the top of the magnetic wavefront peaks. The control system corrected the phase and current to keep the peaks lined up. The increased PWM update time meant that the oscillation around the peak, termed cogging, was larger than the design configuration. Because of the effects of the increased PWM update delay times of the present implementation and the higher loop time of the control software, current waveforms and thrust did not achieve the extreme smoothness possible with the LCLSM configuration.

These limitations of the experiment implementation can be overcome with further refinement of the system. Modification of the coding for the processors is a significant means of improvement. Most of the coding is in the C language. Code implementation in assembly language along with streamlining of the control procedures would result in a substantial improvement in loop speed. Then, tuning of the control system parameters to match the loop speed achieved with the new coding would improve performance and system stability. Tuning the bus filter parameters around the characteristics of the control system with the new loop time further aids in the ability to provide smooth thrust. Thus there are both implementation-specific and general approaches to improving system performance.

Any of the limitations that were observed in this experiment were not limitations inherent to the LCLSM concept but were simply limitations relating to the specific experimental implementation and practical issues of funding and scope of the program.

The test configuration presented in Figure 4-2 was used with a data acquisition system to obtain the operating characteristics of the system as a function of operating point. A typical run is presented in Figure 4-4. The current measurement was rectified as a result of the location of the current measurement resistor at the bottom of the bridge (Figure 4-2). The bus voltage was seen to have substantial harmonic content when the local bridge was excited. The bus harmonic content quickly died down as the excited region moved away from the measurement point.

The force measurement presented in Figure 4-4 is based on a load cell on the four bar linkage supporting the vehicle. The force measurement system may not be operating optimally due to adjustments of the linkage and possible stick-slip phenomenon. Calibration testing showed that at very low rotational speeds the thrust can be calculated as the following function of the sensor reading (r):

$$\text{Thrust} = (r - 3.4 \cdot v) \cdot 77 \cdot \frac{n}{v}$$

It was found that the offset shifts significantly at higher speeds; additional adjustment and calibration of the force measuring system could improve the accuracy of the thrust measurements.

The voltage from ground to each terminal (side) of the coil is also plotted in Figure 4-4. Since the coil was driven by Pulse Width Modulation (PWM), the voltage measurement was essentially rail to rail pulses when the measured terminal was driven by the positive bus. The sampling rate of 20 kHz was well below the Nyquist frequency (80 kHz) for the 40 kHz PWM frequency, so the data were aliased (peaks may not be sampled, etc.), but this was not a critical measurement in terms of the details of the PWM pulses. The current and thrust waveforms

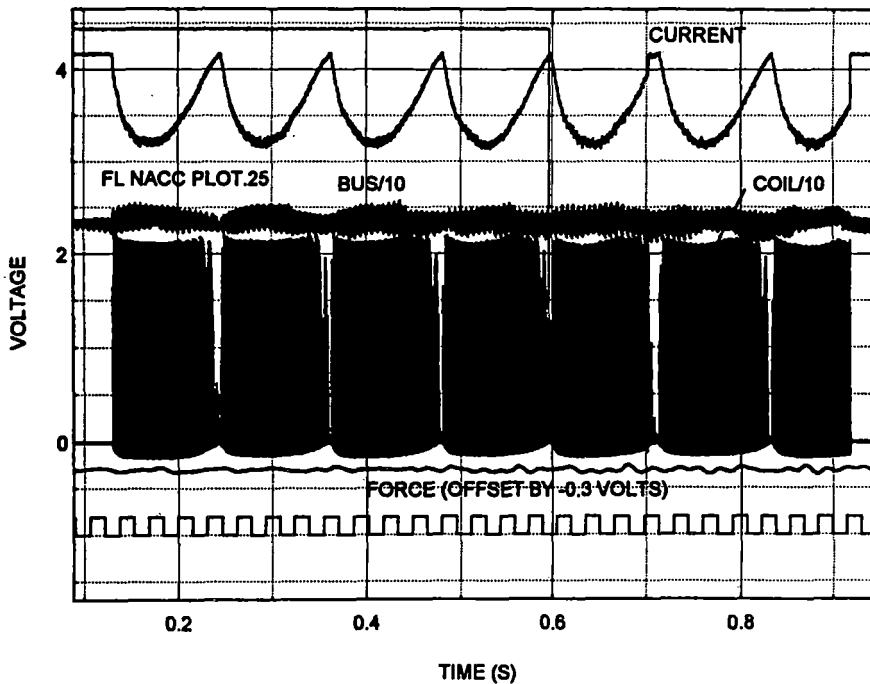


Figure 4-4. Typical test run

were adequately sampled because they were band limited to much less than 5 kHz. The pulses stopped at the zero crossing point in the current waveform (the rectified sine wave near the top of the figure). This was because the back EMF and the desired current were near zero at this point so the duty cycle was very low. This figure shows the voltages measured at both terminals of the coil. Each pulse block was the voltage measured (relative to ground) at the opposite terminal of the coil from the adjacent pulse block. Because both voltages are shown on the same graph, the voltage on the low (ground) side of the coil was obscured by the powered side voltage, so only the positive side of the coil is visible. As expected the inverter output was symmetric as shown by the fact that adjacent pulse packets are similar.

One coil voltage measurement was deleted from Figure 4-5 so that the voltage on the other side of the coil could be observed. For a normal bridge configuration, the voltage would be zero when the other terminal of the coil is driven, but, in this configuration, the current sense resistor between the bridge and ground produced a voltage in proportion to the current. This was the basis of the current waveform measurement and was the same for this part of the cycle except for the conversion factors, gains, and filters on the current sense measurement instrumentation.

A portion of Figure 4-4 has been expanded in Figure 4-6 (the exact part can be determined from the time scale). The bus harmonic (peak to peak) was approximately 15 percent of the bus voltage for the case studied. The current harmonic through the coil was approximately 0.2A peak to peak which was consistent with the calculations based on the coil inductance and PWM frequency.

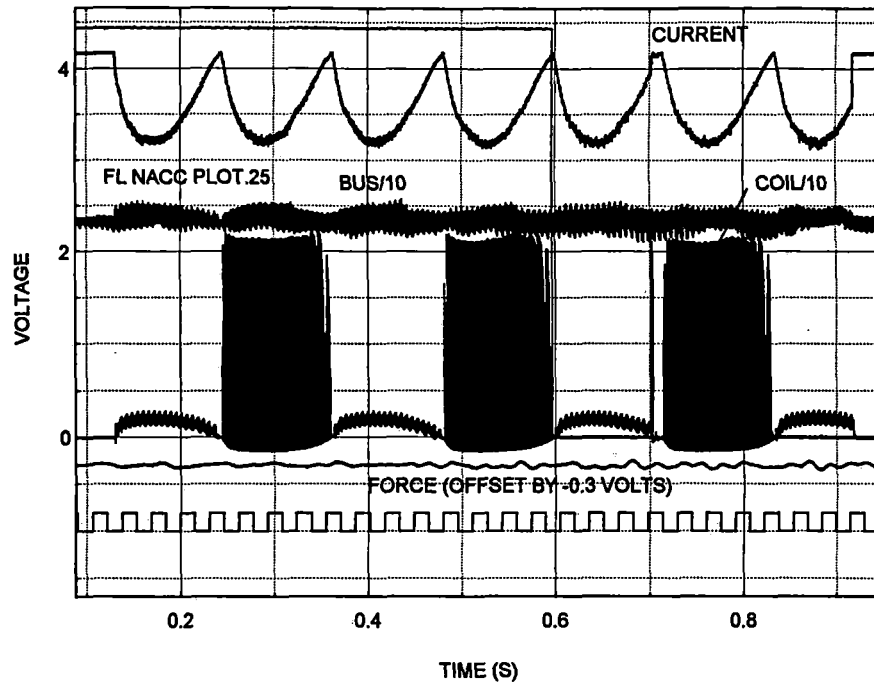


Figure 4-5. Coil voltage on one side only

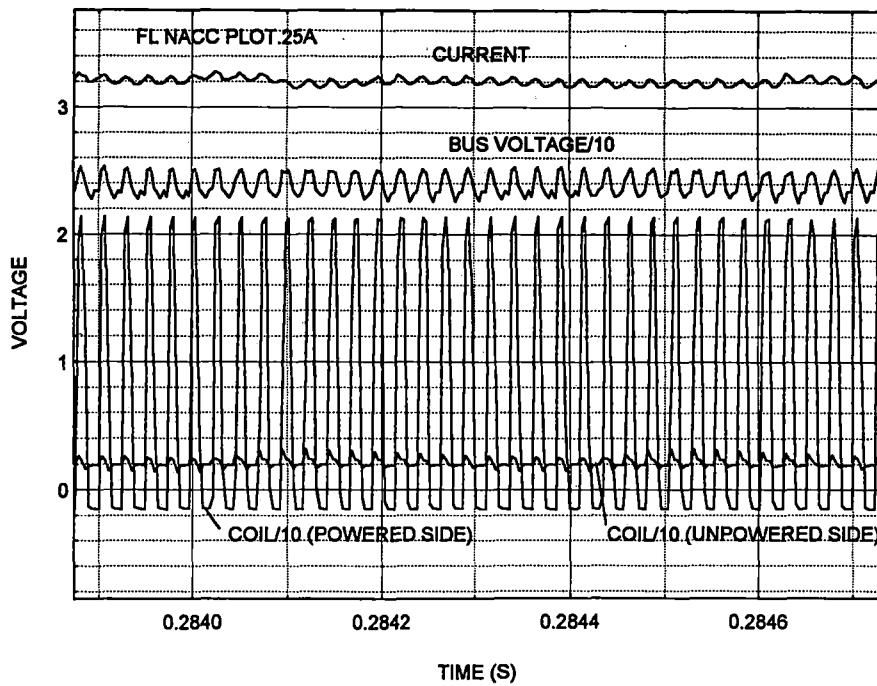


Figure 4-6. PWM harmonics

4.2.1 No Load Cases

No Load, No Acceleration Cases

A series of tests were conducted with the load (drag) motor operated open circuit. In this mode of operation the primary sources of drag were aerodynamic and bearing losses. These cases are referred to as "no-load." The data are presented in Figures 4-7 through 4-10. As can be seen, there were significant thrust variations in these cases. In general the no-load cases had significant thrust variations due to update rate limitations. These limitations were specific to this experimental setup. For example, in Figure 4-7 the thrust oscillations shown were a significant fraction of the rated thrust. The current waveforms were poorly formed. This was in part due to duty cycle update rate limitations previously described. Another factor was the low current draw which increased the magnitude of current waveform errors due to cycle time constraints relative to the actual delivered current. The large ratio of current error to desired current increased the instability of the control system and resulted in reduced accuracy of the current wave form.

No Load, Acceleration Cases

In Figures 4-11 and 4-12, cases are presented where the load motor was operated open circuit and the rotor was accelerated. The current waveforms were significantly better than for the no-load, no acceleration cases. This was due in part to the lower rotor speed and hence current waveform frequency for the acceleration cases studied (which reduced relative cycle time delay) and in part to the fact that acceleration called for a high current to produce high thrust. The high current reduced the relative magnitude of the current error and resulted in more stable operation of the control system. The current waveform produced in the

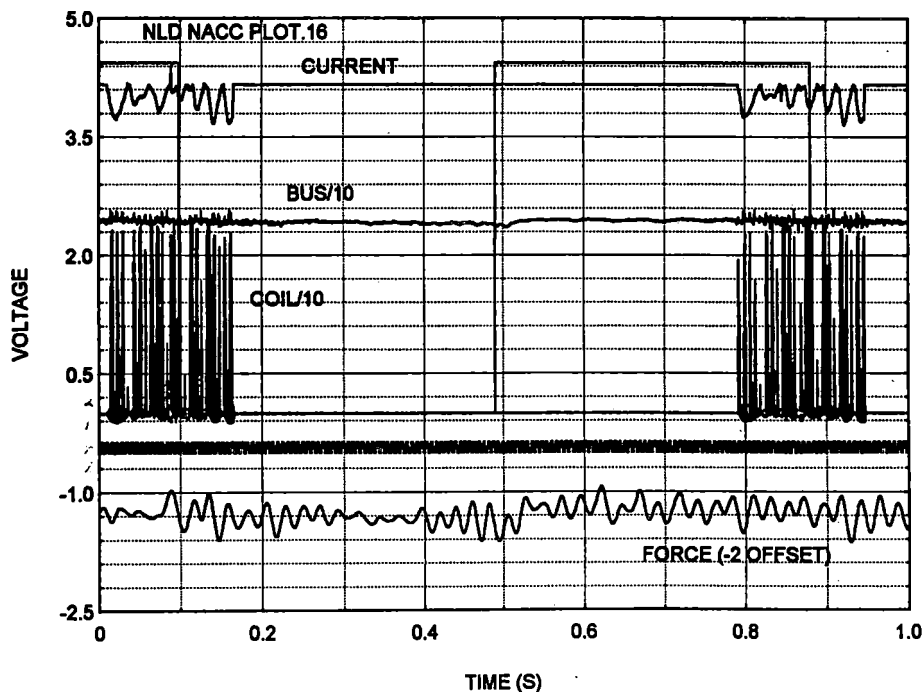


Figure 4-7. No-load, no-acceleration, case 16 (1.28 Hz, 5.87 m/sec)

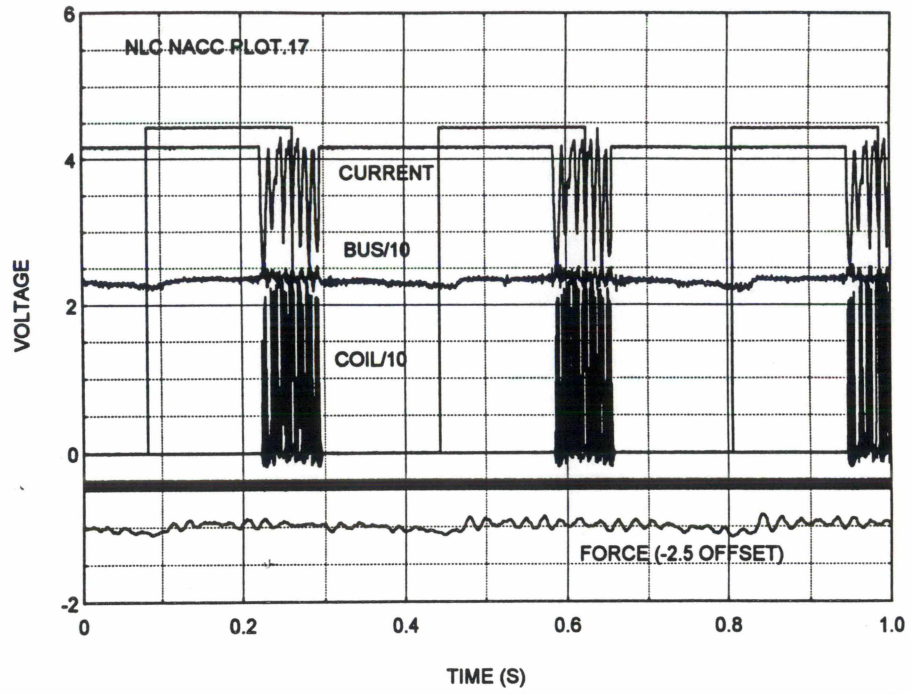


Figure 4-8. No-load, no-acceleration, case 17 (2.78 Hz, 12.72 m/sec)

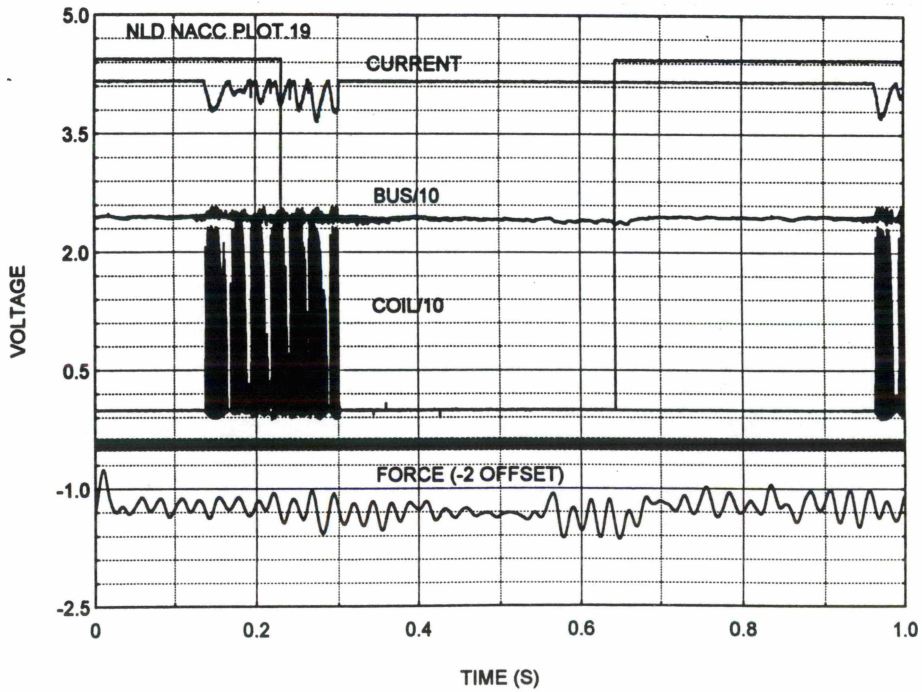


Figure 4-9. No-load, no-acceleration, case 19 (1.25 Hz, 5.72 m/sec)

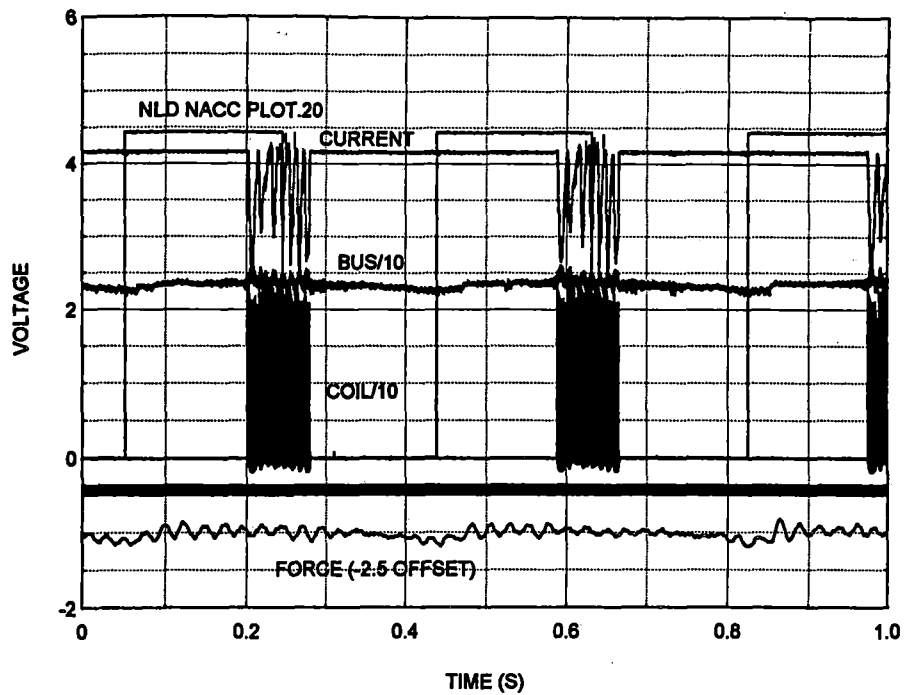


Figure 4-10. No-load, no-acceleration, case 20 (2.56 Hz, 11.73 m/sec)

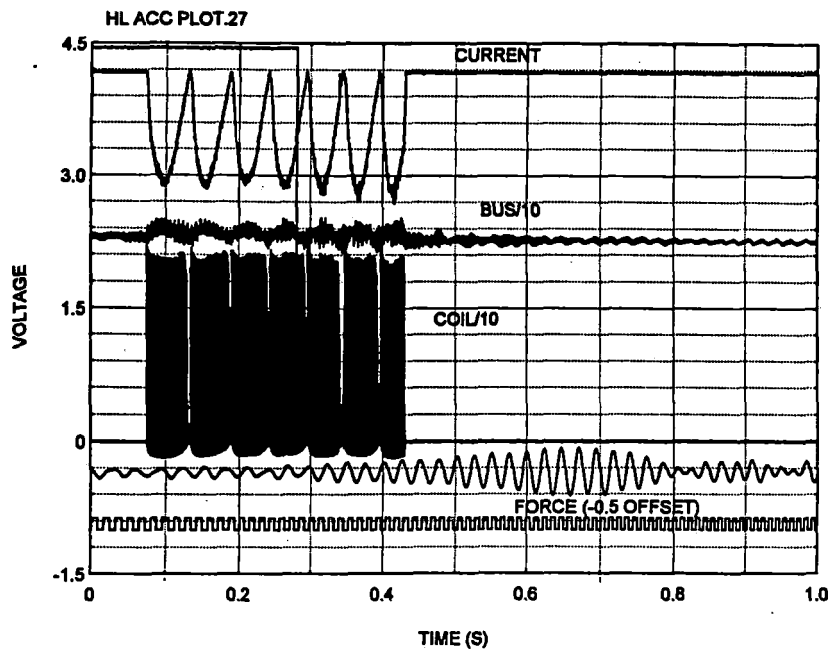


Figure 4-11. No-load, acceleration, case 27 (0.47 Hz, 2.15 m/sec, 0.3 Hz/sec, 1.39 m/sec²)

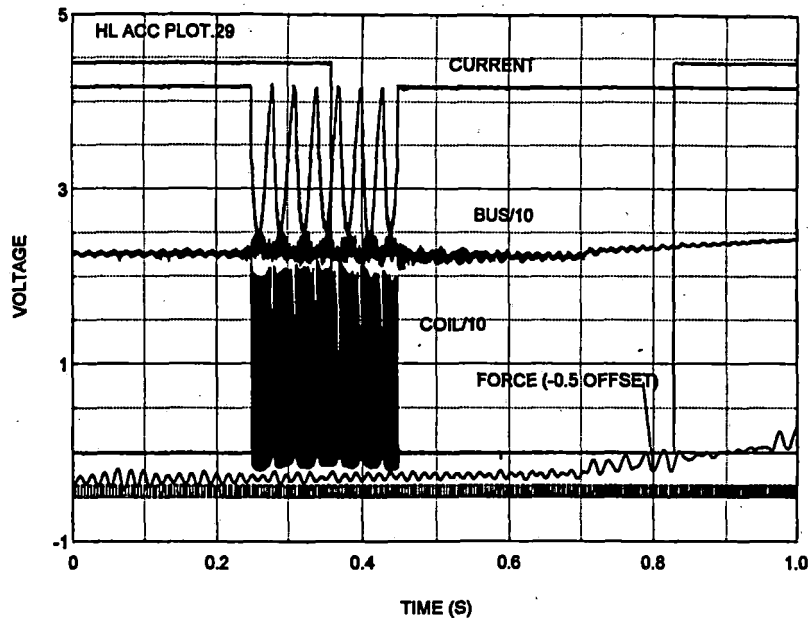


Figure 4-12. No-Load, acceleration, case 29 (0.82 Hz, 3.75 m/sec, 0.39 Hz/sec, 1.79 m/sec²)

acceleration tests was more typical of what would have been produced at lower current levels if the loop time was reduced.

No Load, Deceleration Cases

Figures 4-13 through 4-15 present deceleration cases with the velocities and rates of change of velocities listed with each figure. In these tests, deceleration was achieved by the standard motor control algorithm acting on the command to reduce current (thrust) so that the velocity matched the set point velocity. For no load conditions and a high deceleration rate this means that the commanded current was negative relative to what would have been commanded for steady operation or acceleration. This was not a regenerative deceleration. Under these conditions the back EMF was aiding the bus voltage because the current was being driven in the same direction as the back EMF under deceleration rather than bucking it as in normal operation.

Figure 4-13 presents a deceleration from a slow speed to a stopped condition as can be seen by the increasing period of encoder pulse and the current waveform which tracked the magnet position. Because the waveform frequency was low, the effect of the loop PWM update time delay was reduced. Figures 4-14 and 4-15 show a deceleration of sufficient rate to result in an oscillation in the control circuit for the coil current. This can be seen in the middle of the current waveforms in the figures. This instability occurred near the peak of the current waveform. This instability was not observed in the acceleration data shown in the previous subsection.

Acceleration and deceleration differed in that the back EMF was aiding the current flow in the deceleration control mode used in the tests. This effectively increased the "gain" of the

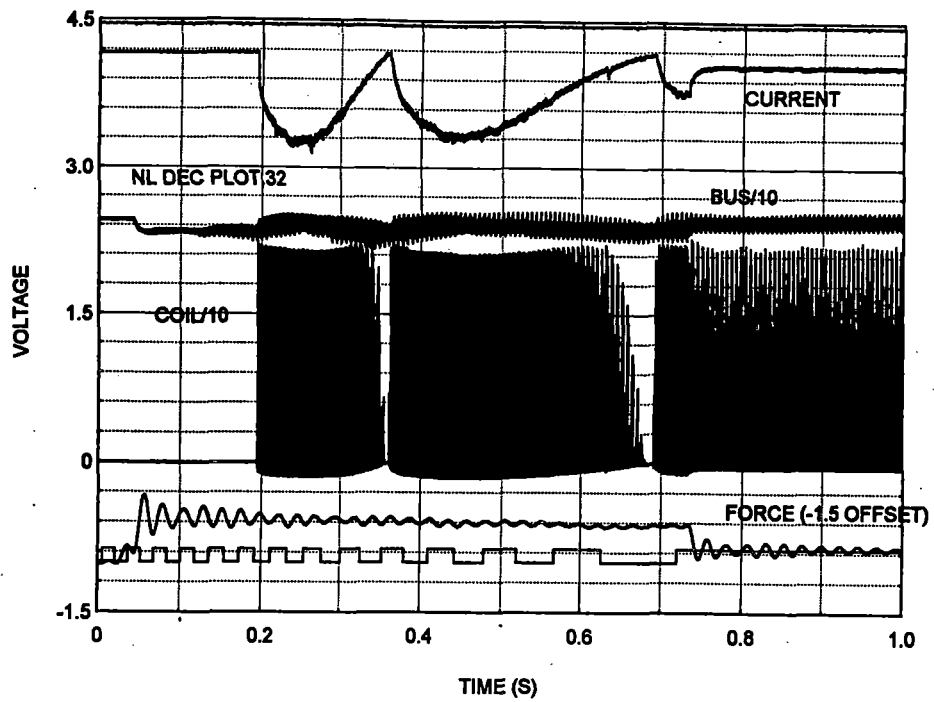


Figure 4-13. No-load, deceleration, case 32 (0.12 Hz, 0.536 m/sec, 0.39 Hz/sec, 1.79 m/sec²)

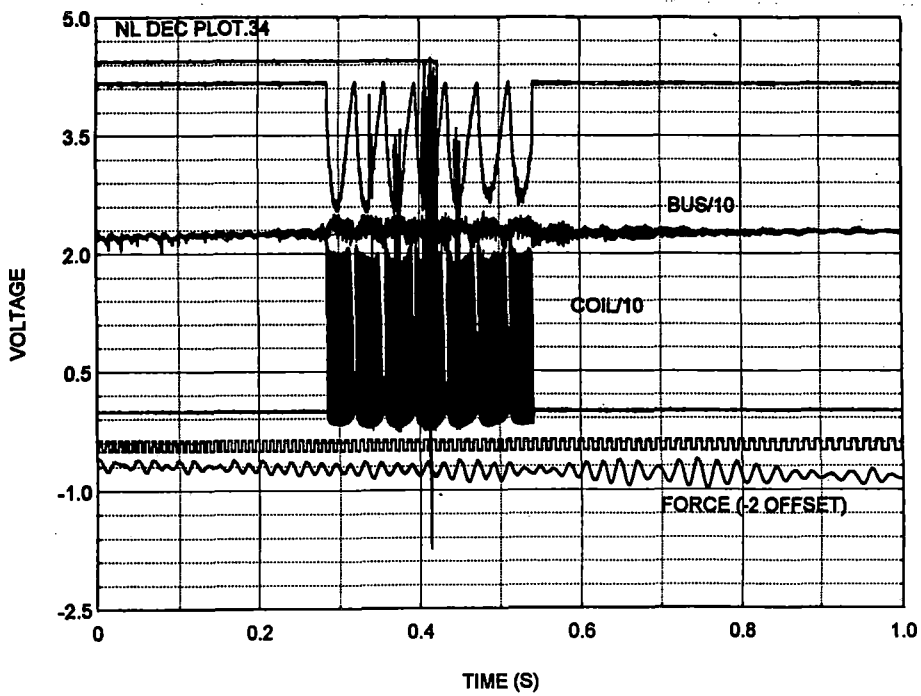


Figure 4-14. No-load, deceleration, case 34 (0.23 Hz, 1.07 m/sec, 0.52 Hz/sec, 2.38 m/sec²)

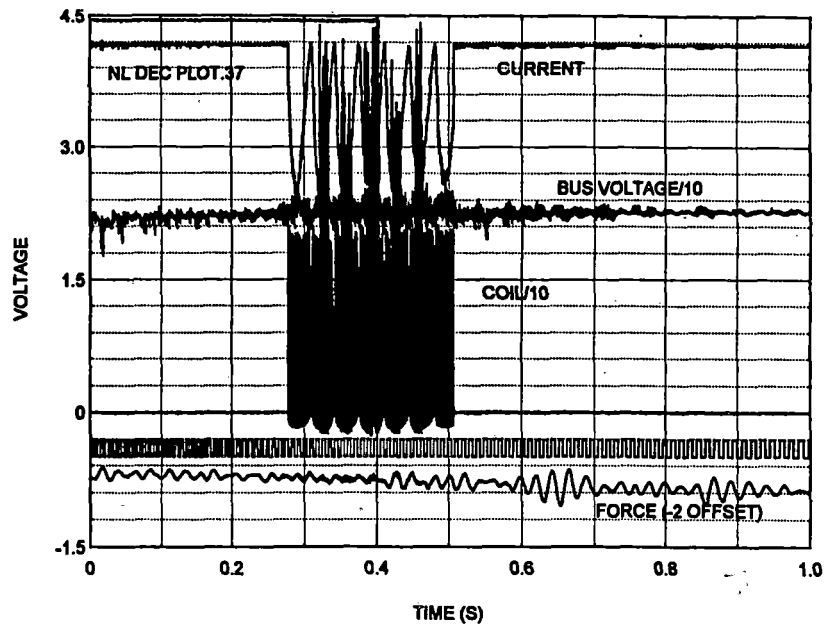


Figure 4-15. No-load, deceleration, case 37 (0.22 Hz, 0.98 m/sec, 0.48 Hz/sec, 2.2 m/sec²)

current supply which can result in instability. This instability was not apparent at low speed because the back EMF was proportional to speed. At low speeds, shown in Figure 4-13, the back EMF was very low and the loop delay time was a smaller fraction of the wave period. Both these factors contributed to stability at low speed and instability at high speed for this type of deceleration control (current driven with bus voltage and EMF adding). Regenerative deceleration utilizes an entirely different mode of operation in which the back EMF and coil inductance are utilized to produce a boost supply that drives current against the bus voltage and puts power back into the bus. Regenerative braking is within the capability of the system but has not been implemented in the control software.

4.2.2 Partial Load Cases

The partially loaded case, with the load (drag) motor as described in Table 4-2, utilized the drag motor armature connected in series with a load resistor to provide a drag load proportional to velocity. This was called the partial load case because a still greater load was achieved by shorting the drag motor at the motor terminals to achieve minimum resistance and thus maximum drag torque in the load motor. The high load cases are presented in the subsection that follows this one. Data presented in this subsection were taken under conditions of constant velocity, acceleration, and deceleration with 0.375 ohm resistors (wires) connected across the drag motor terminals to produce a drag force proportional to the rotor velocity in addition to the aerodynamic and bearing loads already present in the system.

Partial Load, No-Acceleration Cases

Figure 4-16 shows a low speed condition. The current waveform, force, and PWM output fluctuated in a manner that indicated a low frequency speed oscillation in the system. At very low speeds this velocity variation was observed visually. This low speed oscillation is typical of velocity controlled motors. At low speed, a position control scheme is more appropriate than the velocity control used for the outer loop vehicle thrust control (which is controlled at the "base station").

Figures 4-17 and 4-18 show data taken at higher speed. The waveforms were relatively steady since the load torque required significant current and the velocity control mode worked well at these speeds. The force measurement in these figures is interesting since it shows a high frequency component of oscillation on the order of 100 Hz.

Partial Load, Acceleration Cases

The partial load acceleration cases are shown in Figures 4-19 through 4-21. As was typical for acceleration where the speed was moderate and the current demand was high, the waveforms and stability were good.

Partial Load, Deceleration Cases

Figures 4-22 through 4-25 show deceleration data for the moderate load. Figures 4-22 through 4-24 and are particularly notable. Not only do they show the control instability that occurred, but the bridge control errors that occurred during this instability produced some spikes above the baseline current reading. These positive spikes represented regenerative

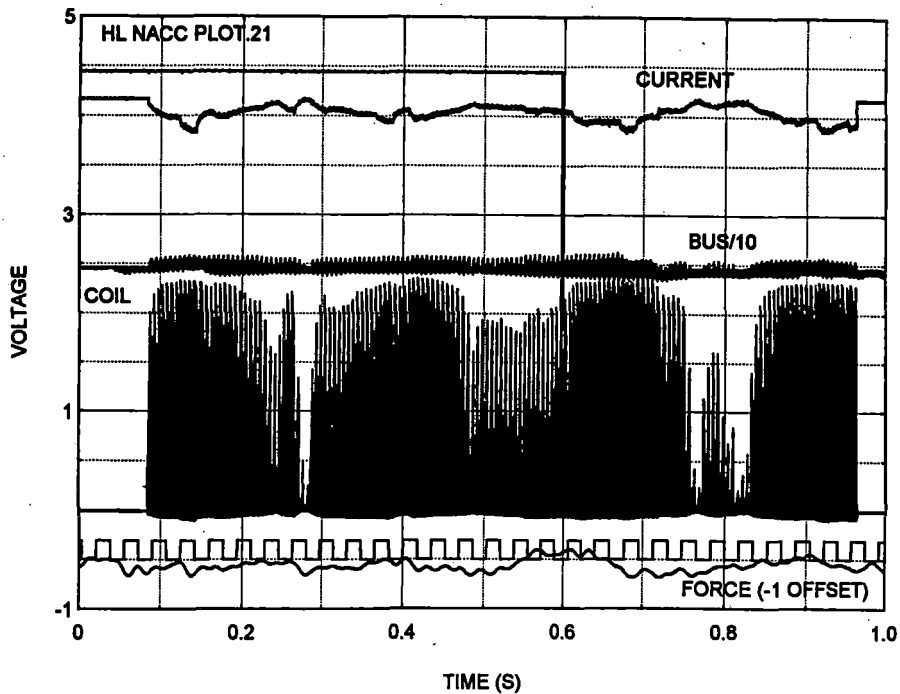


Figure 4-16. Partial-load, no acceleration, case 21 (0.21 Hz, 0.95 m/sec)

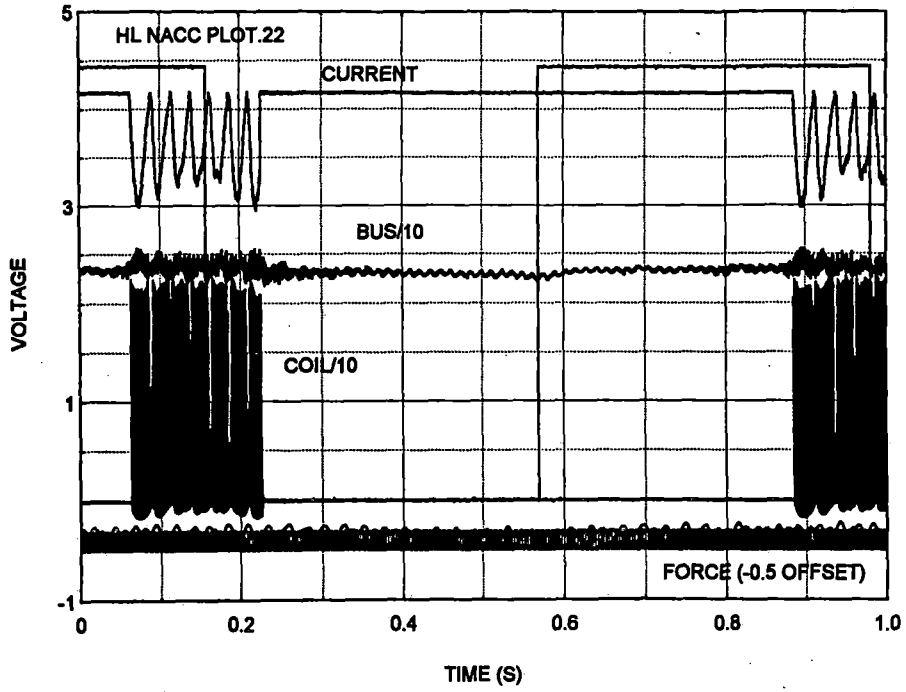


Figure 4-17. Partial-load, no-acceleration, case 22 (1.22 Hz, 5.58 m/sec)

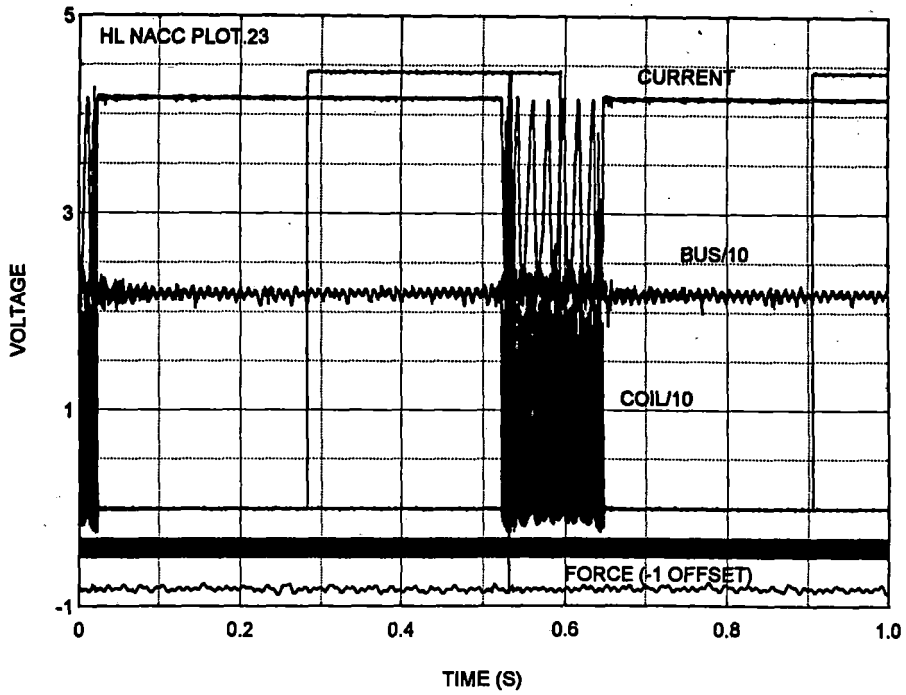


Figure 4-18. Partial-load, no acceleration, case 23 (1.59 Hz, 7.3 m/sec)

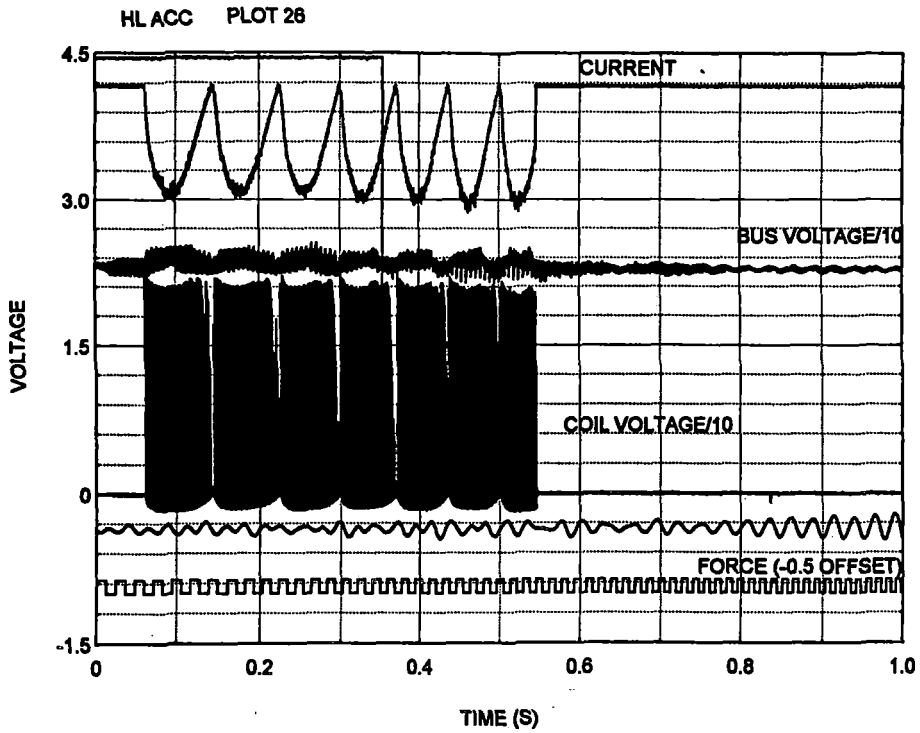


Figure 4-19. Partial-load, acceleration, case 26 (0.39 Hz, 1.78 m/sec, 0.35 Hz/sec, 1.56 m/sec²)

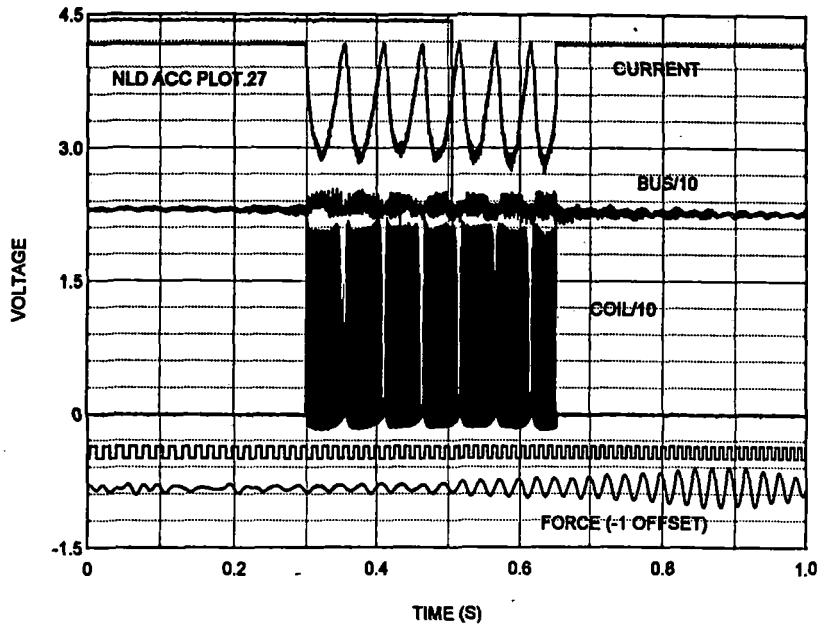


Figure 4-20. Partial-load, acceleration, case 27 (0.5 Hz, 2.3 m/sec, 0.35 Hz/sec, 1.56 m/sec²)

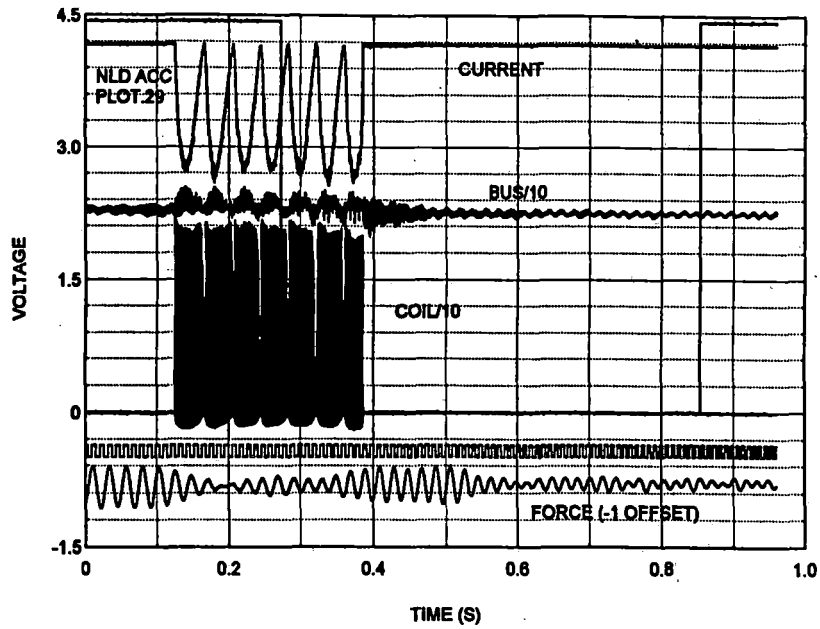


Figure 4-21. Partial-load, acceleration, case 29 (0.94 Hz, 4.3 m/sec, 0.26 Hz/sec, 1.2 m/sec²)

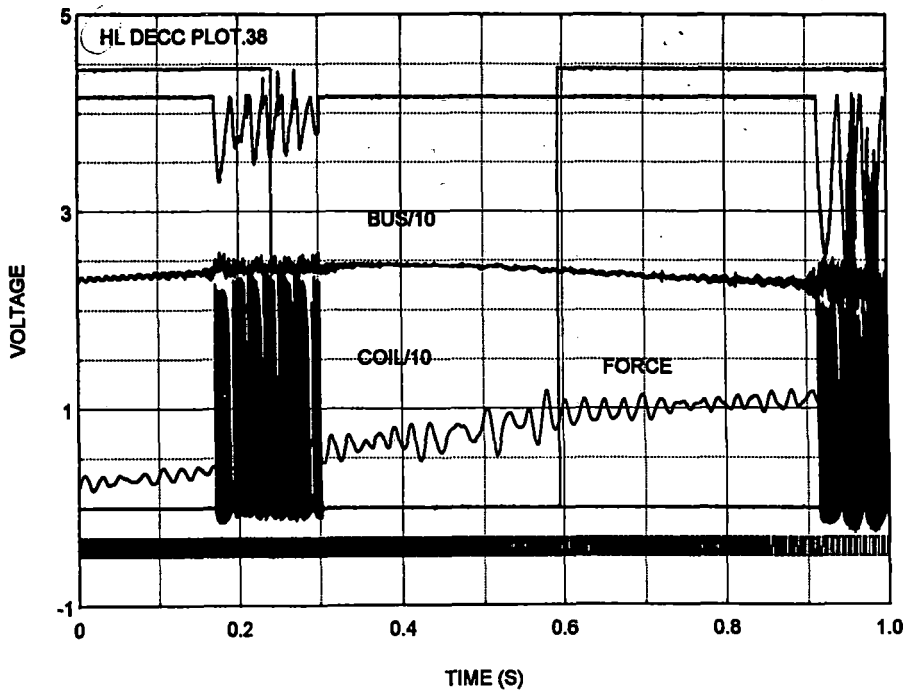


Figure 4-22. Partial-load, deceleration, case 38 (0.94 Hz, 4.3 m/sec, 0.78 Hz/sec, 3.6 m/sec²)

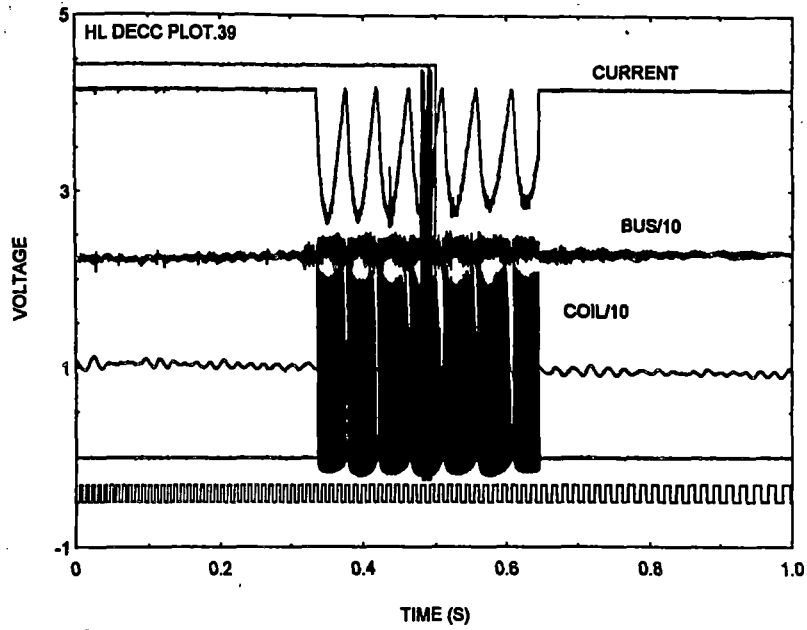


Figure 4-23. Partial-load, deceleration, case 39 (0.625 Hz, 2.86 m/sec, 0.52 Hz/sec, 2.38 m/sec²)

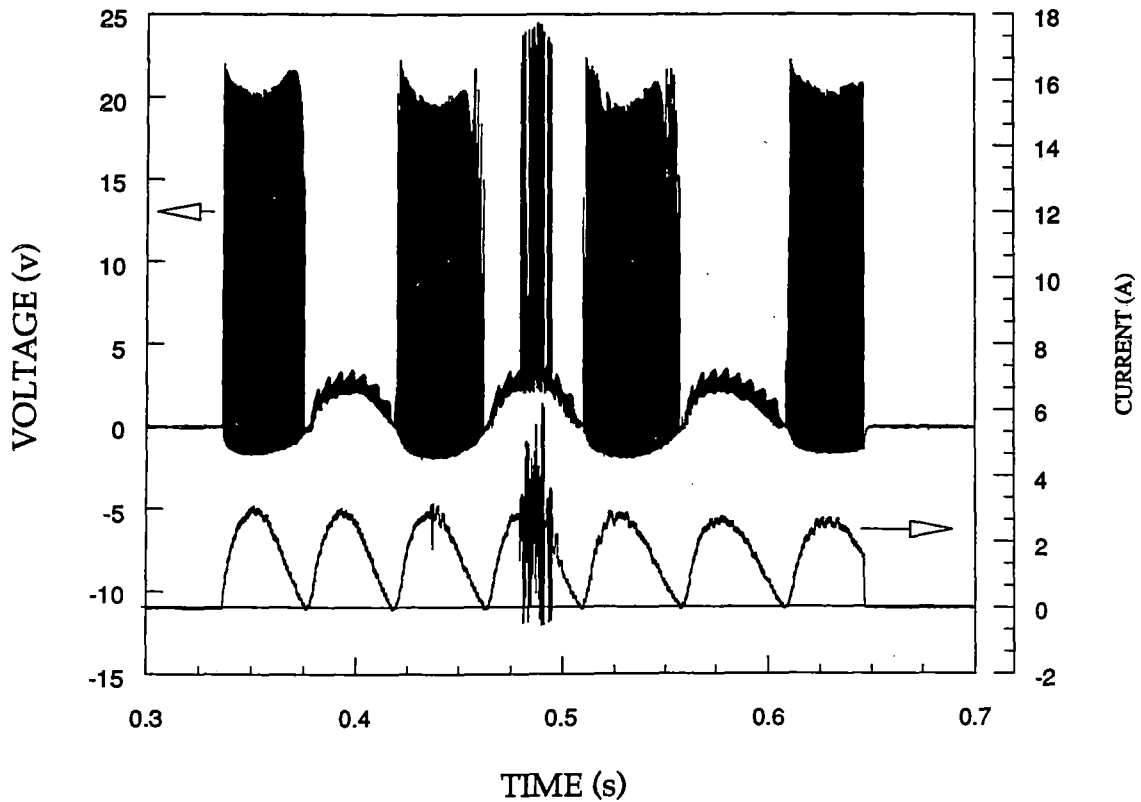


Figure 4-24. Partial-load, deceleration, case 39 - single side coil voltage and bridge current (0.625 Hz, 2.86 m/sec, 0.52 Hz/sec, 2.38 m/sec²)

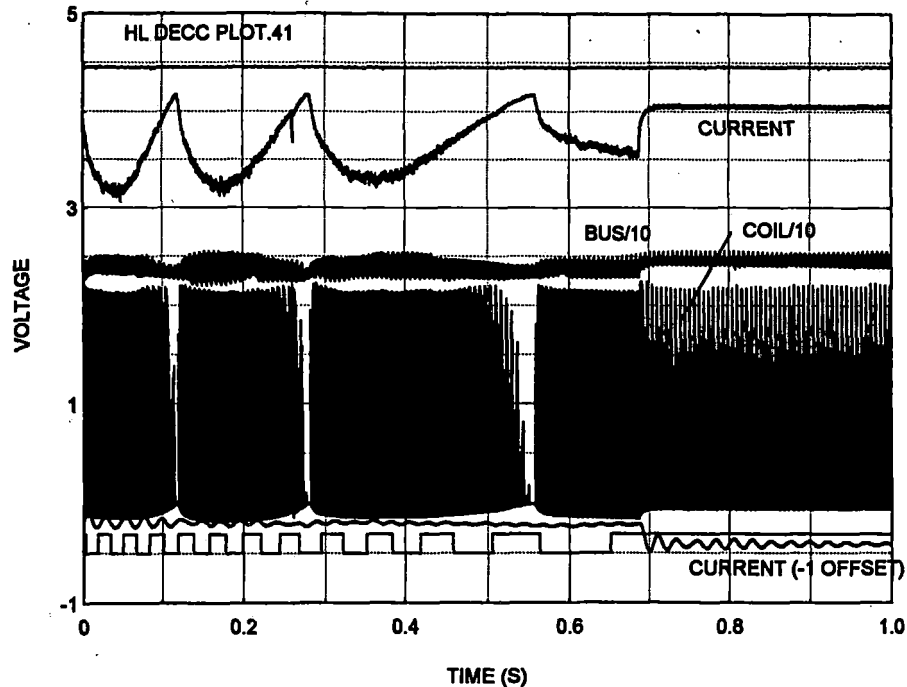


Figure 4-25. Partial-load, deceleration, case 41 (0.12 Hz, 5.4 m/sec, 0.26 Hz/sec, 1.2 m/sec²)

current flow and showed that regenerative operation of the system was physically feasible with the experimental apparatus. Figure 4-24 is a more detailed view of Figure 4-23 in which the bridge bus current and a single terminal coil voltage are shown. The current in the beginning was in the same direction as the back EMF and acted as a brake. The power was dissipated in the coil resistance and the thermal protection resistors that protect the FETs. The spiking region just before the 0.5 sec point was a region where the control was switching the bridge to buck the back EMF as seen in the PWM voltage on the coil. The bridge coast configuration in this mode resulted in a situation in which the coil current caused regeneration through the bridge diodes.

4.2.3 Full Load Cases

This subsection presents the measured test data for cases in which the motor was loaded by shorting the drag motor at its terminals. This provided the maximum resistance to rotation which was proportional to the rotational velocity. For this load, cases were run at constant speed and acceleration. The high drag precluded significant deceleration testing.

Full Load, No Acceleration Cases

Figures 4-26 through 4-28 show full load no-acceleration data. For full load operation, the required current was high and the speed was relatively low. For the reasons described previously, relatively good performance results under these conditions.

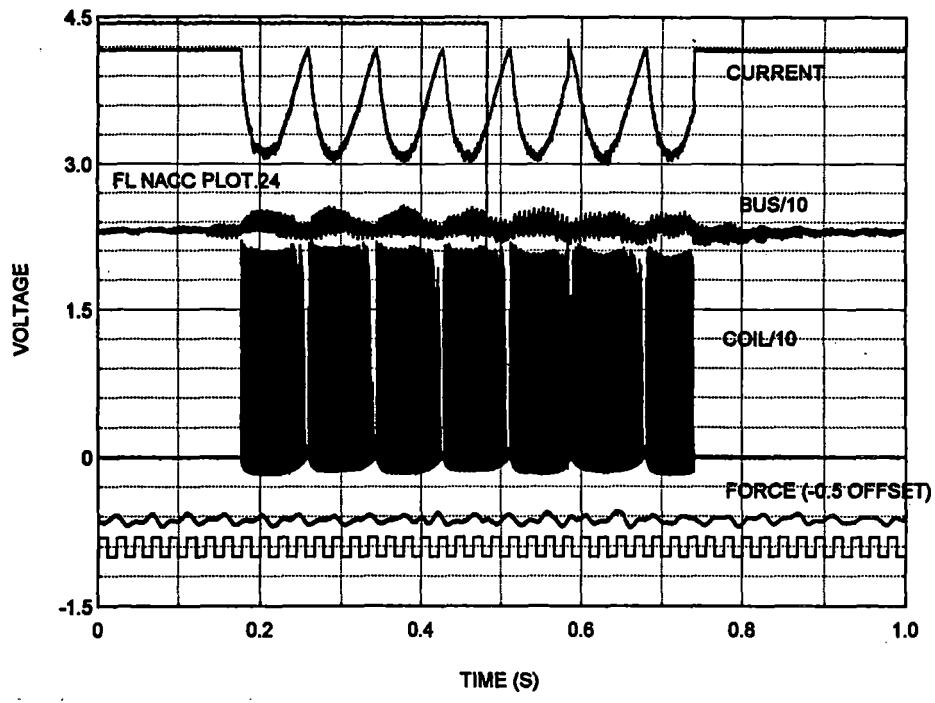


Figure 4-26. Full-load, no acceleration, case 24 (0.35 Hz, 1.6 m/sec)

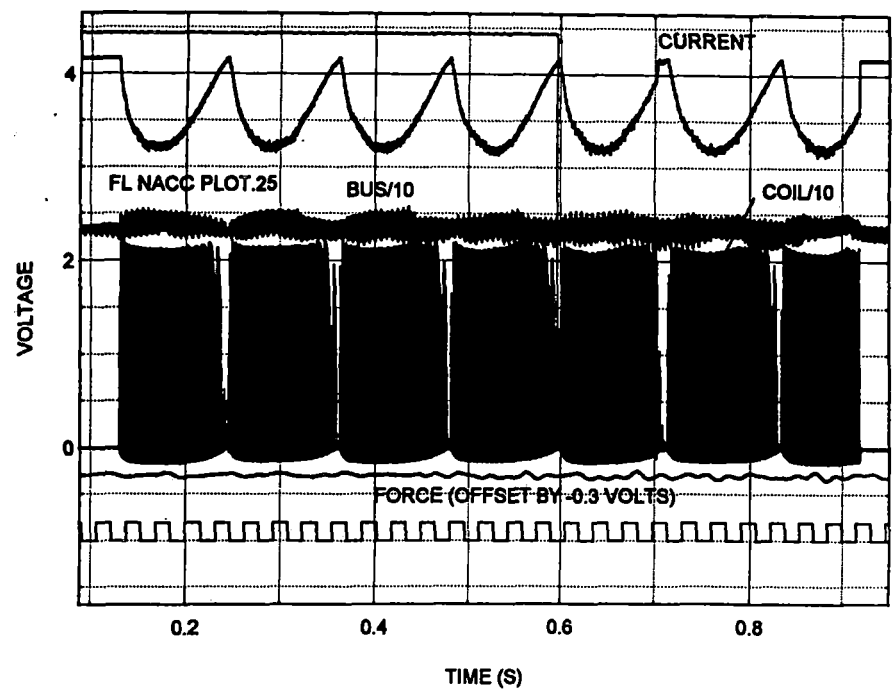


Figure 4-27. Full-load, no acceleration, case 25 (0.25 Hz, 1.16 m/sec)

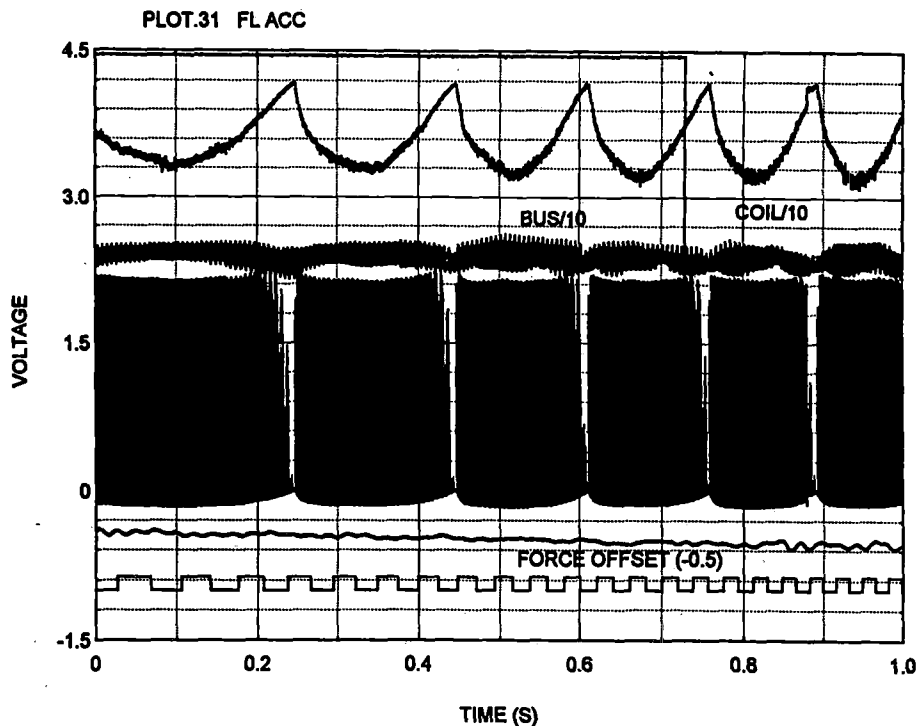


Figure 4-28. Full-load acceleration, case 31 (0.16 Hz, 0.72 m/sec, 0.13 Hz/sec, 0.60 m/sec²)

Full Load, Acceleration Cases

Figure 4-29 shows full load acceleration which produced good performance since the current demand was high and the speed was low.

Coil Spatial Placement

A change in coil spatial placement was simulated by changing the software so that the coil was assumed to be and controlled as if was out of position by 20 percent of the pitch. This was an extreme case and represented a much greater error in position than is physically possible since the coils would interfere mechanically at this large a displacement. The reason for investigating this case was to explore the limits of coil misplacement compensation. Results of the measured perturbation in thrust are shown in Figure 4-30.

4.3 Experimental Conclusions/Recommendations

The experimental apparatus demonstrated the feasibility of the LCLSM concept. Measured electrical parameters agreed with the modeling and simulation performed in the program. The experiment demonstrated distributed communications, control, and power processing for the LCLSM. The loop delay in the PWM control of approximately an order of magnitude greater than that used in development of the control system prevented optimal operation under all conditions. This problem was not one inherent to LCLSM. Given more time and resources, the loop delay could have been reduced substantially using the existing experimental apparatus and more refined programming (assembly code).

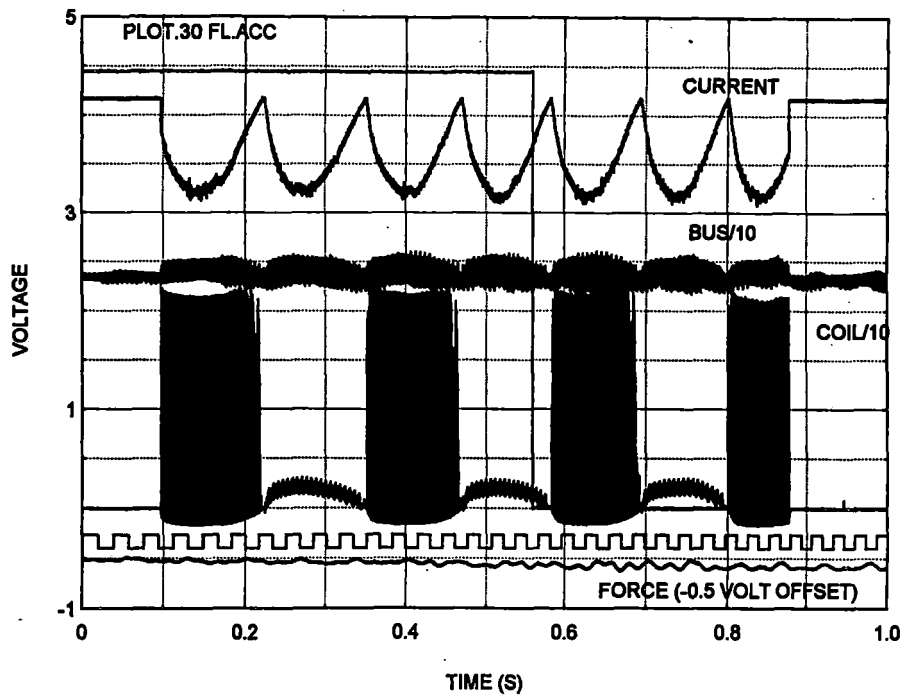


Figure 4-29. Full-load, acceleration, case 30 (0.27 Hz, 1.25 m/sec, 0.11 Hz/sec, 0.52 m/sec²)

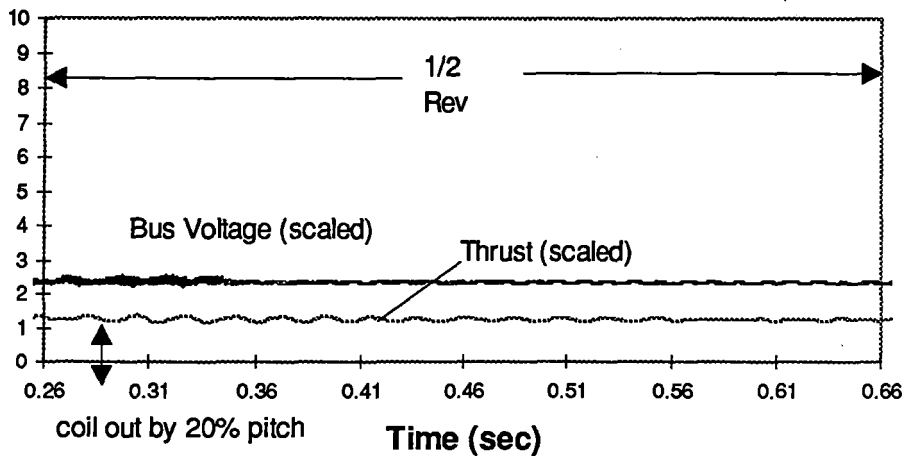


Figure 4-30. Impact of 20 percent coil misplacement

The experimental tests demonstrated that even under a range of operating conditions, optimal and nonoptimal, the LCLSM performed adequately. Indeed, the PWM update delay problem provided significant insight into the variety of phenomena that can be exhibited and the inherent ability of the LCLSM configuration to accommodate these problems and still operate. Practicality of communications between processors and transitions from coil to coil as the vehicle passes were demonstrated. Distributed control and local processing even under degraded operating capabilities was demonstrated. Local power conditioning (inverter operation) with low inductance and high power factor operation was achieved and bus harmonic content and filtering were demonstrated. The major technical aspects of LCLSM operation were proven feasible by the experimental apparatus and testing program.

5. CONCLUSIONS AND RECOMMENDATIONS BASED ON THE LCLSM PROGRAM RESULTS

The LCLSM program verified the feasibility of the LCLSM concept. Analytical tools, scaling laws, control systems, and simulations were developed and verified to enable design of the LCLSM for specific applications. Communications, control, and power processing for the LCLSM were demonstrated. Both specific and general approaches to improving the experimental scaled motor performance have been identified and could be implemented to result in substantial improvement in the range of tests that could be performed. It is important to note that limitations in the present configuration of the experiment are not inherent limitations in the performance capabilities of the LCLSM concept, but instead reflect the limitations in program schedule, resources, and scope. It is recommended that the LCLSM concept investigated and demonstrated in this program, or variants of it, be considered as a sound approach to electric machine design with many advantages for Maglev propulsion applications.

The overall design philosophy which guided the development of the LCLSM system was high efficiency, high reliability, graceful degradation, and low electromagnetic interference. LCLSM is a single-layer propulsion and power transfer system in which independent controllers control dedicated coils to supply a desired waveform with the proper frequency, phase and amplitude. In one embodiment, the coils are commutated locally by pulse-width-modulation (PWM) of semiconductor switches in an H-bridge configuration controlled by signals transmitted over fiber optic communications lines from a central control. Local communication allows energized coils to be limited to those required to achieve a specific purpose (propulsion or power transfer). For example, only those coils in the immediate vicinity of the superconducting magnets need to be energized for propulsion.

The LCLSM design utilizes the same guideway coils for the propulsion and power transfer functions. The PWM scheme is modified from that appropriate for propulsion to a higher frequency, lower current waveform appropriate for power transfer. Power is inductively coupled to onboard coils for power factor correction. In addition, for true Maglev systems, the LCLSM coils can also be used to supply a magnetic guidance function.

A complete LCLSM system will have a great many identical single units, especially semiconductor devices. Repeated experience with semiconductor devices has shown that the cost of a system must account for the dramatic unit price drop as a result of the increase in volume of units. It is recommended that LCLSM be evaluated for economic viability as a propulsion technology for Maglev and related applications.

A specific conclusion of the work is the ability to compensate in software for low tolerance guideway manufacture. This feature was demonstrated and discussed in the report. In most system-level cost analyses, the structural guideway dominates the cost of the entire project for most specific routes. The advantage of this capability is that the guideway system can be manufactured according to low cost, low tolerance methods without compromising future passenger ride comfort.

* A major application for LCLSM technology may be in industrial assembly line conveyance
* systems with variable station dwell times and velocity profiles. Essentially a part on the
* assembly line can be moved independently to subsequent stations as required without regard
* to progress at other stations. Thus, a part can dwell at a station until ready to advance and
* then the advancement can occur independently of other stations. Nonproductive station
* backups are avoided since each part can be independently rerouted to open or available
* stations.

* An additional specific conclusion of this work is the applicability of the LCLSM concept to
* other applications such as photovoltaic power systems, multiple-battery power subsystems
* (including battery chargers, uninterruptible power systems (UPS), etc.), wiring harnesses such
* as used in the automotive industry, and general distributed power processing subsystems.

Recommendations for additional work based upon the successful demonstration of LCLSM-based propulsion include the following areas:

- Cost analysis.
- Power transfer demonstration.
- Investigation of stability enhancement in the air gap and improved ride quality via active control, both dissipative and nondissipative.

A brief description of the recommended areas for investigation follow. The cost analysis of the LCLSM system should include the LCLSM cost savings of capabilities such as power transfer, guidance, and the ability to utilize low tolerance construction techniques for guideway cost savings. The power transfer demonstration could be made with the test bed already established. The goal should be to reduce future risk of design by accomplishing simultaneous propulsion and power transfer with the same coils and control logic at the appropriate frequencies and speeds. Stability enhancement and improved ride quality arise from forces in the track coils which are normal to the plan of the coils. These forces can be used to compensate for the natural tendency of electrodynamic repulsive levitation systems to oscillate about an equilibrium. The magnetic damping of the oscillation can be quite small and the amplitude of the oscillation can grow. Stability enhancement can be used to actively absorb the energy of oscillation.

6. REFERENCES

1. Oppenheim and Willsky, *Signals and Systems*, Prentice Hall, 1983, page 248.
2. *Electromagnetic Levitation and Suspension Techniques*, B.V. Jayawant, 1981, Edward Arnold Publishers, London. ISBN 0 7131 3428 3.
3. C.C. Chan, "An Overview of Electric Vehicle Technology," Proc. IEEE, Vol. 81, No. 9, Sept. 1993, p. 1202.
4. Greg Parker, Collmer representative for Fuji, Fall '93.
5. MCT User's Guide, Harris Semiconductor Corp., Fall '93.
6. Y. Iwasa, "Magnetic Shielding for Magnetically Levitated Vehicles," Proceedings of the IEEE, Vol. 61, No. 5, May 1973.
7. Nasar and Boldea, *Linear Electric Motors*, Prentice Hall, 1987, page 116.
8. I.S. Grant, W. R. Phillips, *Electromagnetism*, John Wiley & Sons 1975, p159

APPENDIX A

HARMONIC CURRENT EQUATIONS

The duty cycle can be derived as follows.

The rates of current change in on and off states are:

$$\left(\frac{d}{dt} I\right)_{\text{on}} = \frac{1}{L} \cdot (VB - EMF - I \cdot R - 2 \cdot VS)$$

$$\left(\frac{d}{dt} I\right)_{\text{off}} = \frac{1}{L} \cdot (-EMF - I \cdot R - VD - VS)$$

Off plus on time = total cycle

$$\delta t = \delta t_{\text{off}} + \delta t_{\text{on}}$$

The rate of change of current is the on time change plus off time change

$$\left(\frac{d}{dt} I\right) \cdot \delta t = \left(\frac{d}{dt} I\right)_{\text{on}} \cdot \delta t_{\text{on}} + \left(\frac{d}{dt} I\right)_{\text{off}} \cdot \delta t_{\text{off}}$$

We can then solve for the fraction of time which the bridge is on (duty cycle)

$$\left(\frac{d}{dt} I\right) \cdot \delta t = \frac{1}{L} \cdot (VB - EMF - I \cdot R - 2 \cdot VS) \cdot \delta t_{\text{on}} + \frac{1}{L} \cdot (-EMF - I \cdot R - VD - VS) \cdot (\delta t - \delta t_{\text{on}})$$

$$\frac{\delta t_{\text{on}}}{\delta t} = \frac{EMF + R \cdot I + VD + VS + L \frac{d}{dt} I}{VB - VS - VD}$$

where

- EMF = instantaneous back EMF
- VD = diode drop
- VS = switch drop
- I = $I_0 \sin(\omega t)$
- L = coil inductance
- VB = bus voltage
- δI_{off} = peak to peak harmonic current (off state current change)
- δI_{on} = on state current change
- δI = current change during one cycle
- δt_{on} = duration of the on state
- δt_{off} = duration of the off state
- δt = duration of one cycle

Given the duty cycle we can then calculate the current change in one off cycle:

$$\left(\frac{d}{dt} I\right)_{\text{off}} = \frac{1}{L} \cdot (-EMF - I \cdot R - VD - VS)$$

$$\delta I_{\text{off}} = \frac{1}{L} \cdot (-EMF - I \cdot R - VD - VS) \delta t_{\text{off}}$$

$$\delta I_{\text{off}} = \left(1 - \frac{\delta t_{\text{on}}}{\delta t}\right) \delta t$$

$$\delta t = \frac{2\pi}{\omega_s}$$

$$\frac{\delta t_{\text{on}}}{\delta t} = \frac{\text{EMF} + R I + \text{VD} + \text{VS} + L \frac{d}{dt} I}{(\text{VB} - \text{VS} + \text{VD})}$$

$$\delta I_{\text{off}} = \frac{1}{L} \cdot (-\text{EMF} - I \cdot R - \text{VD} - \text{VS}) \left(1 - \frac{\delta t_{\text{on}}}{\delta t}\right) \delta t$$

$$\delta I_{\text{off}} = \frac{1}{L} \cdot (-\text{EMF} - I \cdot R - \text{VD} - \text{VS}) \left(1 - \frac{\text{EMF} + R I + \text{VD} + \text{VS} + L \frac{d}{dt} I}{(\text{VB} - \text{VS} - \text{VD})}\right) \frac{2\pi}{\omega_s}$$

For LCLSM the EMF is much larger than the coil resistive or inductive drops or the drops through the components. This permits a simple estimation of the switching harmonic as:

$$\delta I_{\text{off}} = \frac{1}{L} \cdot (-\text{EMF}) \left(1 - \frac{\text{EMF}}{\text{VB}}\right) \frac{2\pi}{\omega_s}$$

The amplitude of the switching harmonic depends on the magnitude of the selected bus current (VB). For estimation purposes we can assume that the bus voltage equals the peak EMF (since the other voltage drops are small). When the EMF is zero, the harmonic current is zero by the first term in the above equation. When the EMF equals the bus current, the harmonic current is zero. The above equation is maximized when the EMF equals half the bus voltage:

$$\delta I_{\text{off}} \sim - \frac{\text{EMF}}{2L} \frac{2\pi}{\omega_s}$$

The EMF can be represented as a sum of harmonics. The fundamental harmonic is:

$$\text{EMF} = \omega_f M_o I_{\text{sc}} \quad (\text{peak})$$

where

M_o = peak SCM to track coil mutual

ω_f = fundamental frequency

I_{sc} = superconducting coil current (ampere-turns)

$$\delta I_{\text{off}} \sim - \frac{\omega_f M_o I_{\text{sc}}}{4L} \frac{2\pi}{\omega_s} \quad (\text{based on } 1/2 \text{ peak EMF})$$

$$\text{Harmonic (peak)} = \frac{\delta I_{\text{off}}}{2} \sim - \frac{\omega_f M_o I_{\text{sc}}}{8L} \frac{2\pi}{\omega_s}$$

APPENDIX B

IGBT DATA SHEET

Ratings and characteristics of Fuji IGBT (MBT) Module

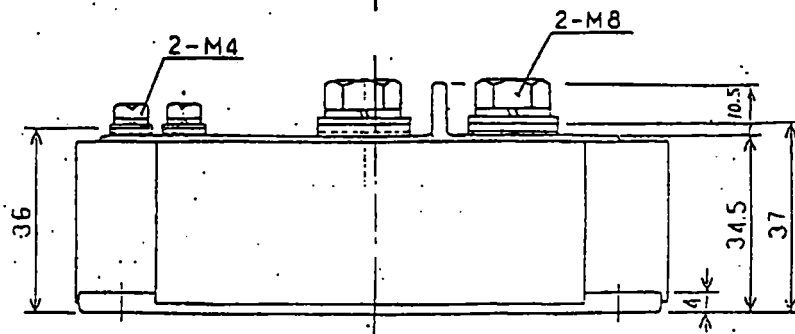
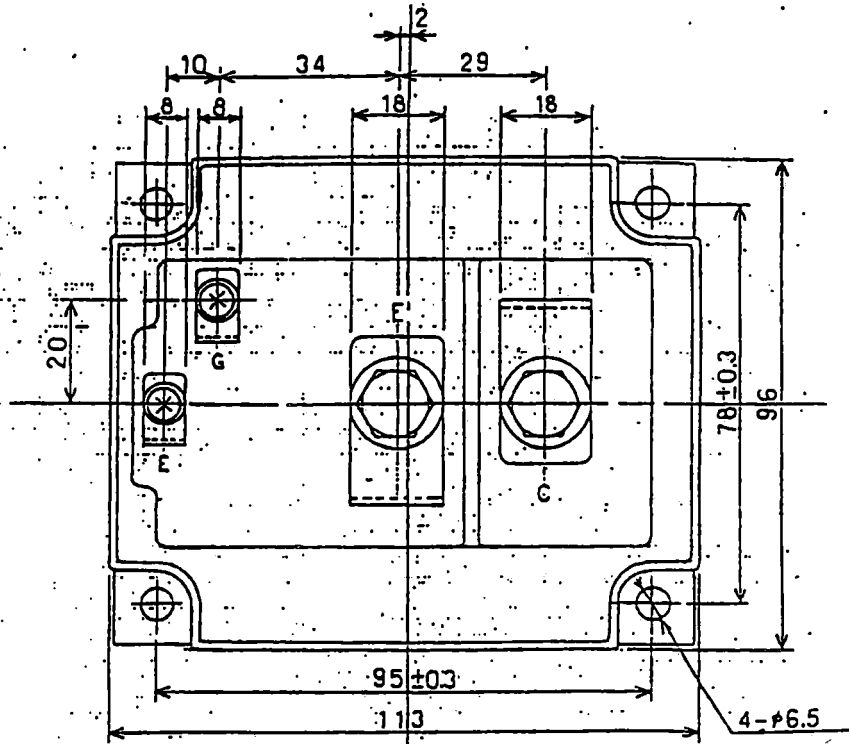
1MBI400L-200 (目標仕様)

1. Outline Drawing

Unit : mm

* Isolation Voltage (Terminal to Copper Case) : AC 5400V, 1 minute

This material and the information herein is the property of Fuji Electric Co., Ltd. They shall be neither reproduced, copied, lent, or disclosed in any way whatsoever for the use of any third party nor used for the manufacturing purposes without the express written consent of Fuji Electric Co., Ltd.



富士電機株式会社

	DATE	NAME	APPROVED
DRAWN	July 15-92	K. Harouchi	

Fuji Electric Co., Ltd.

4. Static electrical characteristics (at Tj=25°C unless otherwise specified)

Items	Symbols	Characteristics			Conditions	Units
		min.	typ.	max.		
Zero gate voltage collector current	I _{CEES}			10.0	Tj = 25°C V _{CE} = 0V V _{CE} @ 200V	mA
						mA
Gate-emitter leakage current	I _{GEES}			1.0	V _{CE} = 0V V _{CE} = ± 2.0V	μA
Gate-emitter threshold voltage	V _{GE(1A)}	3.0		6.0	V _{CE} = 2.0V I _C = 400mA	V
Collector-emitter saturation voltage	V _{CE(sat)}		3.4	4.5	V _{CE} = 1.5V I _C = 400A	V

5. Dynamic ratings (at Tj=25°C unless otherwise specified)

Items	Symbols	Characteristics			Conditions	Units
		min.	typ.	max.		
Turn-off time	t _{off}		2.5	5.0	V _{CE} = 750V, I _C = 400A V _{GE} = ± 15V, R _G = 1.1Ω	μs
	t _f		1.0	3.0		

6. Characteristics of reverse diode (at Tj=25°C unless otherwise specified)

Items	Symbols	Characteristics			Conditions	Units
		min.	typ.	max.		
Diode forward on-voltage	V _F			3.0 ^e	I _F = 400A V _{GE} = 0V	V
Reverse recovery time	t _{rr}		0.6 [@]		I _F = 400A V _{GE} = -10V, 900A/μs	μs

This material and the information herein is the property of Fuji Electric Co., Ltd. They shall be neither reproduced, copied, lent, or disclosed in any way whatsoever for the use of any third party nor used for the manufacturing purposes without the express written consent of Fuji Electric Co., Ltd.

	DATE	NAME	APPROVED
DRAWN	- -		
CHECKED	(S)		

Fuji Electric Co., Ltd.	
DWG. NO.	MT5F4615
	3/4

7. Thermal resistance characteristics

Items	Symbols	Characteristics			Conditions	Units
		min.	typ.	max.		
Thermal resistance	R _{th(j-c)}			0.05	IGBT	°C/W
	R _{th(j-c)}			0.24	Diode	

This material and the information herein is the property of Fuji Electric Co., Ltd. They shall be neither reproduced, copied, lent, or disclosed in any way whatsoever for the use of any third party nor used for the manufacturing purposes without the express written consent of Fuji Electric Co., Ltd.

--	--	--	--

	DATE		
DRAWN	-	NAME	APPROVED

Fuji Electric Co., Ltd.

51 RET 7 40 1 7 10



PROPERTY OF
RESEARCH CENTER
LIBRARY

PROPERTY OF IFA
RESEARCH & DEVELOPMENT
LIBRARY

